Cardiff University

Institute of Medical Engineering and Medical Physics

School of Engineering

Verification of Intensity Modulated Radiotherapy

Rebecca Sian Cufflin

A thesis presented to the Institute of Medical Engineering and Medical Physics at Cardiff School of Engineering, Cardiff University in partial fulfilment of the requirements for the degree of Doctor of Philosophy

Abstract

The main aim of this work was to develop accurate and efficient methods for the verification of Intensity Modulated Radiotherapy (IMRT). IMRT is an advanced form of radiotherapy demanding extensive verification procedures to ensure treatments are delivered accurately. This requires comprehensive sampling of the complex dose distributions impacting on the tumour volume and radiation-sensitive ‘organs at risk’.

This work has focused on the use of electronic portal imaging devices (EPIDs) for verification purposes. Modern EPIDs are composed of a scintillator and an amorphous silicon detector panel with an array of photodiodes and thin film transistors. They are primarily used to verify the patient position during treatment by capturing transmission images, but they also have the potential to be used as efficient dose verification tools of high spatial resolution.

Two complementary dose verification methods have been developed. One approach involves the calculation of portal dose using Monte Carlo (MC) methods. A MC model of the linear accelerator, in combination with the EPID, enables the dose to the detector to be predicted accurately and compared directly with acquired images. An alternative approach has also been developed. This utilises a clinical treatment planning system (TPS) to calculate the dose at the detector level, and convert this to predicted EPID intensity by application of a series of derived correction factors.

Additionally, there have been numerous publications in the literature detailing problems in dosimetry caused by non-uniform backscatter to the imager from the model of detector support arm used in this work. Two novel methods to correct for this issue have been developed, a MC modelling solution and a matrix-based correction.

These developed methods for IMRT dose verification have been applied both prior to and during treatment. When applied to pre-treatment verification, the MC solution is accurate to the 2%, 2 mm level (an average of 96% of points passing gamma criteria of 2%, 2 mm) and the TPS based method is accurate to the 3%, 3 mm level (an average of 98% of points passing gamma criteria of 3%, 3 mm). Both verification methods achieve acceptable verification results during treatment at the 5%, 5 mm level (average gamma pass rates of 97% and 96% being achieved for the MC and TPS based solutions respectively). Furthermore, in initial clinical studies, both techniques have identified dose delivery errors due to changes in patient position or patient anatomy.

Acknowledgements

- Thank you to Cancer Research Wales and Ysgol Uwchradd Tregaron for financial support.
- Thank you to Prof. John Woodcock and Prof. Peter Wells, my supervisors at Cardiff University.
- Thank you to Dr. Geraint Lewis, my supervisor at Velindre Cancer Centre.
- Thank you to Mr. Tony Millin and Dr. Emiliano Spezi for providing many helpful comments and suggestions throughout the duration of this work.
- Thank you to Dr. Patrick Downes for all your help over the last 3 years; for help with all RTGRID problems, for many helpful discussions and for proof reading my thesis.
- Thank you to Mr. Dewi Johns for proof reading my thesis.
- Finally, a big thank you to all my friends and family for their support, especially my mum, Jamie and Jane who were always there for me at times when balancing my PhD with work and home life seemed impossible. Thank you for your encouragement.

Contents

Chapter 1
Introduction 1

1.1 Cancer Incidence and Survival 1
1.2 An Introduction to Radiotherapy 3
1.3 An Introduction to IMRT 5
1.4 The Need for IMRT Verification 8
1.5 An Introduction to EPID Dosimetry 10
1.6 Thesis Context and Objectives 12
1.7 Thesis Outline 13

Chapter 2
An Introduction to the Monte Carlo Method and Dose Calculation Algorithms 15

2.1 An Introduction to Monte Carlo 15
    2.1.1 Statistical Uncertainties and Run-Times in MC Simulations 23
    2.1.2 Distributed Computing 25
2.2 An Introduction to Dose Calculation Algorithms 29
    2.2.1 Energy Fluence from a Clinical Beam 30
    2.2.2 Dose Calculation using Convolution Kernel Models 33

Chapter 3
Monte Carlo Modelling of the Linear Accelerator and Multi-Leaf Collimator 40

3.1 Monte Carlo Modelling of the Linear Accelerator 40
    3.1.1 Introduction 40
    3.1.2 Methods 41
    3.1.3 Results 45
    3.1.4 Discussion 52
3.2 Monte Carlo Modelling of the Multi-Leaf Collimator 52
    3.2.1 Introduction 52
    3.2.2 Methods 54
    3.2.3 Results and Discussion 55

Chapter 4
MC Modelling of EPID 59

4.1 Introduction 59
4.2 Methods 63
    4.2.1 Backscatter Modelling and Calibration 65
4.3 Results 69
4.4 Discussion 76

Chapter 5
Pre-treatment MC EPID Dosimetry for IMRT Verification 78

5.1 Introduction 78
5.2 Methods 79
    5.2.1 Identification of IMRT Dose-Rate Dependent Delivery Errors 79
    5.2.2 Example Head and Neck IMRT Plan 80
    5.2.2.1 Evaluation of Results 81
5.3 Results 84
    5.3.1 Identification of IMRT Delivery Errors 84
    5.3.2 Example Head and Neck IMRT Plan 87
5.4 Discussion and Conclusions 91

Chapter 6
INtegrated TReatment Planning and EPID Dosimetry (INTREPID): Devised Method and Novel Correction for Non-Uniform Backscatter 94

6.1 Introduction 94
6.2 Method 95
    6.2.1 Correction for Non-Uniform Backscatter 99
6.3 Results 101
    6.3.1. Results: Correction for Non-Uniform Backscatter 105
6. 4 Discussion 107
6.5 Conclusions 109

Chapter 7
Application of INtegrated TReatment Planning and EPID Dosimetry (INTREPID) Method for Exit Dosimetry 110

7.1 Introduction 110
7.2 Methods 115
  7.2.1 Verification of Dose Calculation at the Exit Plane 117
  7.2.2 Hounsfield Unit to Electron Density Conversion 119
  7.2.3 Determination of Correction Factors 120
    7.2.3.1 Correction Factor 1: OMP Dose in Water to EPID Image Intensity 120
    7.2.3.2 Correction Factor 2: Field Size Output Factors 121
    7.2.3.3 Correction Factor 3: Off-axis Calibration Matrices 121
    7.2.3.4 Correction Factor 4: Correction for Non-Uniform Backscatter 122
  7.2.4 EPID Positional Stability with Gantry Angle 122
  7.2.5 Clinical IMRT Treatment Verification 123
7.3 Results 124
  7.3.1 Verification of Dose Calculation at the Exit Plane 124
  7.3.2 Hounsfield Unit to Electron Density Conversion 127
  7.3.3 Determination of Correction Factors 128
    7.3.3.1 Correction Factor 1: OMP Dose in Water to EPID Image Intensity 128
    7.3.3.2 Correction Factor 2: Field Size Output Factors 129
    7.3.3.3 Correction Factor 3: Off-Axis Correction Matrices 130
    7.3.3.4 Correction Factor 4: Correction for Non-Uniform Backscatter 131
  7.3.4 EPID Positional Stability with Gantry Angle 132
  7.3.5 IMRT Plan Verification 133
7.4 Conclusions 140

Chapter 8
MC Patient Dose Verification 142

8.1 Introduction 142
8.2 Methods 144
  8.2.1 Full Forward Calculation of Portal Dose 144
  8.2.2 Evaluation of Dose within the Patient 150
8.3 Results 153
  8.3.1Full Forward Calculation of Portal Dose 153
  8.3.2. MC Evaluation of Dose within the Patient 156
8.4 Conclusions 159

Chapter 9
Conclusions 161

9.1 Summary 161
9.2 Further Work and Discussion 164

References 167

Appendix 1: Publications and Presentations 176

Appendix 2: Glossary of Abbreviations 178

List of Figures

Figure 1.1. Typical tumour control probability (TCP) and normal tissue complication probability (NTCP) curves. 5

Figure 2.1. A Monte Carlo linear accelerator model. 18

Figure 2.2. An image of the RTGrid Portal. 28

Figure 2.3. Energy deposition kernels. 34

Figure 2.4. Angular binning of the point kernel in the collapsed cone algorithm. 36

Figure 2.5. The parallel lines along which the energy released is transported in the collapsed cone algorithm. 36

Figure 3.1: Monte Carlo depth dose compared with measured data. 45

Figure 3.2. Effect of changing the width of the primary electron beam on profile shape. 46

Figure 3.3. Profiles demonstrating the agreement between Monte Carlo and measurement for the 10 MV model. 47

Figure 3.4. Profiles demonstrating the agreement between Monte Carlo and measurement for the 10 MV model. 48

Figure 3.5. Profiles demonstrating the agreement between Monte Carlo and measurement for the 6 MV model. 49

Figure 3.6. Profiles demonstrating the agreement between Monte Carlo and measurement for the 6 MV model. 50

Figure 3.7. Normalised MC simulation efficiency versus photon splitting number. 50

Figure 3.8. Monte Carlo generated field size output factors versus measurement, with and without correction for backscattered radiation to the monitor chamber at 6 MV. 51

Figure 3.9. Monte Carlo generated field size output factors versus measurement, with and without correction for backscattered radiation to the monitor chamber at 10 MV. 51

Figure 3.10. Varian 120 leaf Millennium MLC. 53

Figure 3.11. Profile cuts across a diamond shaped field to demonstrate agreement of leaf transmission between Monte Carlo and measurement at 10 MV. 56

Figure 3.12. Profile cuts across a diamond shaped field to demonstrate agreement of leaf transmission between Monte Carlo and measurement at 6 MV. 57

Figure 3.13. Profile cuts across 10 MV beam with closed MLCs to demonstrate MLC leakage. 58

Figure 4.1. Schematric diagram of Varian linac and EPID with supporting structures. 62

Figure 4.2. Images of the EPID and supporting structures. 62

Figure 4.3. Large beam profile in water with beam 'horns' and large beam profile for an EPID image demonstrating the removal of the beam 'horns' by the standard Varian flood field calibration procedure. 65

Figure 4.4. Profile cut through seven linearly aligned (3 x 3) cm^2 fields to demonstrate the effect of non-uniform scatter from EPID components on the intensity of small fields centred at different positions on the device. 67

Figure 4.5. Varian Clinac Pulse Patterns. 69

Figure 4.6. The location of images used to test the robustness of the backscatter solution. 69

Figure 4.7. Cross-sections of the DOSXYZnrc imager model including 'supporting structures'. 71

Figure 4.8. Matching the MC simulated flood images to acquired flood images. 72

Figure 4.9. Portal Image Pixel Intensity versus MC dose and delivered MU for 100, 300 and 600 MU min^{-1}. 73

Figure 4.10. Linearity of EPID response for a dose-rate of 300 MU min^{-1} for extended dose range of 5 to 500 MU. 73

Figure 4.11 The effects of ghosting for a 5MU (10 x 10) cm^2 image immediately following a 100 MU (5 x 5) cm^2 image. 75

Figure 4.12. Inline profiles with and without the backscatter solution delivered in standard (non-IMRT) mode at a dose-rate of 300 MU min^{-1}. 76

Figure 5.1. The sequences set up to detect IMRT delivery errors. 80

Figure 5.2. The complex IMRT plan referred to in Chapter 5**.** 82

Figure 5.3 EPID images (at 140 cm SDD) for beams 1 to 3. 83

Figure 5.4. Inline profiles with and without the backscatter solution delivered in both standard (non-IMRT) and IMRT mode at a dose-rate of 300 MU min^{-1}. 86

Figure 5.5 The effect of the established correction for backscatter for beams with small off axis segments. 88

Figure 5.6 Percentage difference between acquired image and Monte Carlo prediction for a sample beam. 91

Figure 6.1. EPID and water field size output factors. 98

Figure 6.2. Process map for INTREPID pre-treatment portal dosimetry. 98

Figure 6.3. 4 segments of an IMRT beam demonstrating the complexity of segment shapes. 101

Figure 6.4 Description of automated Matlab script processes for INTREPID. 102

Figure 6.5. Sample INTREPID result without correction for backscatter. 104

Figure 6.6. The backscatter correction matrices obtained for various field sizes. 105

Figure 6.7. Sample INTREPID result with correction for backscatter. 108

Figure 7.1. Rotated CT data set and attached 'EPID' within the TPS. 116

Figure 7.2. Process map for INTREPID transit dosimetry. 117

Figure 7.3. The calibration set up for Monte Carlo, treatment planning system calculation and measurement. 118

Figure 7.4 CT scan of CIRS electron density phantom. 120

Figure 7.5. Rando anthropomorphic phantom with attached 'EPID'. 124

Figure 7.6. Dose calculation through different thicknesses of water equivalent material for Monte Carlo simulation and Oncentra Masterplan collapsed cone 'classic ', collapsed cone 'enhanced' and pencil beam 'classic' algorithms. 125

Figure 7.7. Relative electron density versus HU for the Velindre scanner, Oncentra Masterplan (OMP) and calculated using Thomas 1999. 126

Figure 7.8. EPID intensity and Monte Carlo exit dose in water for varying thickness of water equivalent material. 129

Figure 7.9. Average ratio of EPID field size output factor to water field size output factor, for thicknesses of water equivalent material of 6 cm to 35 cm. 130

Figure 7.10. Off-axis correction matrices. Ratio of EPID image intensity to dose in water for various thicknesses of water equivalent material. 131

Figure 7.11: Example matrices for correction for non-uniform backscatter through different thicknesses of water equivalent material. 132

Figure 7.12. Acquired EPID Image and Calibrated TPS Image (INTREPID image) for a prostate beam. 134

Figure 7.13. INTREPID verification results for beams 5 and 6 in table 7. 137

Figure 7.14. INTREPID gamma maps for subsequent fractions for a patient with known positional problems. 138

Figure 7.15. Example gamma pass for an anterior beam exiting a moveable couch bar. 139

Figure 8.1. Process map for Monte Carlo Exit dosimetry. 145

Figure 8.2. A rotated patient CT slice with Monte Carlo EPID model attached perpendicular to the beam direction. 146

Figure 8.3. Defining a patient / phantom dataset and an imager on a common rectilinear grid. 147

Figure 8.4 Velindre scanner HU to electron density curve. 148

Figure 8.5. Example results for MC exit dosimetry. 155

Figure 8.6. Percentage difference between MC simulation and acquired image for a beam exiting a couch bar. 156

Figure 8.7. The Monte Carlo calculated dose distribution versus treatment planning system calculated dose distribution for one CT slice of a prostate IMRT plan. 157

Figure 8.8. The Monte Carlo calculated dose distribution versus treatment planning system calculated dose distribution for one CT slice of a head and neck IMRT plan. 158

List of Tables

Table 1.1. Number of new cases and rates of cancer 2007. 2

Table 1.2. Some key papers published on portal dosimetry techniques. 12

Table 4.1. Measured EPID versus Monte Carlo simulated field size output factors for different backscatter conditions in simulations. 75

Table 5.1. IMRT Plan Information for head and neck plan referred to in chapter 5. 84

Table 5.2. Average IMRT dose delivery errors with associated standard deviation measured with ionisation chamber. 86

Table 5.3 Percentage of points passing gamma criteria of 2%, 2.8 mm and 3%, 4.2 mm with and without the devised correction for non-uniform backscatter using the Monte Carlo technique. 87

Table 5.4 Percentage of points passing gamma criteria of 2%, 2.8 mm and 3%, 4.2 mm at 100 and 300 MU min^{-1} using the Monte Carlo technique. 90

Table 6.1. Results of INTREPID IMRT verification without the correction for backscatter included. 103

Table 6.2. Results of INTREPID IMRT verification with the devised correction for backscatter included. 106

Table 7.1. Average percentage of points passing gamma criteria of 5%, 5 mm (gamma < 1) for 8 patients evaluated using INTREPID exit dosimetry. 134

Table 7.2. Detailed verification results for patient 6 using INTREPID exit dosimetry. 136

Table 8.1. IMRT verification results for Monte Carlo exit dosimetry technique. 154

Chapter 1

Introduction

1.1 Cancer Incidence and Survival

In the UK, more than one in three people will develop cancer in their life (Cancer Research UK 2011). Around 298,000 people were diagnosed with cancer in the UK in 2007; this equates to around 489 cases for every 100,000 people. Wales has the highest incidence of cancer in the UK, in 2007 there being 586 cancers per 100,000 population; table 1.1 gives the rates of cancer in the UK in 2007 (Cancer Research UK 2011). Cancer is most common in older populations, over a third being diagnosed in those over 75 years of age, and so cancer rates are heavily influenced by the number of elderly people in the population. Therefore, quoted cancer rates are usually age standardised to take into account age differences in underlying populations, hence the European age standardised rate given in the table.

The incidence of prostate cancer is reported to be particularly high in Wales (Cancer Research UK 2011). However, some of this variation may be explained by differences in the availability and uptake of screening services for prostate-specific antigen (PSA) across the UK (Cancer Research UK 2011, Brewster *et al.* 2000).

	England	**Wales**	**Scotland**	**N. Ireland**	**UK**
Crude rate per 100,000	480.2	586.0	534.1	439.1	488.7
European age standardised rate per 100,000	371.4	415.8	403.0	388.2	377.0

Table 1.1. Number of new cases and rates of cancer (all malignant tumours excluding non-melanoma skin cancer), 2007 (data from Cancer Research UK 2011).

Continual improvements in cancer treatments enable a greater number of people to survive, cancer survival rates usually being quoted at 1, 3, 5 and 10 years post diagnosis. Survival is improving for the majority of cancer sites, the Welsh Cancer Intelligence and Surveillance Unit (2010) quoting 46% of males surviving five years from diagnosis in the period 2000-2004 compared to 31% in the period 1985-1989, with female five year survival increasing from 45% in 1985-1989 to 53% in 2000-2004. They state that the majority of these increases can be attributed to prostate cancer for males for which five year survival has increased from 45% in 1985-1989 to 78% in 2000-2004, and for breast cancer in females for which five year survival has increased from 66% in 1985-1989 to 82% in 2000-2004.

1.2 An Introduction to Radiotherapy

Radiotherapy has been used in the treatment of cancer for over 100 years. It involves the use of ionising radiation in the form of X-rays, electrons, gamma rays, neutrons or protons. Electrons and protons are classed as ‘directly’ ionising radiation as they are charged particles that impart energy directly to matter, whilst X-rays, gamma rays and neutrons are classed as ‘indirectly’ ionising, energy being imparted in a multiple step process. X-ray or gamma photons firstly interact with the medium via interactions such as the photoelectric effect, Compton effect or pair production, these interactions releasing electrons that impart energy to matter, whereas neutrons predominantly interact with atomic nuclei releasing photons or electrons. Radiotherapy may be administered by external beams of radiation directed towards the tumour (external beam radiotherapy or teletherapy), by positioning radioactive material close to, or within, the tumour (brachytherapy), or by administering radioactive liquids with preferential uptake in a particular organ (radionuclide therapy).

The main difficulty in treating cancers with radiotherapy is that since the tumour mass is usually situated either within or on the surface of a particular tissue or organ it is inevitable that healthy tissues will also receive a high dose of radiation. The aim of radiotherapy treatments is to deliver the highest possible dose to the tumour in order to maximise the probability of complete tumour regression whilst restricting the dose to the normal tissue so that it is able to maintain its function after treatment.

The key to successful radiotherapy treatment lies in the sensitivity of different tissues to radiation, tumours often being more sensitive to radiation than the nearby healthy tissues. Figure 1.1 gives typical tumour control probability (TCP) and normal tissue complication probability (NTCP) curves as a function of dose[1].

TCP curves are typically 'sigmoid' in shape, with minimal chance of cure at low doses, a rapid rise in cure-rate once a particular dose is received and an asymptotic approach to maximum effect. The NTCP curve follows a similar shape, radiotherapy being most successful in anatomical regions with the greatest lateral displacement between the TCP and NTCP curves. The ratio of tumour control probability to normal tissue complications probability for a particular dose is called the 'therapeutic index'. In addition, radiotherapy treatments are usually 'fractionated', i.e. the delivered dose is spread out over a number of treatments. Fractionated radiotherapy enables normal tissues to partly repair themselves between radiotherapy treatments (normal tissues preferentially repair over tumour cells), therefore maximising the therapeutic index.

---

[1] It should be noted that the term dose is used to mean absorbed dose throughout the thesis.

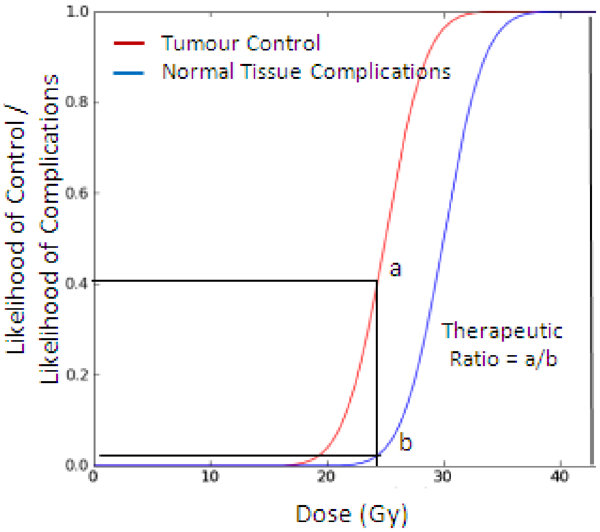

Figure 1.1. Typical tumour control probability (TCP) and normal tissue complication probability (NTCP) curves as a function of dose.

1.3 An Introduction to IMRT

Normal tissue complications limit the dose that can be delivered to the tumour. Intensity Modulated Radiotherapy (IMRT) is an advanced form of radiotherapy in which the intensity of each radiation beam is modulated, enabling greater conformity to the tumour volume. Increased sparing of organs at risk (OAR) in close proximity to the tumour reduces toxicity to these organs and also gives the potential for dose escalation, achieving greater tumour control. With increasing evidence that it provides improved treatment outcomes (McDonald *et al*. 2009, Staffurth 2010, Dirix and Nuyts 2010, Dirix *et al*. 2010, Jensen *et al*. 2010) IMRT has become the standard of care for many treatment sites.

Intensity modulation is achieved by breaking the beam down into many ‘beamlets’ of varying intensities shaped by a multi-leaf-collimator (MLC). The MLC is situated in the head of the linear accelerator and consists of typically 80 to 160 moveable tungsten ‘leaves’ (figure 3.10). IMRT is usually carried out using either ‘step and shoot’ or ‘sliding window’ (dynamic) techniques. The step and shoot method requires the beam to be turned off between MLC movements. The dynamic method involves moving the collimator leaves continuously with the radiation on.

Conventional treatment planning uses a ‘forward’ method whereby the beam sizes, directions and weights are specified by the person preparing the plan, based on previous experience. The high number of parameters involved in complex IMRT dose distributions usually necessitates an automated approach. These dose distributions are achieved using ‘inverse’ planning techniques. Inverse planning involves specifying the dose deposition objectives by identifying the dose that must be achieved in the tumour volume and the doses that must not be exceeded in any critical structures or normal tissues, giving each objective a level of importance. The IMRT optimisation process then determines the beam parameters (i.e. the number of beamlets and intensities required) that will give the best outcome.

There are two main categories of mathematical processes by which treatment planning software can carry out this optimisation process; stochastic and deterministic methods. Both methods seek the ideal dose distributions iteratively. The iteration processes run through a sequence of possible beam changes, each change being associated with a ‘cost function’, which is based on the degree by which the desired dose distribution is improved or worsened by the change. A simple example of a deterministic search algorithm is gradient descent. The problem with this method is that it is possible to get stuck in local minima and so the ideal dose distribution (global minimum) is not approached. Stochastic searches, such as simulated annealing, are characterised by some degree of random search behaviour, and so getting stuck in local minima can be prevented.

Staffurth (2010) has presented a review of the clinical benefit for IMRT and identified 61 studies comparing IMRT with conventional radiotherapy. Toxicity related effects were reported to be consistently reduced for IMRT. In particular, it was reported that inverse-planned IMRT maintains parotid saliva production and reduces acute and late xerostomia during radiotherapy for locally advanced head and neck cancer, and reduces late rectal toxicity in prostate cancer patients allowing for safe dose escalation. Additionally it was reported that simpler forward-planned IMRT of the breast reduces acute toxicity and improves late clinician-assessed cosmesis compared with conventional tangential breast radiotherapy.

Recently, Intensity Modulated Arc Therapy (IMAT) has been introduced by linear accelerator and treatment planning system manufacturers, which allows similar or superior dose distributions to IMRT with reduced treatment time. In this technique, the radiation is delivered in arcs, rather than delivered from typically 5 to 7 discrete directions. However, at the time of writing, our centre has only recently obtained a planning system able to support this treatment mode and no clinically satisfactory plans have as yet been produced.

1.4 The Need for IMRT Verification

An excessive dose of radiation leads to radiation necrosis of healthy tissues, whilst an inadequate dose would fail to kill the cancerous cells, in time leading to recurrence of the tumour. The importance of accurate and precise dosimetry and radiotherapy treatment planning therefore cannot be overemphasised. Advanced radiotherapy techniques, such as IMRT, require extensive verification measurements to ensure that the treatments are delivered correctly (Ibbott *et al.* 2008, Ezzell *et al.* 2009). The Radiological Physics Centre in the United States reported in 2008 that 30% of the centres evaluated as part of an IMRT credentialing process failed to deliver IMRT to within 7% of the planned dose distribution (Ibbott *et al.* 2008). Differences between the planned dose and the dose delivered by the linear accelerator may arise from inaccuracies in the treatment planning system (TPS) dose calculation algorithm or from errors in IMRT treatment delivery. Furthermore, all dosimetry methods are associated with uncertainties, and inter-fractional dose variations will occur due to patient positional errors and day-to-day anatomical variations (Castadot *et al*. 2010).

Initial commissioning of IMRT requires thorough verification of the complex three dimensional dose distributions calculated by the treatment planning system. Due to the complexity of the treatments, most centres still verify these dose distributions on a patient by patient basis to ensure correct TPS dose calculation and treatment delivery by the linear accelerator prior to the patient being treated (Ezzell *et al.* 2009). Some centres additionally measure the dose delivered during treatment, a recommendation of the UK Report 'Towards Safer Radiotherapy' (Royal College of Radiologists 2008).

Conventional dosimetric methods such as ionisation chamber, diode or thermoluminescent dosimeter (TLD), have limitations for IMRT verification in that they are only able to provide point by point sampling and so do not comprehensively sample what may be complex distributions with steep dose gradients impacting on both the tumour volume and OAR. Traditional film dosimetry, which provides very high resolution in 2D, is no longer an option for most centres, with film processors becoming obsolete as radiotherapy centres turn to digital picture archiving and communication systems (PACS). The main alternatives available are radiochromic film (that requires no chemical processing), 2D arrays (composed of ion chambers or diodes) or electronic portal imaging devices (EPIDs).

1.5 An Introduction to EPID Dosimetry

EPIDs, which are primarily used for the verification of patient position during treatment by acquiring transmission images, are increasingly becoming the dosimeters of choice in this area (van Elmpt *et al.* 2008a, van Elmpt and Ezzell 2009). Most centres already have EPIDs available on their linear accelerators (linacs), and so they provide cost effective absolute dosimetry with rapid read-out. In addition, the uncertainties created by non-uniform film response and differences in temperature or time between irradiation and analysis are eliminated. 2D arrays of ion chambers or diodes, even with the detector shift methods described for increasing their resolution (Spezi *et al*. 2006), are still unable to provide the sub-millimetre spatial resolution available from EPIDs or film. Spatial resolution is of particular importance for IMRT verification to ensure that the MLC leaves are being driven to the correct position during delivery.

There are a number of EPID dosimetry approaches published in the literature, both *pre-treatment* to verify delivery before treatment commences and *transit,* or *transmission,* dosimetry to verify delivery during treatment of the patient. Table 1.2 identifies some of the key papers published. *Transmission* methods either evaluate the dose distribution at the plane of the detector or reconstruct the dose within the patient. Reconstruction can be achieved by back-projection methods (McNutt *et al.* 1996, Wendling *et al.* 2006, McDermott *et al.* 2006b) or by using fluence profiles extracted from the acquired images to calculate the dose within the patient (Partridge *et al.* 2002, Steciw *et al.* 2005, Renner *et al.* 2005, van Elmpt *et al.* 2007).

‘A literature review of electronic portal imaging for radiotherapy dosimetry’ (van Elmpt *et al.* 2008a) points out the vast range of publications yet current lack of commercially available transit dosimetry solutions. ‘Dosimetry Check’ from Math Resolutions[2], based on the methods presented by Renner *et al.* (2005), claims to be the first commercial EPID based transit dosimetry solution. Sankar *et al.* (2010), reported preliminary results using this software at the Institute of Physics and Engineering in Medicine (IPEM) Biennial Radiotherapy meeting, which are discussed in more detail in Chapter 7.

---

[2] http://www.mathresolutions.com/rtqasys.htm

Pre-treatment Verification (non-transit images)	***At detector plane***	**2D**	Van Esch 2004, Siebers *et al.* 2004, Li *et al.* 2006, Nicolini *et al.* 2006, Parent *et al.* 2006, Parent *et al.* 2007, Greer *et al.* 2009, Cufflin *et al.* 2010a
	Dose reconstructed within patient CT / phantom	**2D**	Warkentin *et al.* 2003
		3D	Steciw *et al.* 2005, Renner *et al.* 2005, van Elmpt *et al.* 2007
Transit (Transmission) Dosimetry	***At detector plane***	**2D**	McNutt *et al*. 1996, McCurdy *et al.* 2001, Spezi and Lewis 2002, Chin *et al.* 2003, Chin *et al.* 2005, Chen *et al.* 2006, Nijsten *et al.* 2007a, Mohammadi *et al*. 2006, Reich *et al*. 2006, Dahlgren *et al*. 2002
	Dose reconstructed within patient CT	**1D**	Nijsten *et al.* 2007b, Piermattei *et al.* 2007
		2D	Wendling *et al.* 2006, McDermott *et al.* 2006b
		3D	McDermott *et al.* 2008, Partridge *et al.* 2002
Review Papers / Discussions			van Elmpt *et al.* 2008a, van Elmpt *et al.* 2009

Table 1.2. Some key papers published on portal dosimetry techniques.

1.6 Thesis Context and Objectives

The work in this thesis was carried out at Velindre Cancer Centre (VCC) in Cardiff, Wales. VCC is one of the largest cancer centres in the UK, providing specialist cancer services to over 1.5 million people in South East Wales and beyond.

The aims of this work were to develop accurate and efficient methods for the verification of IMRT, an advanced form of radiotherapy. The main focal point has been the development of EPID dosimetry for IMRT verification. Two methods have been developed side-by-side, one method involving full forward Monte Carlo (MC) calculation of portal dose and the other utilising the treatment planning system to calculate the dose at the EPID level, and convert this to predicted EPID intensity.

1.7 Thesis Outline

This thesis is organised such that:

Chapter 2 gives an introduction to the MC method and dose calculation algorithms, with Chapter 3 detailing the MC modelling and optimisation of parameters that has been carried out as a part of this work.

Chapter 4 describes the MC modelling of the Varian aS500 EPID, paying particular attention to the modelling of the Varian imager support arm which is known to cause difficulties in portal dosimetry due to non-uniform backscatter (Siebers *et al.* 2004, Ko *et al.* 2004, Moore and Siebers 2005, Greer *et al.* 2009, Wang *et al.* 2009).

Chapter 5 demonstrates the use of the developed MC EPID model for pre-treatment IMRT verification.

Chapter 6 details INTREPID (INtegrated TReatment Planning and EPID Dosimetry), the method devised to calculate the dose at the EPID level within the treatment planning system and convert to EPID intensity. The associated novel correction for non-uniform backscatter is also described.

Chapter 7 extends the INTREPID method to the verification of delivery during treatment.

Chapter 8, MC portal dosimetry, details the methods used for full-forward MC calculation of portal dose for transit dosimetry during treatment. The MC calculated dose to the patient is also calculated as a part of this process.

Finally, Chapter 9 summarises the work in this thesis and identifies some areas for future work.

Chapter 2

An Introduction to the Monte Carlo Method and Dose Calculation Algorithms

2.1 An Introduction to Monte Carlo

The MC method is known to be the most accurate dose calculation method in the presence of patient contour and tissue heterogeneities (Rogers 2006). The technique, so called because the possible particle interactions are sampled using random number generators, involves simulating the irradiation system. Accurate models of the radiation sources are required and the radiation transport determined using physical models for energy deposition and detailed specification of the properties of the different materials involved.

The term Monte Carlo was first used to describe random sampling of radiation transport at the end of the Second World War (Chetty *et al.* 2007). Increased computing power and the introduction of new MC codes have resulted in an enormous increase in MC studies in radiotherapy in recent years, with a doubling of papers on the subject every 5 years between the first Physics in Medicine and Biology paper in 1967 (which applied MC techniques to calculate the response of a NaI detector used to measure radiotherapy beam spectra (Bentley *et al.* 1967)) and 2000 when the numbers levelled off (Rogers 2006). To quote Chetty *et al.* (2007) "As a technique for calculating dose in a patient the underlying physical basis is much simpler in concept than analytic algorithms because the MC method consists of a straightforward simulation of reality and does not involve complex approximations nor models of dose deposition, but only a knowledge of the physics of the various interactions which have been well understood for over 50 years in most cases".

This project uses the BEAMnrc package (Rogers *et al.* 2001), an upgraded version of the original BEAM code (Rogers *et al.* 1995). BEAMnrc is used for linac simulations and the associated code DOSXYZnrc, for calculations of dose distributions within a patient, phantom or EPID. BEAMnrc allows easy modelling of radiotherapy linear accelerators, and has been bench-marked and used extensively in the scientific literature and is therefore often considered to be the gold standard for MC simulations for radiotherapy applications (Hasenbalg *et al.* 2008). The BEAMnrc package is based on the EGS (Electron Gamma Shower) MC code (Nelson *et al.* 1985, Kawrakow 2000) which was developed at the Stanford Linear Accelerator Center (SLAC) and the National Research Council of Canada (NRC). Linac models are built by specifying which “component modules” are to be used and in what order. It is possible to represent each individual part of the linac using these component modules.

Up until 2005, all BEAMnrc simulations generated “phase-space” files recording the type, energy and direction of each particle crossing a specific plane. These phase-space files are used to feed subsequent MC simulations, either DOSXYZnrc simulations in a phantom or patient, or further BEAMnrc simulations. For example a phase-space file above the linac jaws may be created to increase the speed of simulations, avoiding repetition of simulating particles through static geometries. In releases of BEAMnrc since 2005 an additional option to use a full BEAMnrc simulation of a treatment head as a particle source for DOSXYZnrc simulations has been available, with the obvious advantage that intermediate phase space data need not be stored, therefore preventing data storage issues. For calculations with the precision required in a clinical setting this can save tens of GBytes of disk storage. However, the extra time required to perform a full linac simulation to generate source particles results in reduced efficiency. Kawrakow and Walters (2006) directly compared efficiency between phase space sources and full BEAMnrc simulation sources. They reported that with efficient use of variance reduction techniques, such as photon splitting within DOSXYZnrc and directional bremsstrahlung splitting within BEAMnrc (see page 20), BEAMnrc simulation sources are only 3 – 13% less efficient than simulations with phase-space file sources, eliminating the need for storage of intermediate phase space. Figure 2.1 illustrates a Monte Carlo model of a linear accelerator.

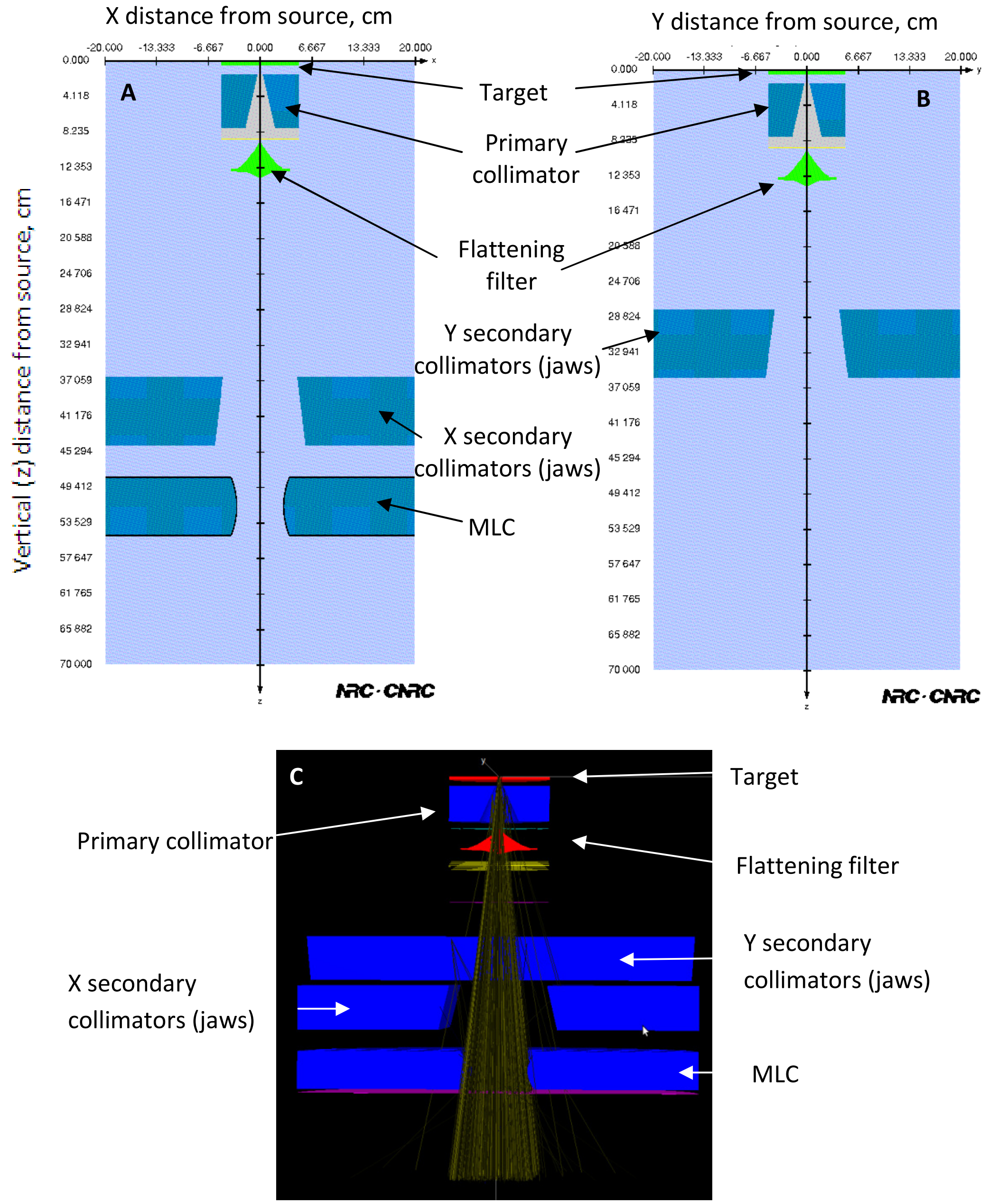

Figure 2.1. A Monte Carlo linear accelerator model A) X-Z cross-section B) Y-Z cross-section and C) Diagram showing photon tracks.

MC transport relies on the availability of cross-section datasets for each physical process simulated. BEAM material cross section data are created with the pre-processor PEGS4 (Nelson 1985) and are based on material compositions and densities set out in the International Commission on Radiation Units (ICRU) Report 37 (ICRU 1984). There are 2 data sets readily available, ICRU 521 and ICRU 700, which correspond to kinetic energy thresholds for secondary electron production of 10 and 189 keV respectively.

MC transport of electrons is significantly more complicated than for photons, electrons undergoing a very large number of collisions during the slowing down process. Condensed history techniques are used to condense a large number of these electron collisions into a single step, the shorter the step the more accurate the simulation. Condensed history techniques were first described by Berger in 1963, this technique now forming the basis of all electron-photon MC codes. With the aim of improving electron transport at low energies EGS introduced parameters 'ESTEPE' and 'SMAX' which represent the maximum fractional energy loss per electron step and the maximum step length allowed. This can, however, result in artefacts when crossing boundaries where multiple step assumptions are not valid anymore. To overcome this boundary crossing problem BEAM originally incorporated 'PRESTA' (at proximity to interface or boundary, the electron step is shortened) (Bielajew and Rogers 1987). PRESTA was the default boundary crossing algorithm (BCA) up until 2006, after which the 'EXACT' algorithm became the default. The EXACT BCA was introduced in EGSnrc to eliminate a known fluence singularity caused by forcing a multiple scattering event at a boundary (Walters and Kawrakow 2007). In the EXACT case, electrons are transported in single elastic scattering mode as soon as they are within a specified distance from the boundary.

Transport cut offs and range rejection techniques are used to increase calculation speeds, and when used correctly should improve efficiency without a significant change in the result. If the particle energy falls below the relevant transport cut off (ECUT for electrons and PCUT for photons), the particle trajectory is terminated and its energy deposited in the current region. Electron range rejection involves terminating electron tracks with a residual range that does not allow them to reach the scoring plane of interest. For linac simulations 2 – 3 MeV is chosen (Sheikh-Bagheri and Rogers 2002).

Variance reduction techniques are used in MC simulations to decrease the calculation time to reach a certain statistical variance in the simulation outputs. Bremsstrahlung splitting creates a higher number of photons with reduced statistical weights. Directional Bremsstrahlung Splitting (DBS) was introduced by Kawrakow *et al.* (2004) and results in greater efficiency than bremsstrahlung splitting methods used previously. If a primary charged particle undergoes a bremsstrahlung or annihilation event then the event is split 'NBRSPL' times, the energy deposition 'weight' of the resultant photons being multiplied by NBRSPL^{-1}. Photons aimed at the splitting field are kept and are considered 'non-fat' (low weight), with random number Russian Roulette being played on those photons aimed away from the splitting field. The photon survives if the random number is less than a survival threshold of NBRSPL^{-1}, surviving photons having their weight multiplied by NBRSPL (these are now considered 'fat'). This technique reduces calculation times as fewer particles aimed away from the splitting field are tracked. DBS is very efficient for photon fluence calculations but results in only a few 'fat' charged particles reaching the plane of interest. Charged particle splitting must therefore be carried out to "recover" the charged particles.

Efficiency improvements within the DOSXYZnrc simulation may be achieved by making use of the particle recycling or photon splitting options. Kawrakow and Walters (2006) found that use of photon splitting increases the dose calculation efficiency by a factor of up to 6.5, depending on beam energy, field size, voxel size, and the type of secondary collimation used in the simulation. They found the optimum efficiency with photon splitting to be 55% higher than that with particle recycling. In photon splitting, all photons are split into n_split photons, each with a weight equal to n_split^{-1} times the weight of the original photon. At each interaction site charged particles and/or scattered photons are produced, Russian Roulette being played on all scattered photons with a survival probability of n_split^{-1}. Surviving photons have their weight increased by n_split so that their weight is equal to that of the original photon before splitting. All charged particles survive with weight equal to n_split^{-1} times the original weight.

Whilst the dose calculation technique which shows closest agreement between calculation and measurement is obviously the more desirable, full MC techniques are computationally intensive and still very time consuming, and so are not suitable for patient dose calculations that require near real-time interaction. Faster MC techniques, most based on the code 'VMC' (Kawrakow *et al.*, 1996), have been implemented in some of the most up-to-date treatment planning systems. These techniques were first applied to electron beam simulation, but modified versions are now used for the simulation of photon beams (Gardner *et al.* 2007, Hasenbalg *et al.* 2008, Kunzler *et al.* 2009). These codes are faster due to the intensive use of variance reduction techniques and a much faster implementation of the condensed history technique for charged particle transport, and are often limited to simulating the beam collimation system and patient dose. With multiple core PCs now readily available, faster MC techniques are likely to form the dose computational basis of treatment planning systems in the future, although this is not the case generally at present.

2.1.1 Statistical Uncertainties and Run-Times in MC Simulations

MC simulations are subject to statistical uncertainties. In the current application these are due to uncertainties in the accelerator head (i.e. source) simulation and the random nature of dose deposition. If a pre-calculated phase-space is used, re-using phase space particles in the phantom simulation will improve statistical uncertainties in the result, to the level of statistical uncertainty in the phase-space file.

Beamnrc / DOSXYZnrc use the history-by-history method for calculating uncertainties. The estimate of the uncertainty (standard error of the mean, $s_{\bar{x}}$) of a scored quantity X is given by

$$s_{\bar{x}} = \sqrt{\frac{1}{N-1}\left(\frac{\sum_{i=1}^{N} X_i^2}{N} - \left(\frac{\sum_{i=1}^{N} X_i}{N}\right)^2\right)} \qquad (2.1)$$

where N is the number of histories and X_i is the contribution to the scored quantity by independent history i. When calculating uncertainties it is important to correlate a primary particle with its ‘secondaries’ as treating the secondary particles as independent histories results in an underestimate of the uncertainty.

Statistical uncertainties are dependent upon the number of histories per voxel. Therefore, for a certain number of histories, decreasing the voxel size in the simulation increases the statistical uncertainty. For IMRT simulations involving large intensity gradients, a high resolution (and thus small voxel size) of the order of 1 – 2 mm is required. Commissioning of the MC MLC requires even finer voxels to accurately verify the rounded leaf-ends and inter-leaf leakage.

For standard BEAMnrc patient simulations with the region of interest at or close to the linac isocentre, the number of particles, or histories, required to give a certain statistical accuracy is given by equation 2.2 (BEAM 1997).

$$N = \frac{1}{s^2 \mu_{en}} \frac{A}{V_{voxel}} \qquad (2.2)$$

where N is the number of histories to run, s is the desired fractional uncertainty, μ_{en} is the effective energy absorption coefficient for the medium, A is the area of the beam aperture projection at isocentre and V_{voxel} is the volume of the simulation voxels. It is normally assumed that the body composition of the patient is effectively water equivalent and so a value of 0.03 cm^{-1} is usually used for μ_{en}. The greater the number of histories the longer the simulation time, but the lower the final statistical uncertainty in the resulting dose distribution. The smaller the voxel size the greater the number of histories required to reach a particular statistical uncertainty.

2.1.2 Distributed Computing

The main downside of MC simulations is the lengthy calculation time required. Pencil beam (PB) and Collapsed Cone (CC) dose calculations (section 2.2) take only a matter of minutes to run on a single PC, whereas the clinical MC simulations presented in this thesis would take many weeks of run-time on a single PC. Although the variance reduction techniques described above help to make the simulations faster, to enable run-times for the simulations described in this thesis to become clinically acceptable they must be distributed amongst a larger number of processors simultaneously. The parallel nature of MC simulations makes it relatively straightforward to distribute simulations across multiple machines. Different particle histories are run simultaneously on different computers and, as each radiation history is inherently independent, the final results are neither biased by the physics nor the statistics.

There are a number of methods for distributing simulations across a number of processors. The easiest method to implement is a cluster of machines with homogeneous software and hardware that share a common file system, e.g. a ‘Beowulf’ cluster (Love *et al.* 2000). These are dedicated machines to the process in question and as ownership is typically local, workload is usually predictable and simpler to co-ordinate. High throughput computing (HTC) systems, on the other hand distribute simulations across processors that do not necessarily share a common file system or memory. These processors are not dedicated to HTC but, since they are not constantly in use, their 'idle time' (evenings and weekends for example) may be used for intensive computations.

The release of the multi-platform version of BEAMnrc in 2005 enabled the BEAMnrc code to run on Windows NT/2000/XP and on Apple Mac OSX, immediately making more resources available for HTC. The idea behind 'Grid' HTC systems, such as the National Grid Service (NGS)[3], is to provide computing power for all that require it by simply 'plugging in'. A platform or web portal can be provided to enable simulations to be submitted, and so the use of resources is not restricted to computer experts in the field. Installation of BEAMnrc and DOSXYZnrc on every computer on a 'Grid' system is not feasible due to limited disk space. Therefore, a data shipment necessary for running the simulations must be transferred to the executing processor as and when one becomes available.

When this project was started simulations were run on a cluster of 4 machines running SGI IRIX 6.5, each with 8 500MHz MIPS R14000 processors and 8GB of shared memory. Job submission was through Condor[4] (Litzkow et al. 1988), a specialized workload management system, or 'resource broker' for computationally intensive jobs. Condor provides resource monitoring, resource management and a job queuing mechanism. Users submit their parallel computing jobs to Condor, which places them in a queue and chooses which resources to use

---

[3] http://www.ngs.ac.uk/access.html

[4] http://www.cs.wisc.edu/condor/

for the job. Condor is highly configurable, for example, it can be set up only to start a job when the keyboard has not been used for a specified period of time and to stop the job once a keystroke has been detected.

When using this cluster, the multiple BEAMnrc and DOSXYZnrc input files required for a simulation had to be created manually, as did the combining of output files following the simulation. Matlab[5] scripts were therefore written to 'split' input files. Output files were combined using the DOSXYZnrc 'IRESTART = 4' option, which combines the multiple outputs into a single 3D dose file. This option enables calculation of the overall uncertainty within DOSXYZnrc. Run-times took approximately 2.5 hours per IMRT segment for the BEAMnrc part of the run (when all processors were available) and an average of 1.5 hours per segment for DOSXYZnrc, times being dependent on segment size.

All MC simulations are now run on our recently developed RTGrid service[6] (Downes *et al.* 2009). The RTGrid system was designed to enable MC simulations of treatment plans using a variety of MC codes utilising resources as and when they become available. Access to the underlying HTC system is through a web interface, or 'portal' that facilitates job parameterisation and management. The running of the simulation is controlled by the 'experiment manager' that interacts

---

[5] http://www.mathworks.com

[6] https://rapanui.cs.condor.cf.ac.uk/gridsphere/gridsphere?cid=experimentstab

with the RTGrid database and monitors changes to the simulation status, such as whether the simulation is ‘pending’, ‘running’ or ‘completed’ (figure 2.2). The RTGrid system currently supports four resource brokers: (1) Condor, (2) Globus (Foster 2005), (3) GridWay (Huedo *et al*. 2005) and (4) a broker connecting to the NGS, referred to as the RTGrid broker.

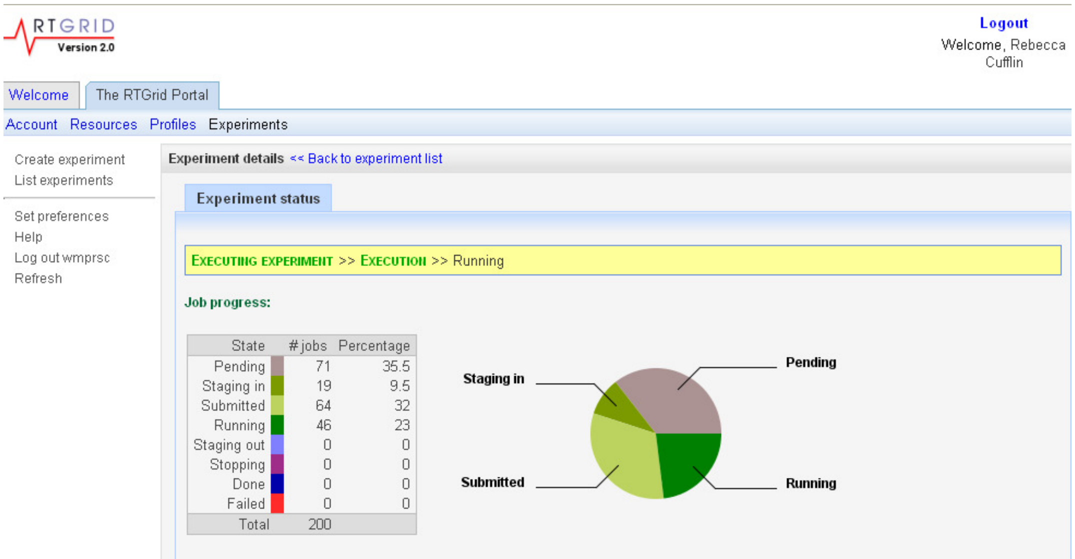

EXECUTING EXPERIMENT >> EXECUTION >> Running

Job progress:

State		# jobs	Percentage
Pending	🟫	71	35.5
Staging in	🟩	19	9.5
Submitted	🟩	64	32
Running	🟩	46	23
Staging out	🟦	0	0
Stopping	🟪	0	0
Done	🟦	0	0
Failed	🟥	0	0
Total		200	

Figure 2.2. An image of the RTGrid Portal showing percentage of simulations at each stage.

For the work in this thesis, jobs submitted via the RTGrid portal were submitted to the Cardiff University Condor pool of Windows XP SP2 PCs, of which between 200 and 1200 are available at any given time. The processors on the machines are mainly Pentium-4s, and memory varies amongst machines from 512 to 2048 MB. 200 of the machines are dedicated, whereas the remainder belong to departments within the university network and so are only available when not being used for other purposes.

For the experiment manager to successfully run an experiment the files have to be laid out in a particular way, but all other aspects, such as the splitting of input files into the required number for the simulations, the combination of the output files following completion of the simulation and the calculation of the overall uncertainty, are handled automatically.

The transition to running simulations on the RTGrid service, combined with a shift from running the IMRT segments in static mode to 'Step and Shoot' mode (see section 3.2) and the use of photon splitting as opposed to photon recycling in simulations, has resulted in a speed up of up to a factor of 10 for IMRT plans from the initial simulations run on the SGI cluster. The full forward exit dosimetry simulations described in Chapter 8 are particularly computer intensive due to the fact that the phantoms are required to be very large and of high resolution, and IMRT simulations for portal dosimetry have to be run beam by beam (IMRT plans consist of up to 14 beams). The RTGrid enables even these results to be obtained overnight, making this process feasible for clinical purposes.

2.2 An Introduction to Dose Calculation Algorithms

All IMRT plans carried out at VCC are currently planned and optimised on Oncentra MasterPlan (OMP, Nucletron, The Netherlands). OMP currently offers two dose calculation algorithms for photon beams, the pencil beam (PB) algorithm, and the collapsed cone (CC) algorithm (Ahnesjö and Aspradakis 1999). In addition, there are presently 2 version releases of each of these algorithms, the 'Classic' implementation, and the newer 'Enhanced' implementation.

PB and CC algorithms provide somewhat different methods and accuracies for calculation of the dose deposited within the medium by interactions with the incident radiation (see Section 2.2.2). In general terms the dose delivered to the patient or phantom is calculated by convolution of the energy released with pre-calculated energy deposition kernels, describing the dose distribution delivered by a primary photon in the volume surrounding its interaction point. Accurate calculation of the energy released requires knowledge of the energy fluence of the treatment beam.

2.2.1 Energy Fluence from a Clinical Beam

An energy fluence distribution denoted by $\psi_{tot}(x,y)$ is defined as the amount of radiant energy incident on area ΔA at position (x,y) traversing a plane perpendicular to the beam (equation 2.3), i.e.

$$\psi_{tot}(x,y) = \sum_{i} \frac{N_{Ei}(x,y) \cdot E_i}{\Delta A} \qquad (2.3)$$

where N_{Ei} (x,y) is the number of photons with energy E_i incident at (x,y) (Oncentra MasterPlan v3.3 Physics and Algorithms).

In clinical beams, the total energy fluence is comprised of both primary photons, and scattered photons from irradiated parts of the treatment head. The total energy fluence can therefore be represented as:

$$\Psi_{tot} = \Psi_{direct}(x, y) \cdot \eta(x, y) + \Psi_{indirect}(A :, x, y) \qquad (2.4)$$

where $\Psi_{direct}(x, y)$ is the open beam energy fluence of non-scattered photons directly from the source, $\eta(x, y)$ describes a possible modulation of the open beam of direct particles, *A* is a formal variable to represent the state of all the aperture setting parameters (for example, MLC settings), and $\Psi_{indirect}(A :, x, y)$ is the energy fluence of indirect photons scattered at least once in the treatment head ("head scatter"). Furthermore, the scatter part of the energy fluence can be divided into contributions from the flattening filter, the collimators and any auxiliary modulators, such as wedges, filters, blocks and trays (equation 2.5).

$$\Psi_{indirect} = \Psi_{\text{flattening filter}} + \Psi_{\text{collimators}} + \Psi_{\text{modulators}} \qquad (2.5)$$

In OMP the direct and head scattered energy fluences are calculated once and stored in separate 2D matrices for each beam, to be employed in patient dose calculations. The matrices are determined at a reference plane distance, usually the isocentre (100 cm from the effective radiation source). Beam divergence is considered by inverse square law scaling, using the target as the source origin focus for the direct fluence, and using the flattening filter as the effective focus for the indirect fluence (the flattening filter being the greatest source of scattered radiation).

The ‘enhanced’ versions of the photon dose calculations include more detailed modelling of the direct energy fluence. The resolution of the energy fluence grid is 1 mm in the enhanced implementation, but 2.5 mm in the ‘classic’ implementation. The enhanced version also includes much more detailed modelling of MLC rounded leaf-ends and inter-leaf leakage using ray-tracing methods. In the classic dose calculation algorithms the transmission through jaws and MLC leaves is included in the indirect (head-scatter) fluence, but in the enhanced algorithms this transmission is included in the direct fluence. A further advantage of the enhanced algorithms is the speed-up for IMRT dose calculations. The classic versions sum the individually calculated doses from each segment, whereas the enhanced versions sum the fluences for all segments in a beam, before performing a single dose calculation.

2.2.2 Dose Calculation using Convolution Kernel Models

The energy deposition by secondary particles around a primary photon interaction site is referred to as a point kernel. Convolution kernel models use the fact that in homogeneous media the point kernel is independent of location, making point kernels suitable for pre-calculation using MC methods. Convolution of these point kernels with the calculated TERMA (total energy released in the medium) for the clinical beam enables the dose within the medium to be calculated. The dose D to point r is given by:

$$D(r) = \int_{r'=-\infty}^{\infty} T(r')h(r - r')dr' \tag{2.6}$$

$$= \int \frac{\mu}{\rho}\psi(r')h(r - r')dr' \tag{2.7}$$

where T(r’) is the TERMA at r’, h(r – r’) is the point spread kernel about point r’, μ is the linear attenuation coefficient, ρ is the density and ψ(r’) is the primary photon energy fluence at r’. $\frac{\mu}{\rho}$ is known as the mass absorption coefficient of the medium.

KERMA (kinetic energy released in the medium) is a familiar term to those in the radiotherapy field and TERMA is analogous to the collision part of KERMA, k_{col}, (equation 2.8) as energy lost to radiative interactions are not included. The term TERMA was introduced by Ahnesjo *et al.* in 1987.

$$k_{col} = \frac{\mu_{en}}{\rho}\psi \qquad (2.8)$$

where $\frac{\mu_{en}}{\rho}$ is the mass energy absorption coefficient.

Full convolution dose calculations are very time consuming and unsuitable for dose calculation within a clinical setting. If the density matrix used for the patient dose calculation is composed of N^3 voxels, the number of calculations required to compute the dose contribution at each location from all the surrounding points would be N^6 (Mackie *et al.* 1998). For this reason further approximations are required. The CC algorithm is an approximation to a point kernel model designed to speed up dose calculations whereas the PB algorithm is based on pencil kernels.

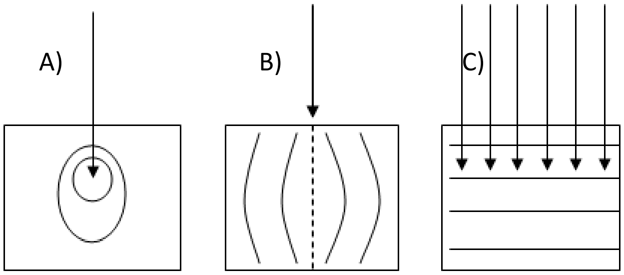

Figure 2.3. Energy deposition kernels. A) a point kernel B) a pencil kernel C) a planar kernel.

Figure 2.3 illustrates the different kernels used in clinical dose calculations. A point kernel describes the energy deposition in an infinite medium around a primary photon interaction site, a pencil kernel describes the energy deposition in a semi-infinite medium from a mono-directional pencil beam and a planar kernel is the energy deposition from a broad parallel beam.

Clinical situations are far more complex than those involving monoenergetic beams incident on homogeneous slabs. Polyenergetic kernels representing the clinical beam can be calculated as a sum of monoenergetic kernels with appropriate weights according to the spectrum of primary photons (Ahnesjo 1989), and point kernels can be scaled according to the density distribution (Mackie *et al.* 1985, Mohan *et al.* 1986, Ahnesjo *et al.* 1987). Off-axis beam softening and beam hardening at depth also need to be considered.

The CC algorithm is a full 3D superposition / convolution dose calculation algorithm based on point kernels. The algorithm gets its name from the fact that each point kernel is divided in 3-D into a number of variably spaced angular bins (or 'cones') and it is assumed that the energy released within each cone is transported only along its axis. As the energy released from a primary photon interaction is mainly concentrated in the forward direction, the density of cones in this direction is greatest. OMP typically uses 106 cones, 60 in the forward direction, 40 laterally and 6 in the backward direction from the kernel origin (figure 2.4), although this can be adjusted by the vendor upon request with a greater number improving accuracy at the expense of additional computation time.

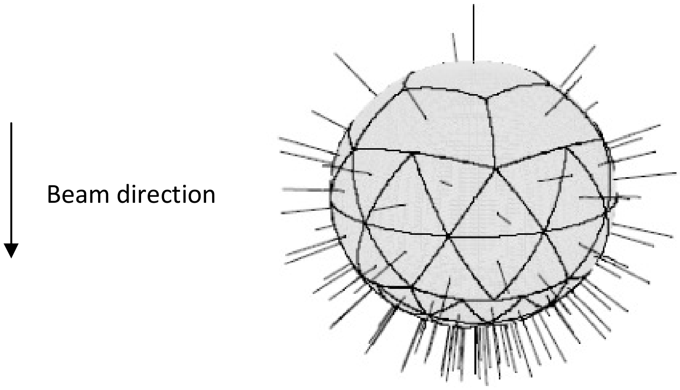

Figure 2.4. Angular binning of the point kernel in the CC algorithm for a beam vertically down. The algorithm gets its name from the fact that each point kernel is divided in 3-D into a number of variably spaced angular bins (or 'cones') and it is assumed that the energy released within each cone is transported only along its axis. (Image reproduced from Oncentra MasterPlan v3.3 Physics and Algorithms.)

A ray trace is performed to all calculation voxels (of 1 mm resolution for the enhanced algorithm, and of 2.5 mm resolution for the classic version), and the amount of radiant energy released in each voxel is determined. The TERMA is separated into 2 parts, the part due to energy released due to primary photons, and the scatter part, which is transported separately. The effects of beam hardening and off-axis beam softening are included in the ray trace.

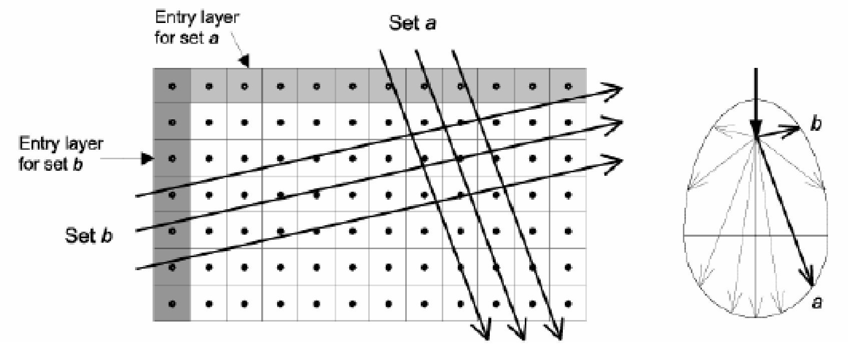

Figure 2.5. The parallel lines along which the energy released is transported in the CC algorithm. The dots at the centre of each voxel represent the TERMA calculation points. (Image reproduced from Oncentra MasterPlan v3.3 Physics and Algorithms.)

The discretised point kernels are then used to transport the energy released, until the energy is deposited as absorbed dose. The transport is performed along sets of parallel lines, or pipes, each set corresponding to a specific direction of the discretised point kernel (figure 2.5). The number of pipes in each set is determined by the requirement that each voxel should be passed by at least one pipe in the set. For each voxel encountered along a pipe the energy absorbed in the voxel is calculated and the energy released in the voxel in the direction of the transport line is added. For each direction the kernels are parameterised by

$$h(r) = \frac{Ae^{-ar}}{r^2} \qquad (2.9)$$

where *r* indicates the distance to the interaction point, *a* describes the range of energy transport from the interaction site, and *A* represents the fraction of energy transported in the given direction per unit solid angle. Two sets of point kernels are used in OMP, one to redistribute the energy released due to primary photons (to give the primary dose), and one to redistribute the energy released due to scattered photons (to give the phantom scatter dose). Both sets of kernels are scaled for the presence of heterogeneities. Due to the beam divergence, a kernel tilt correction is also applied.

The calculation time is proportional to the number of directions used for kernel discretisation (M) and the number of voxels (N^3). Increasing both the number of directions and the number of voxels would increase accuracy, at the expense of calculation time (equation 2.10).

$$\text{Calculation time } \alpha \ N^3M \qquad (2.10)$$

Pencil kernels form the basis of the PB algorithm and result in a considerable speed up of calculation time. The PB algorithm within OMP calculates dose within the patient using a one dimensional convolution along fan–lines. Depth dose curves are used to obtain an effective energy spectrum for clinical beams, which in turn is used to obtain poly-energetic pencil kernels, derived by superposing mono-energetic kernels. At each depth z, the poly-energetic energy deposition kernel in OMP is parameterised as

$$\frac{p}{\rho}(r,z) = \frac{A_z e^{-a_z r} + B_z e^{-b_z r}}{r} \qquad (2.11)$$

where A_z, a_z, B_z and b_z are depth dependent parameters determined by least square fitting. a_z is larger than b_z and so the two terms are interpreted as the dose components due to primary dose and scatter dose. Separating the kernel into primary and phantom scatter dose fractions in this way improves the heterogeneity correction, an equivalent path length correction being used for the primary dose contribution (Ahnesjö and Trepp 1991, Ahnesjö *et al.* 1992, 2005).

The PB algorithm is known as a ‘type a’ algorithm, and CC as a ‘type b’ algorithm (Knöös *et al.* 2006). Type a algorithms are primarily based on equivalent path length scaling for inhomogeneity corrections and do not account for the effects of lateral and backscattered radiation, whereas type b algorithms model lateral scatter (in an approximate way). Type a algorithms therefore have known limitations in heterogeneous media, particularly in close proximity to tissue boundaries. In regions with few inhomogeneities, such as the prostate, studies have shown there to be only minor differences between dose distributions calculated by type a and type b algorithms (Aspradakis *et al.* 2003, Knöös 2006). The more heterogeneous the region the greater the advantage of moving to a more sophisticated calculation algorithm. It should also be noted that the CC method in OMP calculates dose to the actual medium, as does MC, rather than dose to water. Average CC doses are therefore 1-2% lower than PB doses for all treatment sites as the dose to soft tissue is about 1–2% lower than in water due to slight differences in atomic composition and hence mass energy absorption coefficients.

Chapter 3

Monte Carlo Modelling of the Linear Accelerator and Multi-Leaf Collimator

3.1 Monte Carlo Modelling of the Linear Accelerator

3.1.1 Introduction

This chapter will describe the MC modelling of the Varian 2100CD linacs at VCC. VCC currently has three 2100CDs, capable of treating both 6 MV and 10 MV photon ‘energies’[7]. These three linacs are matched (i.e. tweaked to produce the same energy and beam data) to enable transfer of patients between machines to maximise efficiency and ensure continuity of patient treatments in the event of a machine requiring repair. Conventionally 6 MV is used to treat the thinner regions

---

[7] By convention, the voltage is used to characterize X-ray beams, there being a spectrum of energies up to the maxima of 6 MeV and 10 MeV.

of the body, such as the head and neck region, and 10 MV to treat the thicker areas such as the pelvis region due the increased penetration at higher energy. The aim of this work was to model these linacs accurately to enable simulation of clinical IMRT plans.

3.1.2 Methods

This project began with the modelling of the Varian 2100CD linac in 10 MV mode using the BEAMnrc software, the linac in 6MV mode previously being modelled and validated as part of an earlier project (Spezi and Lewis 2002, Spezi 2003, Chin *et al.* 2003, Chin *et al.* 2005). This required the confidential linac specification data, detailing the materials and dimensions of all linac components provided by the vendor, Varian Medical Systems. Component modules SLABS, CONS3R, FLATFILT, CHAMBER, SLABS and JAWS were used to model the accelerator target, primary collimator, flattening filter, ion chamber, mirror and secondary collimators respectively. The MLC, one of the most challenging geometric structures to model in a linac head, was not included in the initial modelling and so is described in the next section. A parallel beam of monoenergetic electrons of energy 10 MeV and beam width 0.1 cm was initially used as these are the nominal values provided by the manufacturer.

Cross section dataset ICRU 521 was selected, corresponding to thresholds of secondary electron production of 0.01 MeV, based on material compositions and densities set out in ICRU Report 37 (1984). ECUT (the electron transport cut off) and PCUT (the photon transport cut off) were set to 0.7 MeV and 0.01 MeV respectively for linac simulations. DBS (see Chapter 2) was used to increase calculation efficiency, with a splitting number of 1000. Although the optimal setting for DBS would vary with the details of the accelerator being simulated, Kawrakow *et al.* (2004) suggest that setting a value of 1000 results in near optimum performance for all set-ups, adjustments around this value possibly increasing efficiency at most by 15%.

In 2003 Verhaegen and Seuntjens presented a topical review of MC modelling of external photon beams. They suggested firstly fine tuning the primary electron energy by plotting the depth dose of a (10 × 10) cm^2 field and comparing it with measured data. All measured data presented here were measured previously in a water tank, depth doses with a Scanditronix *RK* cylindrical ionization chamber with an active volume of 0.12 cm^3 and profiles with a Scanditronix photon diode. Once an energy match has been found, Verhaegen and Seuntjens then suggest fine tuning the width of the electron beam by plotting profiles of large field sizes in air or at shallow depths in a phantom. The spot size of the primary electron beam is a crucial parameter to which calculated dose and fluence distributions are sensitive.

Depth doses should be constantly checked to ensure that a change in the source size has not affected the energy of the emerging beam.

Depth doses ((10 × 10) cm^2 fields) and profiles ((35 × 35) cm^2 fields) were plotted in homogeneous water phantoms created using DOSXYZnrc. The primary electron energy was varied between 9.5 and 10.5 MeV and the source size varied between 0.5 and 2.5 cm until the best match was obtained. A wider range of profiles were then plotted in order to verify the match. Depth doses were normalised at 10 cm deep and profiles at 9 cm deep, the percentage depth dose being applied in order to retain the dose relative to the maximum dose on the central axis (d_{max}). All comparisons between Monte Carlo and measured data were carried out using Matlab software.

At the time this work was initiated it was thought that IMRT prostate treatments, like conventional prostate treatments, would be planned and delivered at 10 MV due to the increased penetration over 6 MV, hence the modelling of the linac in 10 MV mode. However, more recent experience has shown that IMRT dose distributions of equal quality can be obtained at 6 MV. 6 MV IMRT treatments are often recommended for a number of reasons such as minimising neutron production and improved TPS calculation for small beamlets (Welsh *et al*. 2007). Therefore a clinical decision was made at our centre that all IMRT treatments would be carried out at 6MV. As a result, most work in this thesis has been carried out using a model of a 6 MV linac, developed as a part of previous projects (Spezi and Lewis 2002, Spezi 2003, Chin *et al.* 2003, Chin 2005). The 10 MV model has however been validated and is available should the clinical need arise. For completeness, the results of measurement versus the MC 6 MV model have also been included here. The 6 MV and 10 MV linac models are very similar, the only differences being the energy, source size, target and flattening filter design and composition.

In the latter stages of this project, photon splitting was introduced within DOSXYZnrc simulations using 'ISOURCE9' (a full linac simulation source, as described on page 17). As stated in Chapter 2, Kawrakow and Walters (2006) found that use of photon splitting increases the dose calculation efficiency by a factor of up to 6.5, although the optimum value varies with machine and simulation parameters, efficiency being given by equation 3.1. Therefore the optimum value of photon splitting for our set-up was determined.

$$e = \frac{1}{s^2 T} \qquad (3.1)$$

where e is the efficiency, s the uncertainty and T the CPU (Central Processing Unit) time.

Additionally, a jaw position dependent correction for backscatter from the linear accelerator collimating jaws to the monitor chamber has to be performed for Varian linacs. The method used was that devised by Liu *et al.* (2000), who used MC simulations to calculate the ratio of backscattered radiation to forward radiation at the monitor chamber. The amount of backscattered radiation for any field setting was then computed as a compound contribution from both the X and Y jaws, which was used to calculate the change in photon output. Liu *et al*. found a 2% increase in photon output when increasing the field size from (10 × 10) cm^2 to (40 × 40) cm^2.

3.1.3 Results

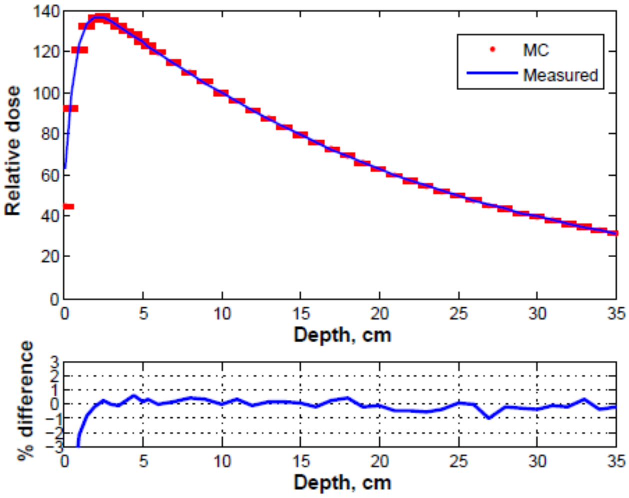

Figure 3.1. Monte Carlo depth dose for 10.2 MeV primary electron beam compared with measured data, normalised at 10 cm deep. Vertical error bars are shown indicating ±1 SD on MC data.

The best match between MC simulation and measurement was found for a primary electron energy of 10.2 MeV and source width of 0.11 cm. These values compare relatively well with those determined by Sheikh-Bagheri and Rogers (2002) i.e. a beam energy of 10.5 MeV and source size of 0.15 cm. The MC and measured percentage depth dose curves are given in figure 3.1, differences between measured and MC data being generally within 0.5%.

The effect of modifying the source width (for a circular source) on the 10 MV beam profile is shown in figure 3.2 below, the black profiles representing measured data, the red, green and blue plots representing the MC data for source sizes of 0.10, 0.18 and 0.24 cm respectively. The profiles correspond to depths of 2.5, 9, and 15 cm. This diagram demonstrates the importance of plotting profiles at shallow depths or in air when estimating the source size, shallow profiles being much more sensitive to any changes. The final MC profiles, for a 0.11 cm source size, versus measurement are given in figures 3.3 and 3.4.

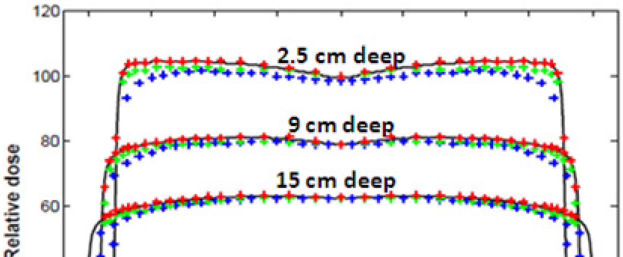

Figure 3.2. Effect of changing the width of the primary electron beam on profile shape. The effect is more visible at shallow depths. The curves were normalised at 9 cm deep and the percentage depth dose applied in order to retain the dose relative to d_{max}.

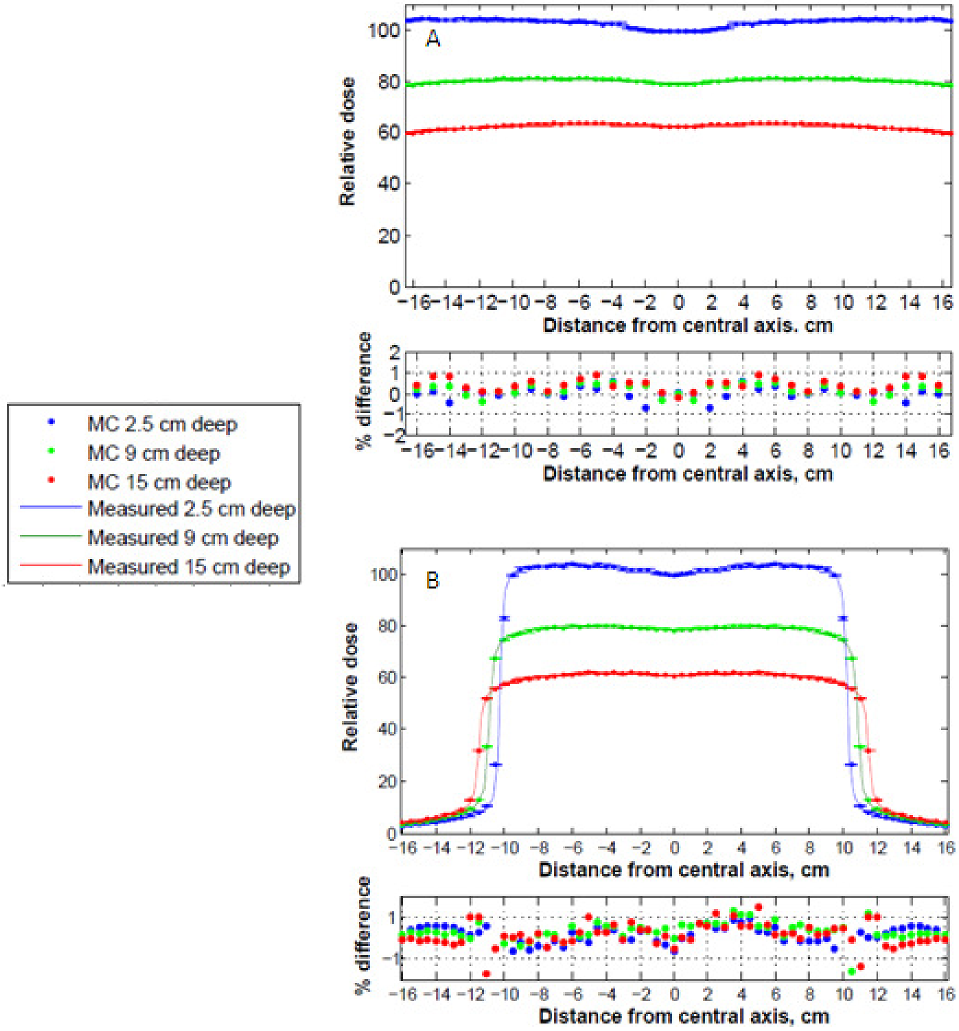

Figure 3.3. Y direction Profiles demonstrating the agreement between MC and measurement for the 10 MV MC model, 0.5 cm voxels A) 35 cm × 35 cm and B) 20 cm × 20 cm field. The curves were normalised at 9 cm deep and the percentage depth dose applied in order to retain the dose relative to d_{max}.

In recent years there have been numerous discussions on using elliptical sources for MC models (Huang *et al*. 2005, Kim 2009). However, as very good agreement between MC simulation and measurement was obtained it was not felt that this warranted investigation (figures 3.3 to 3.6 show profiles plotted in the y direction, and figures 3.11 and 3.12 in section 3.2 show profiles plotted in the x direction).

Additionally, although the focus of the paper by Kim (2009) is elliptical sources, they find a symmetric source of 0.2 mm to be the best match for their Varian 21EX linac.

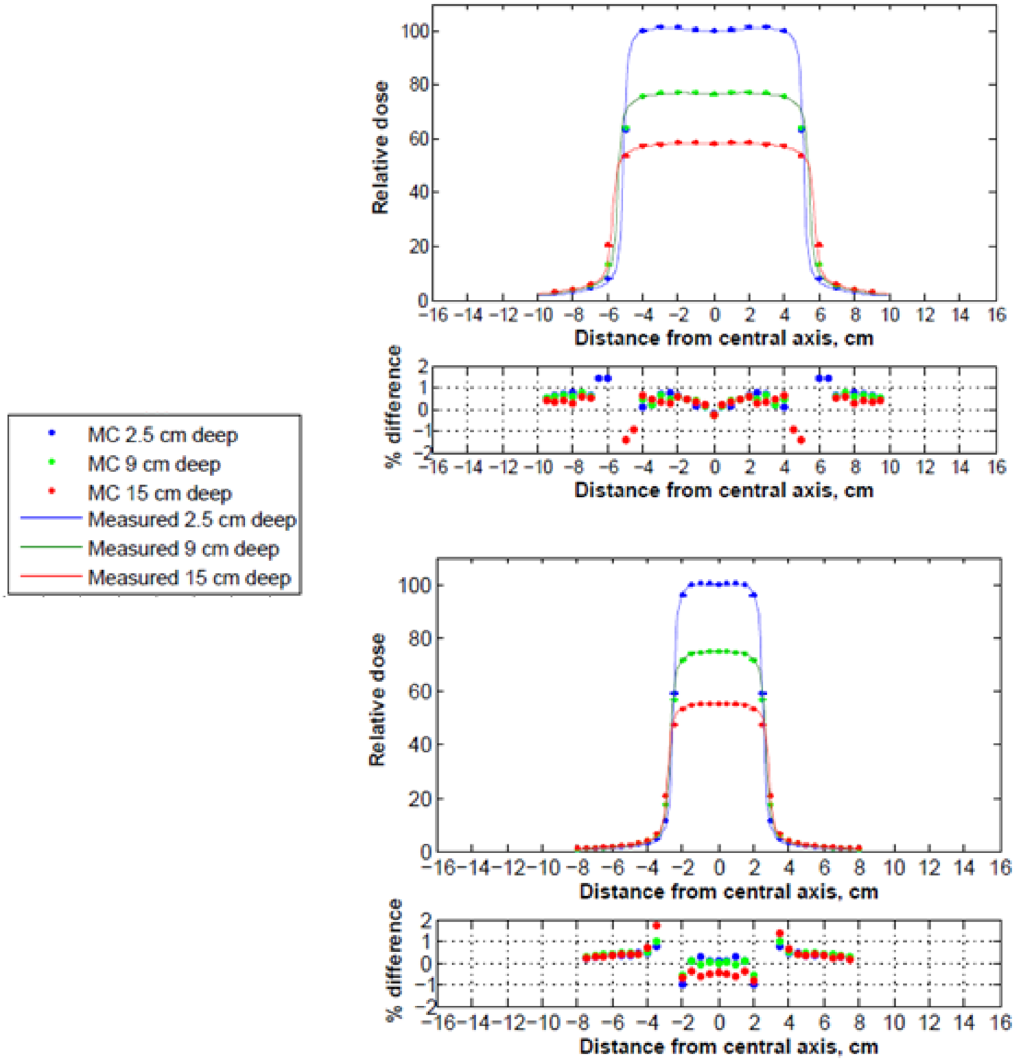

Figure 3.4. Y direction profiles demonstrating the agreement between MC and measurement for the 10 MV MC model, 0.5 cm voxels A) 10 cm × 10 cm and B) 5 cm × 5 cm field. The curves were normalised at 9 cm deep and the percentage depth dose applied in order to retain the dose relative to d_{max}.

Figures 3.5 and 3.6 show profiles plotted for the 6 MV model, the primary electron energy and electron beam width being set at 6.0 MeV and 0.1 cm respectively.

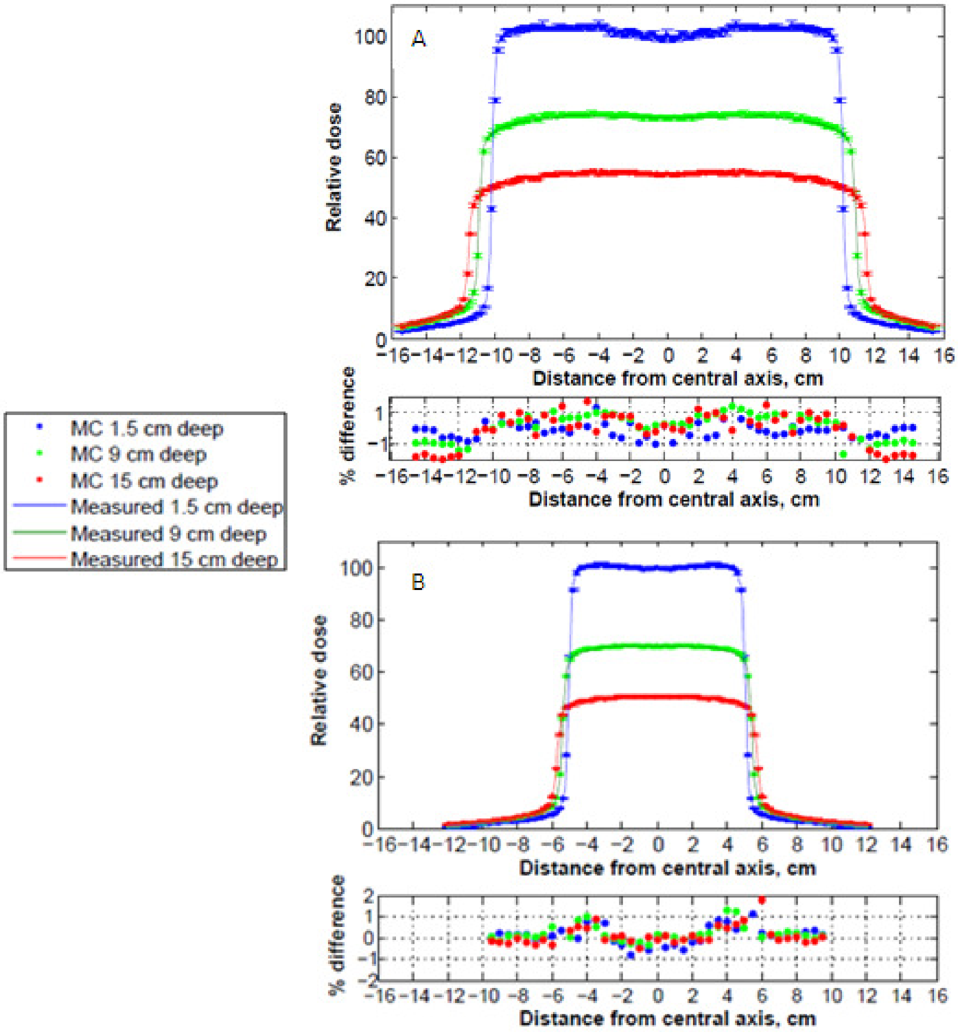

Figure 3.5. Y direction profiles demonstrating the agreement between MC and measurement for the 6 MV MC model, 0.2 cm voxels A) 20 cm × 20 cm and B) 10 cm × 10 cm field. The curves were normalised at 9 cm deep and the percentage depth dose applied in order to retain the dose relative to d_{max}.

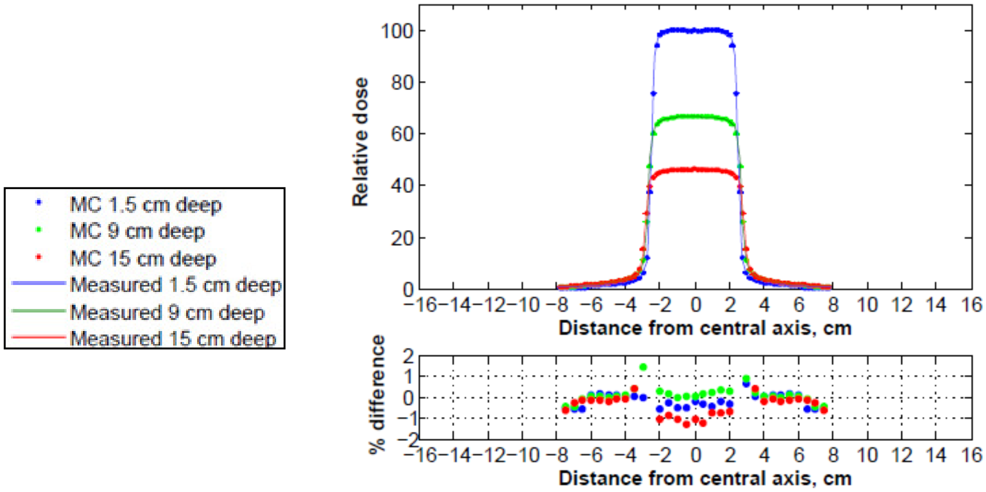

Figure 3.6. Y direction profiles demonstrating the agreement between MC and measurement for the 6 MV MC model, 0.2 cm voxels, 5 cm × 5 cm field. The curves were normalised at 9 cm deep and the percentage depth dose applied in order to retain the dose relative to d_{max}.

The optimum photon splitting number for our linear accelerator model (using a linear accelerator source) was found to lie between 75 and 100 (figure 3.7), efficiency being calculated using equation 3.1. Efficiency was improved by a factor of almost 10.5 for splitting numbers of both 75 and 100 when compared to simulations with no splitting. A splitting value of 100 is currenly used in all MC simulations.

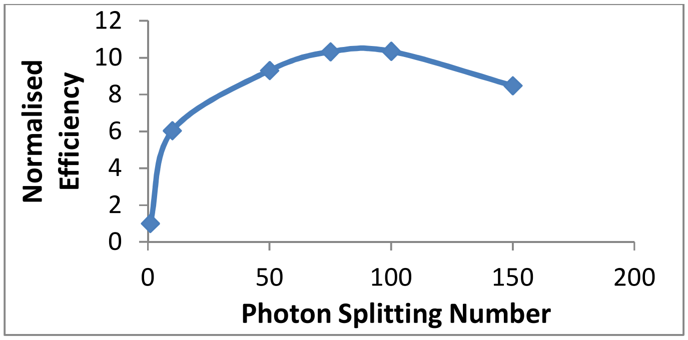

Figure 3.7. Normalised efficiency versus photon splitting number used in simulations.

Figures 3.8 and 3.9 demonstrate the agreement between MC generated field size output factors with and without the correction for backscattered radiation to the monitor chamber, using the method devised by Liu *et al*. 2000. It can be seen that inclusion of this correction greatly improved agreement between MC generated field size output factors and measurement, both at 6 MV and 10 MV. Correction factors, normalised to a (10 x 10) cm^2 field, varied from 0.99 for a (5 x 5) cm^2 to 1.013 for a (20 x 20) cm^2 field.

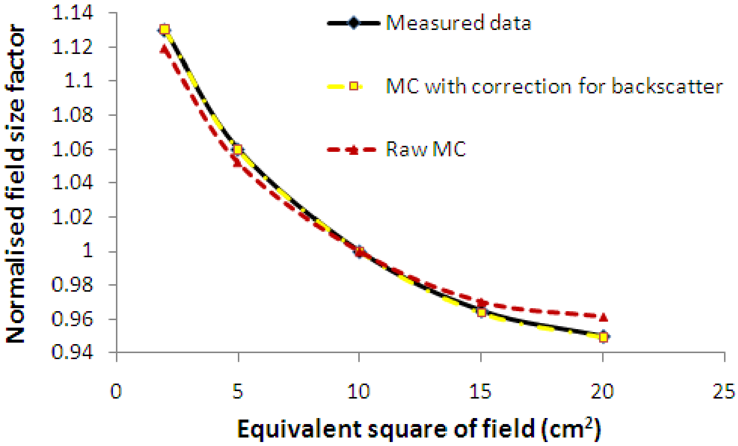

Figure 3.8. MC generated field size factors versus measurement, with and without correction for backscattered radiation to the monitor chamber at 6 MV.

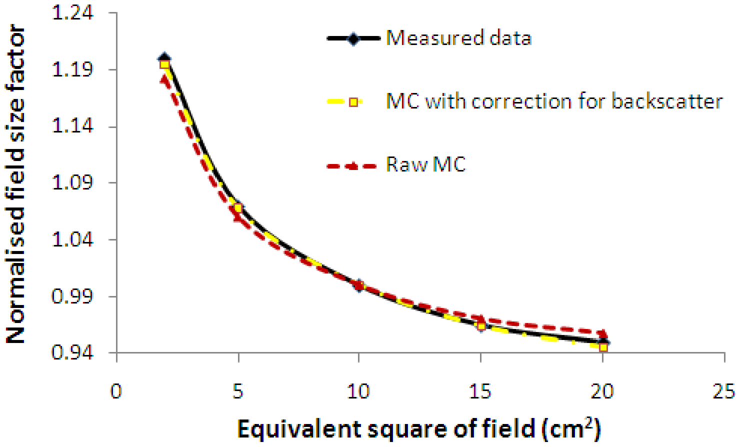

Figure 3.9. MC generated field size factors versus measurement, with and without correction for backscattered radiation to the monitor chamber at 10 MV.

3.1.4 Discussion

Experimental data presented here were measured in a water tank, depth dose measurements with a Scanditronix RK chamber and profile measurements with a Scanditronix photon diode. Before matching a MC model of a linac to acquired data, the validity of the measured data must be verified. This is because experimental set-up and corrections for the effective point of measurement of the chamber make a critical difference, especially in the build up region.

The profile and depth dose plots show there to be very good agreement between measurement and MC simulation, both at 6 and 10 MV (see figures 3.1 and 3.3 to 3.6). The linac models were identical with the exception of the initial electron energy, source size and composition and design of the flattening filter and target. A photon splitting number between 75 and 100 was found to be the optimum for our linac configuration.

3.2 Monte Carlo Modelling of the Multi-Leaf Collimator

3.2.1 Introduction

To enable the verification of IMRT fields, a MC model of the Varian 120 leaf Millennium MLC was required. The Millennium 120 leaf MLC (figure 3.10) is an updated version of the Millennium 80 leaf MLC with 60 leaves on each bank. The central 20 leaves on each bank are 0.5 cm wide (projected to isocentre distance), with 10 × 1 cm wide leaves either side of these central leaves. This model of MLC therefore allows for finer modulation within the central $(20 \times 20)\ \text{cm}^2$, IMRT field sizes very rarely being much larger than this.

When the Millennium MLC DYNVMLC component module was initially released within BEAMnrc (Heath and Seuntjens 2003), the only option was to run simulations in ‘static’ mode. More recently the option to run simulations in ‘step and shoot’ mode has been released enabling multiple segment IMRT beams to be simulated in a single simulation, random number generators being used to sample the probability of each segment being simulated based on the segment weight.

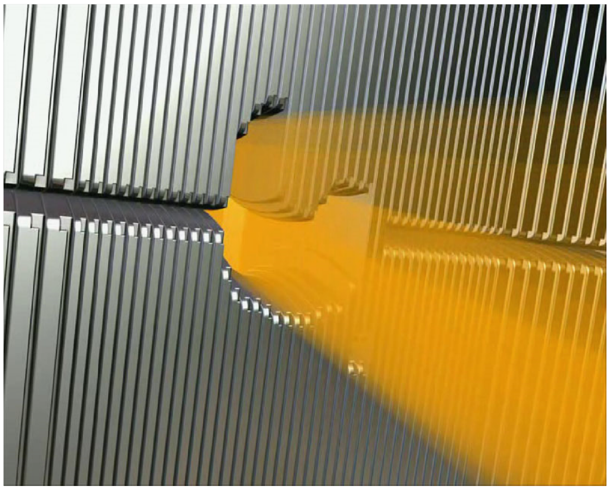

Figure 3.10: Varian 120 leaf Millennium MLC, the central 40 leaves on each bank being narrower than the outer 10 leaves at each end (image courtesy of Varian).

3.2.2 Methods

The MLC was fully modelled using the DYNVMLC component module (Heath and Seuntjens 2003). This component model includes details such as the leaf driving screw hole, support railing groove and leaf tips. Heath and Seuntjens compared interleaf leakage profiles for this CM and an equivalent leaf model using the older VARMLC CM and demonstrated that the simplified geometry of VARMLC is not able to predict the details of the MLC leakage accurately for the 120 leaf collimator.

For IMRT treatments with many segments, leaf transmission and leaf inter-leaf leakage become important factors in patient dose calculations. In IMRT a significant fraction of dose to critical structures is due to radiation scattered from, or transmitted through, the MLC (Mohan *et al.* 2000, Kim *et al.* 2001). In addition, leaf position accuracy is paramount (Budgell *et al.* 2000). Therefore, during commissioning of an MLC, leaf transmission, inter-leaf leakage, leaf abutment leakage and leaf position are all significant factors that must be verified. The field shape in figure 3.11 and 3.12 enables verification of rounded leaf end position and leaf transmission relative to the open field dose. The closed field shape shown in figure 3.13 was used to verify both inter-leaf leakage and leaf end abutment leakage. Additionally, the density of tungsten in the simulations was modified as previous work at our centre (Spezi 2003) found that this was necessary for the older 80 leaf MLC.

3.2.3 Results and Discussion

As with previous work carried out at our centre (Spezi 2003) good agreement between simulation and measurement was found with a tungsten density of 17.5 g/cm^3. When the standard ICRU tungsten density was used leaf transmission was underestimated by about 4%. Figures 3.11 and 3.12 demonstrate the efficient modelling of the rounded leaf ends and the dose under the MLCs relative to the open field dose. Figure 3.13 demonstrates the ability of the MC MLC to model the leakage between abutting MLC leaves and inter-leaf leakage. The maximum measured inter-leaf leakage was 2.3%, compared to a maximum simulated value of 2.4%. It can also be seen from figure 3.13 that there is large variation in measured leakage for different leaves, due to very slight physical differences in reality, and so exact modelling would not be possible without tediously re-writing the whole component module for every individual MLC.

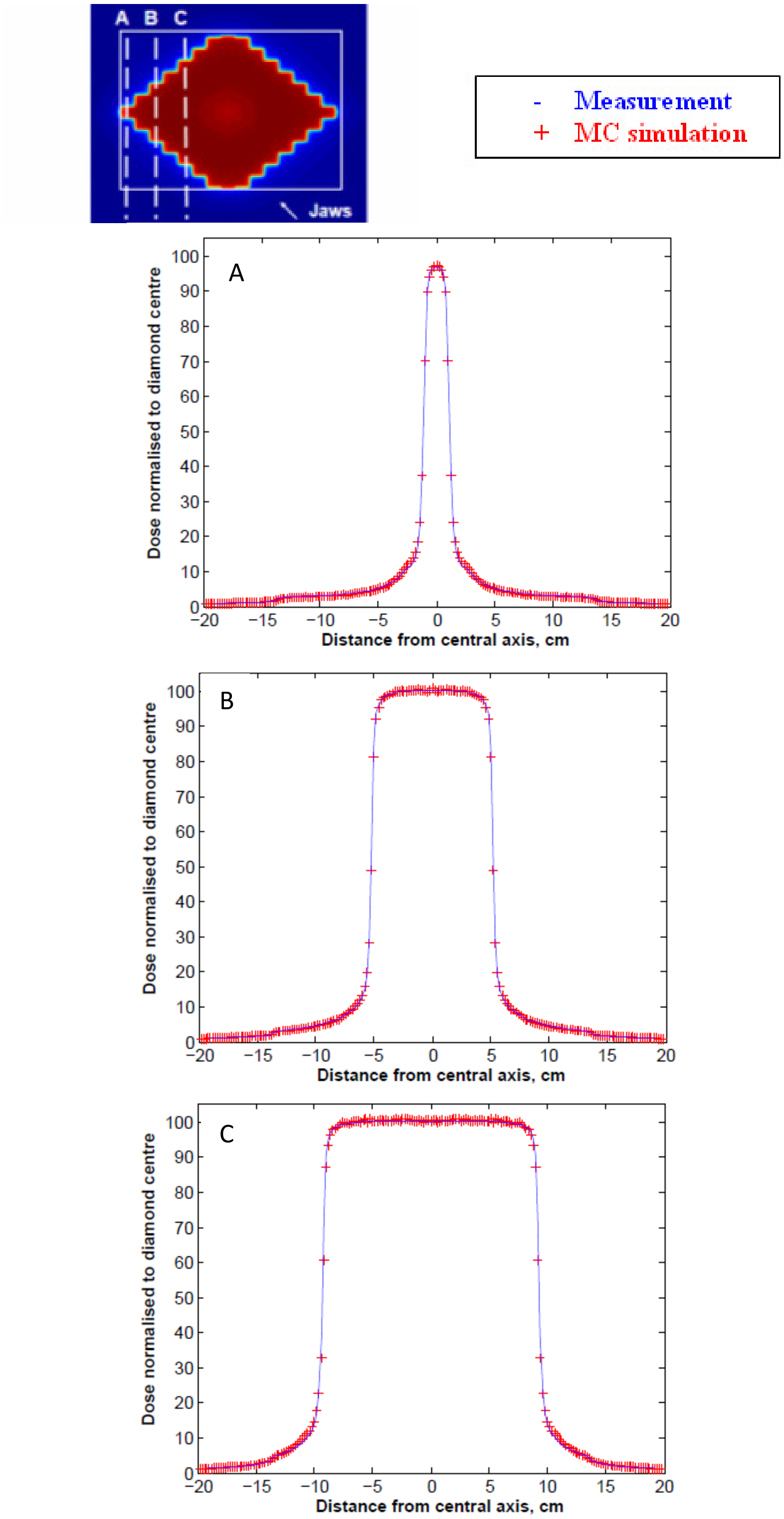

Figure 3.11. Profile cuts across a diamond shaped field to demonstrate agreement of leaf transmission between MC and measurement at 10 MV.

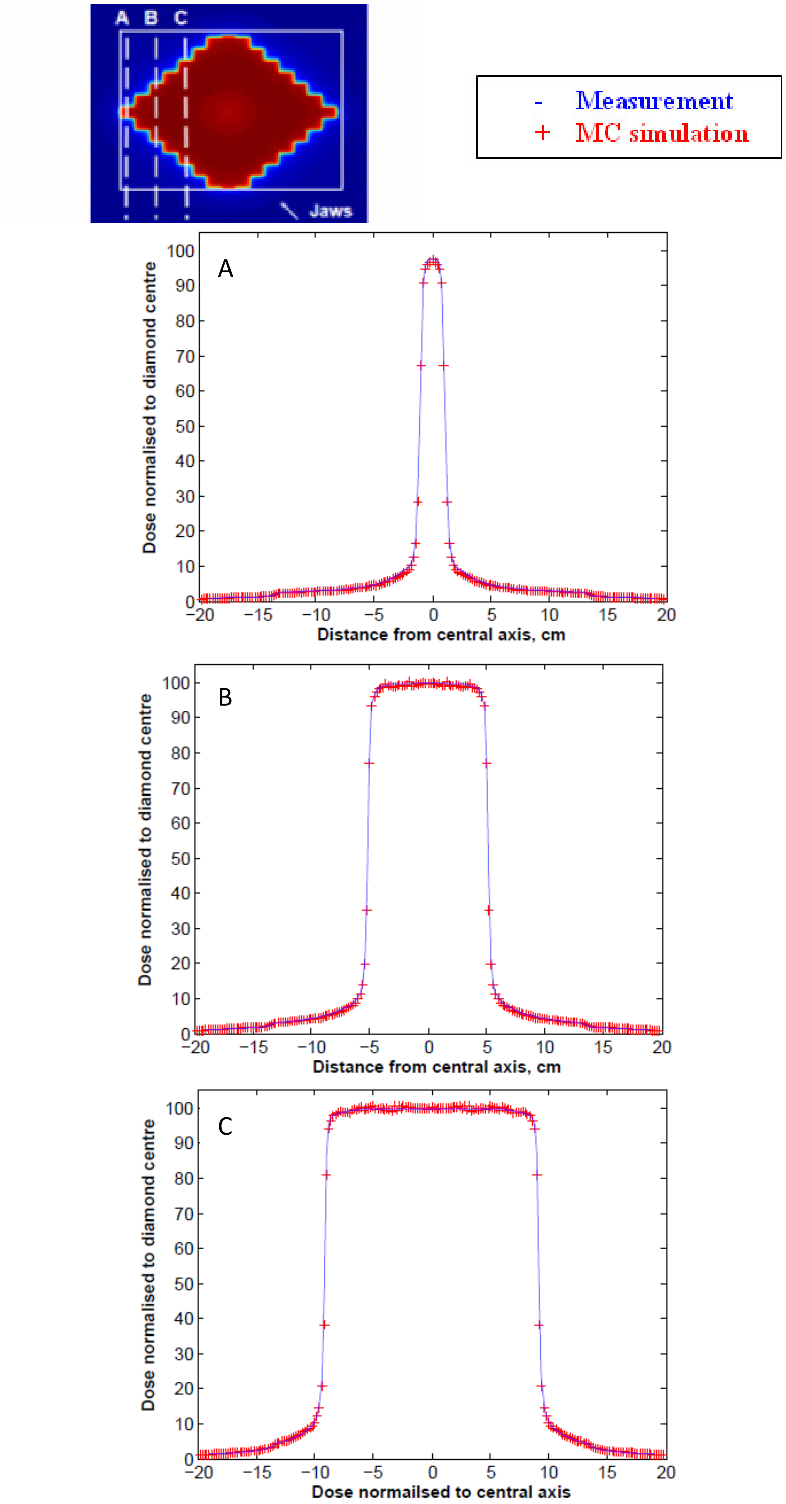

Figure 3.12. Profile cuts across a diamond shaped field to demonstrate agreement of leaf transmission between MC and measurement at 6 MV.

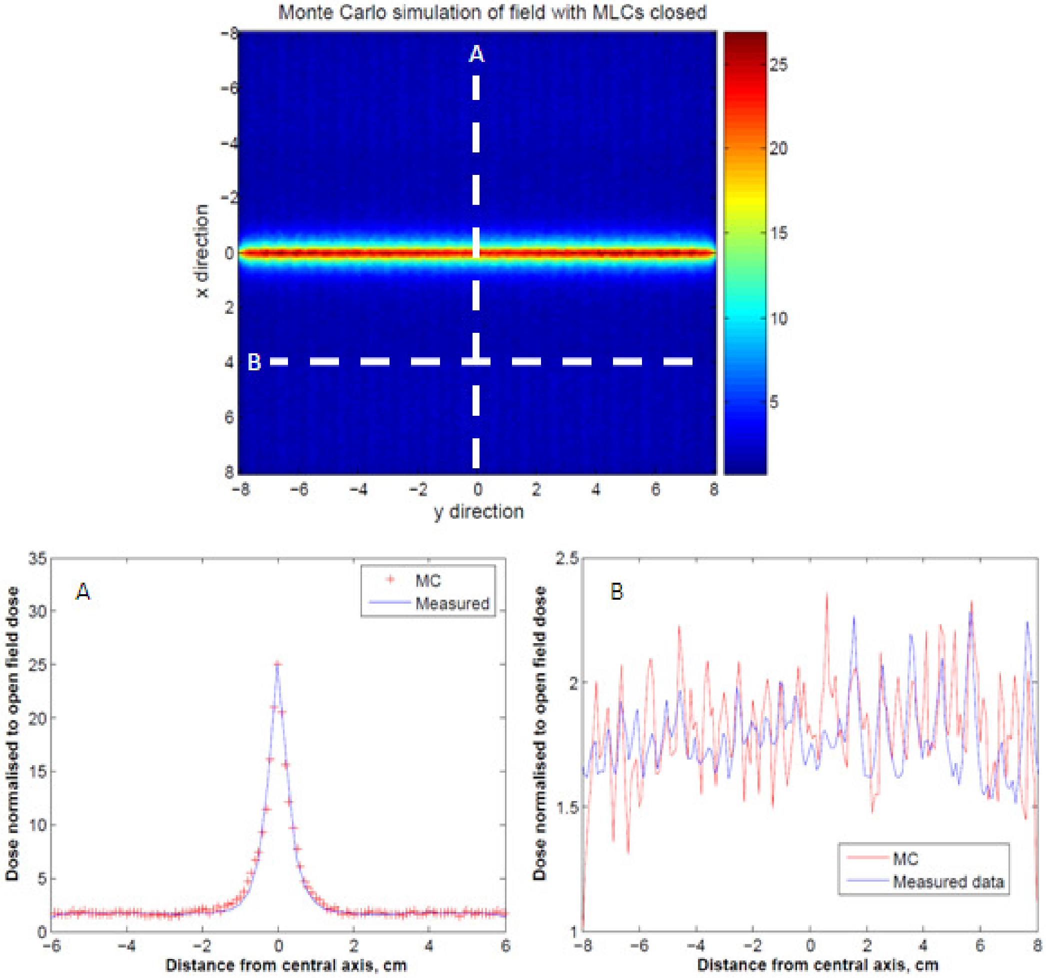

Figure 3.13. Profile cuts across 10 MV beam with closed MLCs, dose being expressed as a percentage of the open field dose. A) Profile cut in x direction. Dose at the leaf abutment position was found to be 25% of the open field dose. B) Profile cut in y direction under MLCs. Maximum inter-leaf leakage for the MC model was found to be 2.4%, comparing well with the measured value of 2.3%. It can be seen that there is large variation in measured leakage for different leaves.

Chapter 4

Monte Carlo Modelling of EPID

4.1 Introduction

As stated in the introduction, there are a number of EPID dosimetry approaches published in the literature, both pre-treatment to verify delivery before treatment commences and transit dosimetry to verify delivery during treatment of the patient. Most portal dosimetry techniques employ either empirical methods (with correction factors applied for non-water equivalence (Nicolini *et al.* 2006)) or superposition / convolution methods (with kernels derived either from extensive measurements (Chen *et al.* 2006, Wendling *et al.* 2006) or MC simulation (McCurdy *et al.* 2001, Warkentin *et al.* 2003, Steciw *et al.* 2005, Li *et al.* 2006)).

At our centre we have for several years been developing approaches involving full forward MC calculation of portal dose (Spezi and Lewis 2002, Chin *et al.* 2004, Chin *et al.* 2005) along with some centres elsewhere (Siebers *et al.* 2004, Parent *et al.* 2006, Parent *et al.* 2007). A detailed MC model of the linac, in combination with the EPID, enables the dose to the detector to be predicted accurately, without the need for scatter approximations or conversion to dose in water, achieving versatility difficult to accomplish by any other technique.

The main components common to modern a-Si EPIDs are (i) the (typically 1 mm thick) copper plate, which converts photons to high energy electrons and absorbs low energy scatter (ii) the terbium doped gadolinium oxysulphide (Gd_2O_2S:Tb) scintillating screen, which converts electrons to optical photons (iii) the a-Si photodiodes, which detect the optical photons (iv) the thin-film transistors within a glass substrate that store an amount of charge that is proportional to the amount of light received by the photodiode. An ideal detector would be water equivalent (as this is the reference medium for radiation dosimetry) but the high atomic number components present in these EPIDs prevent them from being approximated accurately by a water model.

As well as accurately modelling radiation transport from the linac to the EPID it is important to take account of other factors which contribute to the overall accuracy of the result. Two aspects in particular are considered in this work.

1) Backscatter into the radiation-sensitive layer of the detector from ancillary components such as support arm and cabling. This is particularly important when IMRT fields cover a large proportion of the active area of the EPID, which is the case for all IMRT plans currently delivered at our centre.
2) The linearity of EPID response with dose for different dose-rates, as there is a requirement to deliver treatments at the highest possible dose rates to facilitate throughput.

The Varian imager considered in this work has a support arm which has been reported to cause difficulties in portal dosimetry, primarily in the inline direction, due to non-uniform backscatter from supporting structures (Siebers *et al.* 2004, Ko *et al.* 2004, Moore and Siebers 2005, Greer *et al.* 2009, Wang *et al.* 2009, Cufflin *et al.* 2010a). Various solutions to this issue have been presented in the literature. Ko *et al.* (2004) suggested adding material downstream of the EPID phosphor to make the backscatter being detected more uniform, and Greer *et al.* (2009) devised a method to remove the backscatter component from the pixel sensitivity flood field correction matrix, retaining only field specific backscatter in the images. The solution proposed, as set out below, is to incorporate in an approximate way the backscattering components into the MC model of the EPID itself. Figure 4.1 shows a schematic diagram of the linac and EPID with supporting structures and figure 4.2 shows images of the EPID and supporting structures.

Dose-rate dependent EPID saturation effects have been reported previously in the literature (van Esch 2004). Also, IMRT overshoot and undershoot delivery errors from certain linacs are known to increase with dose-rate (Ezzell and Chungbin 2001, Grigorov *et al.* 2006, Kuperman and Lam 2006). These effects have been verified using a combination of ionisation and film dosimetry. With the desire to move to higher dose delivery rates to facilitate patient throughput, the ability of any dosemeter to detect dose-rate dependent treatment effects is paramount.

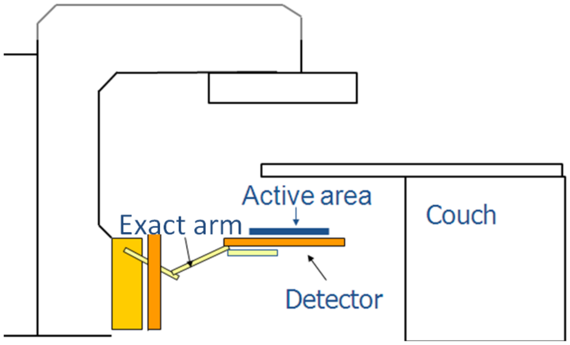

Figure 4.1. Schematric diagram of Varian linac and EPID with supporting structures.

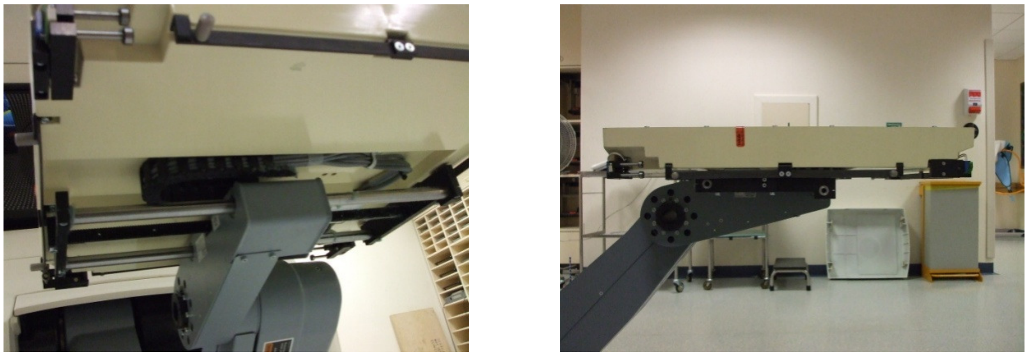

Figure 4.2. Images of the EPID and supporting structures.

4.2 Methods

This work was carried out on a Varian 2100CD linear accelerator with aS500 EPID on an 'Exact' arm. The BEAMnrc MC code (Rogers *et al.* 1995) was used to model the linac and DOSXYZnrc (Walters *et al.* 1996) to model the a-Si detector. Cross section dataset ICRU 521 was selected, corresponding to thresholds of secondary electron production of 10 keV, based on material compositions and densities set out in ICRU Report 37 (1984). ECUT and PCUT were set to 0.7 MeV and 0.01 MeV respectively for linac simulations. DBS was used to increase calculation efficiency (see Chapter 2), with a splitting number of 1000. All simulations were corrected for backscatter to the monitor chamber by the method described by Liu *et al.* (2000).

The DOSXYZnrc grid size in the X-Y plane was set to (2 × 2) mm^2 to decrease the run-time of the simulations (the photodiode spacing being 0.784 mm), with varying dimensions in the Z direction based on the vendor data supplied. This resulted in some loss of imager resolution, but as the imager was positioned at 140 cm source to detector distance (SDD) this corresponds to an effective pixel side of 1.4 mm at isocentre. For the detector simulations ECUT was set to 0.7 MeV as no significant difference was found between results with ECUT set to 0.521 MeV and 0.7 MeV, with 0.7 MeV offering a time saving factor of 1.6. PCUT was set to 0.01 MeV and so optical processes (conversion to light, transport of optical photons from the scintillator to the photodiodes and photodiode signals) were not simulated, but as the photodiode signals are proportional to the energy deposited in the phosphor screen this is the layer of interest in the simulations. The EXACT boundary crossing algorithm was used as this is known to be the most accurate, especially where charged particle equilibrium does not exist or where the phantom is split into non-uniform voxels (Walters and Kawrakow 2007). For calibration simulations requiring low uncertainty, 4×10^7 histories were simulated from the source and particles recycled within DOSXYZnrc to obtain uncertainties of less than 1%. For IMRT segments 2×10^7 histories were simulated from the source and particles recycled within DOSXYZnrc to achieve uncertainties of less than 2%.

The aS500 EPID has 512 × 384 pixels of 0.784 x 0.784 mm^2. The hardware version was IAS2 equipped with software version 6.1.11. The imager was set up for continual acquisition for all measurements ('IMRT Mode' with no pulse synchronisation). The signal generated by the incident photons is stored by the thin-film transistors until it is read out and digitised through an analogue to digital converter. Each of the 384 rows is scanned in sequence by the read-out electronics, 384 rows comprising an image 'frame'.

In this work the imager was positioned at 140 cm SDD for all measurements to minimise the saturation effect observed by others at higher dose rates and shorter

SDDs (van Esch *et al*. 2004), but also with the progression to transit dosimetry in mind. The standard Varian EPID calibration procedure was employed (equation 4.1).

$$\text{Corrected Portal Image} = \frac{\text{Portal Image - Dark Field Image}}{\text{Flood Field Image}} \times k_{\text{FFmean}} \qquad (4.1)$$

where k_{FFmean} is the mean pixel value for the flood field image. The dark field image is acquired with the radiation off and accounts for any electrical leakage and the flood field image is acquired with the radiation covering the detector area and corrects for individual cell sensitivities and electrometer gains.

4.2.1 Backscatter Modelling and Calibration

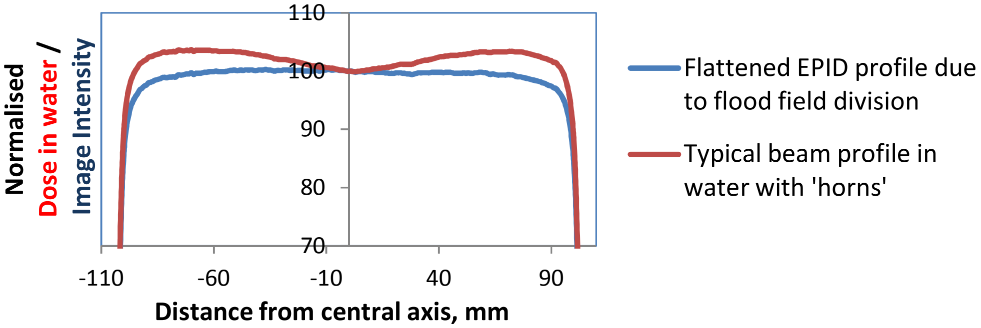

Figure 4.3. Large beam profile in water with beam 'horns' and large beam profile for an EPID image demonstrating the removal of the beam 'horns' by the standard Varian flood field calibration procedure.

The standard 'flood field' correction described above results in uniform 'flattened' images in which the beam 'horns' are removed (figure 4.3). This situation is easy to replicate for large symmetric fields by similarly dividing MC simulated images by a MC-generated flood image of the same size as the acquired flood image. However, the situation becomes far more complex for small fields or segments off-axis in the inline direction for which the scattering conditions become very different to the flood field situation. For example, for two (3 x 3) cm^2 beams centred at ± 6 cm off-axis, the non-uniform backscatter effect results in a 4% difference in image intensity (figure 4.4).

Initial simulations were carried out with a uniform slab of water equivalent material of thickness 2 cm to represent the backscattering material. This thickness was chosen because simulated and measured field size output factors (FSFs) agreed to within ± 1% on the central axis for the range of field sizes typically used (from (2 x 2) cm^2 to (20 x 20) cm^2). The solution devised to correct for non-uniform backscatter from the supporting structures involved adding water equivalent material to the back of the DOSXYZnrc EPID model and varying the thickness of material at every position until the simulated 'flood' images matched the acquired flood images, maximum differences at any position being within ± 2% over the entire imager area (ignoring any defective pixels). Figure 4.8 in the results section demonstrates the match of the acquired to MC generated flood images.

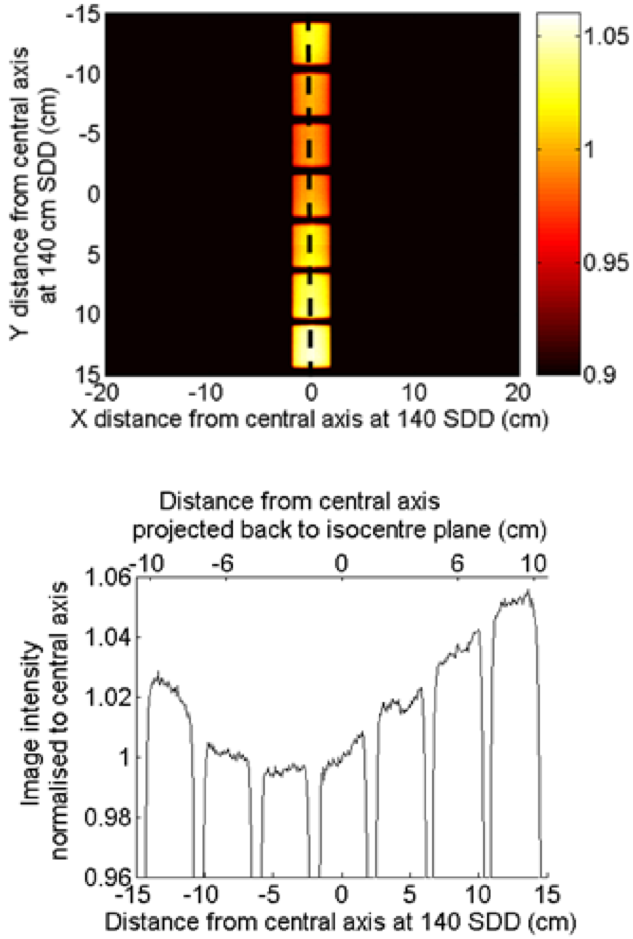

Figure 4.4. Profile cut through seven linearly aligned (3 x 3) cm^2 fields to demonstrate the effect of non-uniform scatter from EPID components on the intensity of small fields centred at different positions on the device.

The MC portal verification procedure was initially commissioned for simple, non-IMRT, symmetric fields of various sizes from (2 x 2) cm^2 to (20 x 20) cm^2 and delivered monitor units (MU) of 10 to 100 MU. Calibration curves converting MC dose to portal image pixel intensity were obtained for this MU range for a (10 x 10) cm^2 field at 100, 300 and 600 MU since the pulse repetition rates for these three dose rates are constant (see figure 4.5). Although a-Si EPIDs are reported to demonstrate reasonable response stability over time (Louwe *et al*. 2004, Budgell *et al*. 2007), two of the EPIDs at VCC are refurbished panels. Therefore regular image calibration is routine and a quick (10 × 10) cm^2 dosimetric calibration is performed in every week that dosimetric measurements are to be made. This weekly dosimetric calibration is consistent for all EPID work reported in this thesis.

To test the robustness of the MC model with devised backscatter solution, off-axis images of different field sizes were also evaluated. Figure 4.6 illustrates three (5 × 5) cm^2 images and three (2 × 2) cm^2 images at different positions in the inline direction to test the backscatter solution for off-axis small fields. These fields were created using the Varian ‘Shaper’ software and the collimator was rotated to 90°.

As unclean discharge and charge trapping, referred to as ‘ghosting’ and ‘image lag’, have been reported for a-Si EPIDs (van Esch 2004, McDermott *et al.* 2006a), a straightforward comparison of the magnitude of these effects at the three dose-rates being investigated was performed. A 5 MU (10 x 10) cm^2 irradiation was carried out immediately following a 100 MU (5 x 5) cm^2 irradiation and the increase in signal at the centre of the image was evaluated. In addition, McDermott *et al.* (2006a) reported non-linearity of system response due to image lag at low doses, and so the linearity of EPID response was evaluated for an extended range of MU from 5 MU to 500 MU at the two lower dose-rates of 100 and 300 MU min^{-1}.

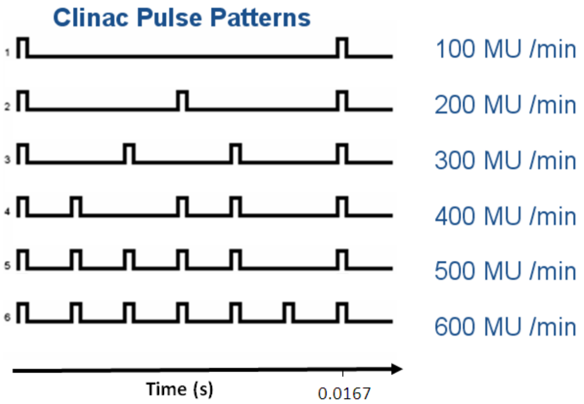

Figure 4.5. Varian Clinac Pulse Patterns.

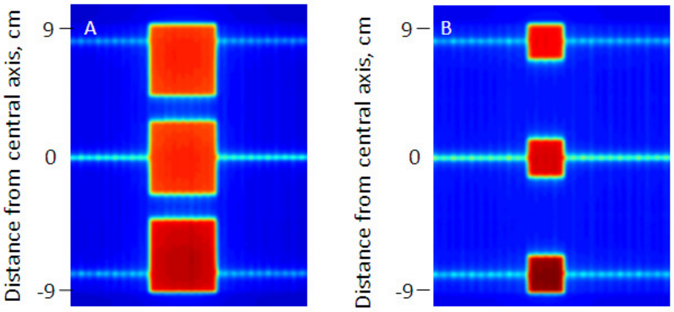

Figure 4.6. The location of A) three (5 × 5) cm^2 images and B) three (2 × 2) cm^2 images at different positions in the inline direction to test the robustness of the backscatter solution.

4.3 Results

The final EPID model (illustrated in figure 4.7) is composed of 28 layers of different materials based on data supplied by the vendor plus 4 additional non-uniform layers of water equivalent material (and air) to represent the differential backscatter. The solution found to minimise differences between simulation and measurement in the flood field data (as shown in figure 4.8) was asymmetric in both directions to represent the various components such as the imager support arm and cabling. The maximum thickness of water equivalent material was 5.5 cm to represent the imager arm, there being 5 cm backscattering material at the central axis. Although from figure 4.2 it can be seen that there is some additional wiring and casing to one side of the imager in the crossline direction, it is possible that the crossline asymmetry measured could be due to slight beam asymmetry, which would be very difficult to determine using this method without a rotation of the imager. However, as the magnitude of the crossline asymmetry (1%) is very much less than that in the inline direction (5%) the effect on the final results is negligible.

Figure 4.9 shows that the portal image calibration curves obtained at 100 MU min^{-1} and 300 MU min^{-1} were collinear in the range 10 MU to 100 MU to within 0.3% (0.3% being the maximum deviation from the line of best fit). In addition, figure 4.10 demonstrates the linearity of EPID response for the extended range of 5 MU to 500 MU (to within 0.8%) at 300 MU min^{-1}. The non-linearity at lower dose-rates reported by McDermott *et al.* 2006a was not observed on any of our Varian aS500 EPIDs. The 'kink' visible in the calibration curve for 600 MU min^{-1} (figure 4.9), corresponding to a loss of approximately 1 MU, occurs due to the transfer of the frame buffer to the CPU after the 64th frame, resulting in saturation of the 65th frame which appears longer as a result. (The vendor has informed us that upgrading to an IAS3 system eliminates these saturation effects due to the faster read-out of up to 30 frames per second compared with the maximum read-out of 15 frames per second with the IAS2 system). Although this loss of signal only corresponds to 1.5% for 65 MU, it becomes particularly significant for acquisitions where the 65th frame occurs during a low MU segment. For example, for an 8 MU segment this would correspond to 12.5% 'missing dose'. No decrease in signal caused by saturation of the 65th frame is visible for the 100 and 300 MU min^{-1} irradiations.

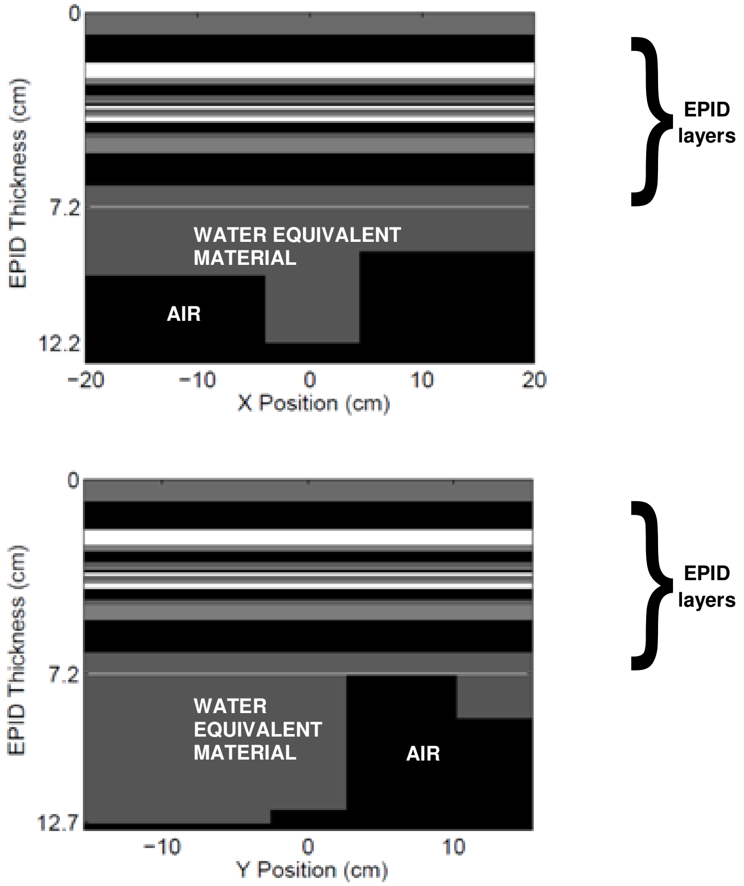

Figure 4.7. Cross-sections of the DOSXYZnrc imager model including 'supporting structures'.

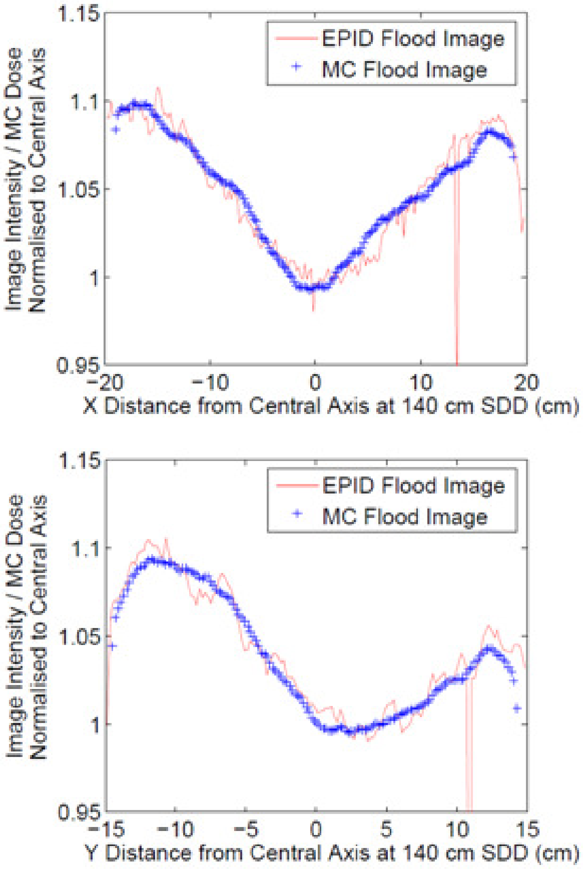

Figure 4.8. The matching of the MC simulated flood images to acquired flood images. The isolated low intensity values are due to defective imager pixels.

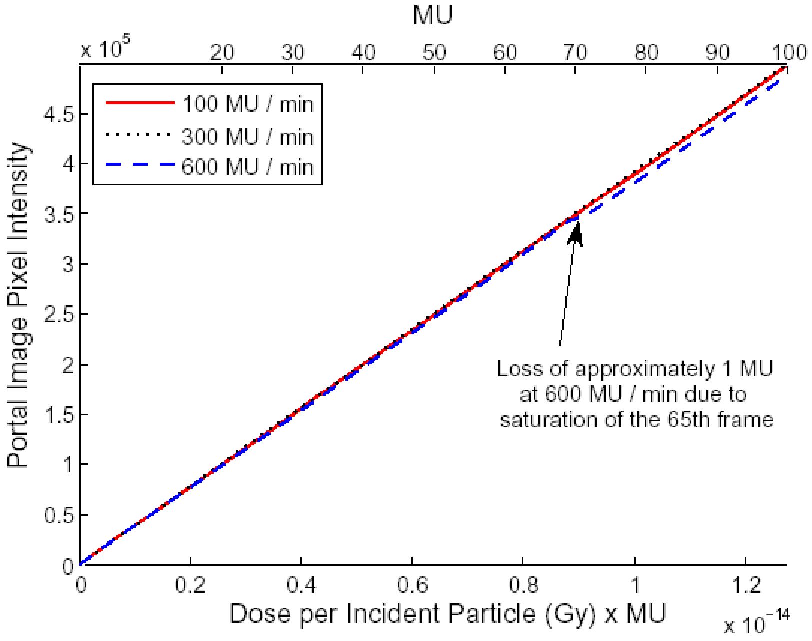

Figure 4.9. Portal Image Pixel Intensity versus MC dose and delivered MU for 100, 300 and 600 MU min^{-1} up to 100 MU.

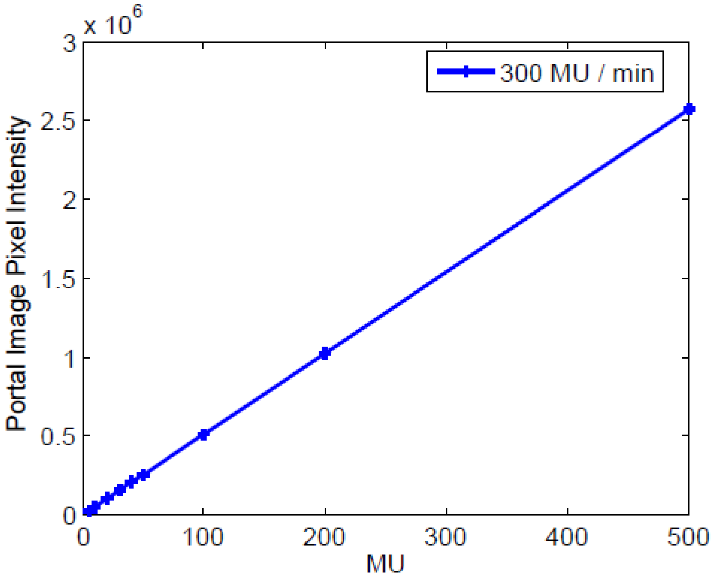

Figure 4.10. Linearity of EPID response for 300 MU min^{-1} for extended dose range from 5 MU to 500 MU.

The investigation into ghosting and image lag showed the effect to be similar at all 3 dose rates as depicted in figure 4.11. For the situation investigated, a 5MU (10 x 10) cm^2 image immediately following a 100 MU (5 x 5) cm^2 image, there was an increase in detector signal of the central pixels of 1.6% for all three dose-rates investigated. However, this increase corresponds to just 0.08 MU and as typical beam MU are much greater than 5MU, the percentage error would be very much less than 1.6% in practice.

The methods described in this chapter account for the effects of the differential backscatter for all field sizes both on and off-axis. It should be possible to extend this method to all EPID positional set-ups, although this has not been verified in this work. Measured versus simulated FSFs at the central axis are given in table 4.1. The approach correctly predicted electronic portal image greyscales for simple, non-IMRT fields to within ± 1% on the central axis. It can be seen from figure 4.12 A-D that for symmetric fields on the central axis there is very little difference in results with and without the devised solution for backscatter. However, for small off-axis fields there is very good agreement between MC and acquired image when taking the differential backscatter solution into account (within 1% for all fields), but a discrepancy of over 3% is visible for the small (2 × 2) cm^2 field off-set in the target direction when using 2 cm uniform backscatter in simulations.

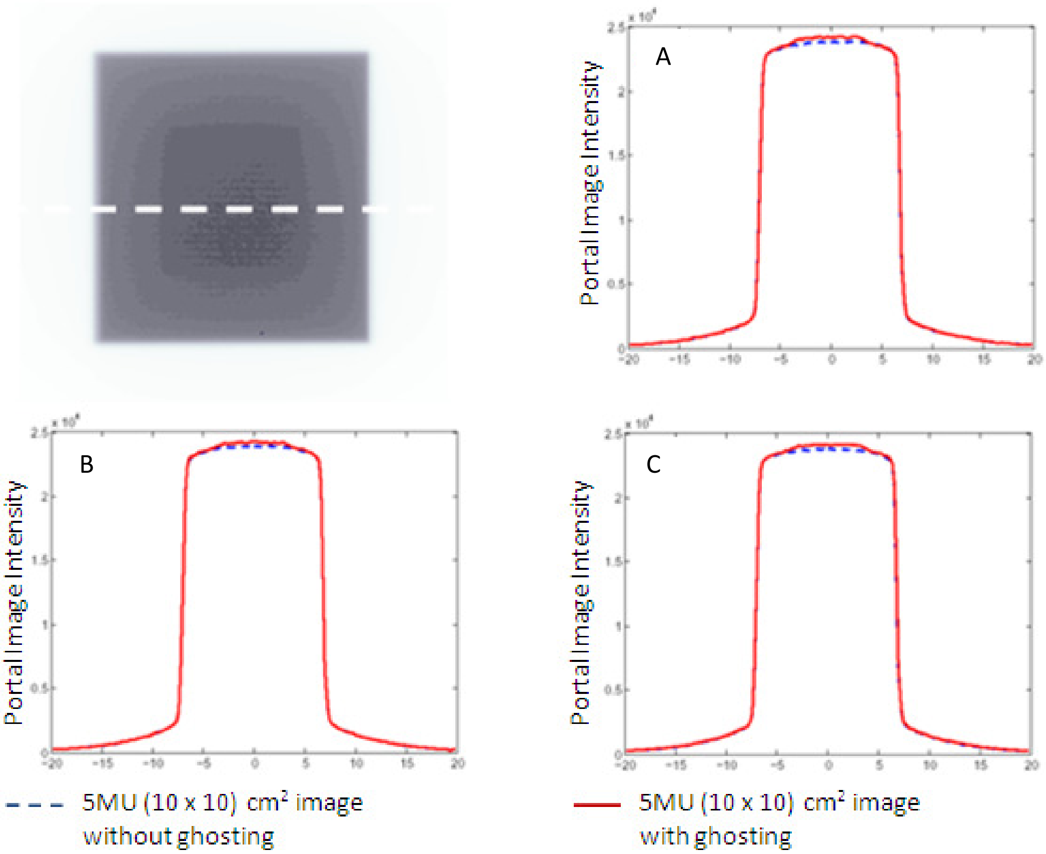

Figure 4.11 The effects of ghosting for a 5MU (10 x 10) cm^2 image immediately following a 100 MU (5 x 5) cm^2 image. A) 100 MU min^{-1} B) 300 MU min^{-1} and C) 600 MU min^{-1}.

Field Size (cm^2)	Measured EPID FSFs	1 cm uniform backscatter		2 cm uniform backscatter		Non-uniform backscatter solution	
		FSF	Percentage Difference	FSF	Percentage Difference	FSF	Percentage Difference
(2 × 2)	1.205	1.178	-2.2%	1.197	-0.7%	1.195	-0.8%
(5 × 5)	1.096	1.075	- 1.9%	1.087	- 0.7%	1.093	- 0.3%
(10 × 10)	1.000	1.000	-	1.000	-	1.000	-
(20 × 20)	0.914	0.928	+1.5%	0.923	+1.0%	0.923	+1.0%

Table 4.1. Measured EPID versus MC simulated FSFs for different backscatter conditions in simulations. Simulated FSFs were calculated for the central (5 × 5) voxels of (0.2 × 0.2) cm^2, uncertainties being less than 2% per voxel.

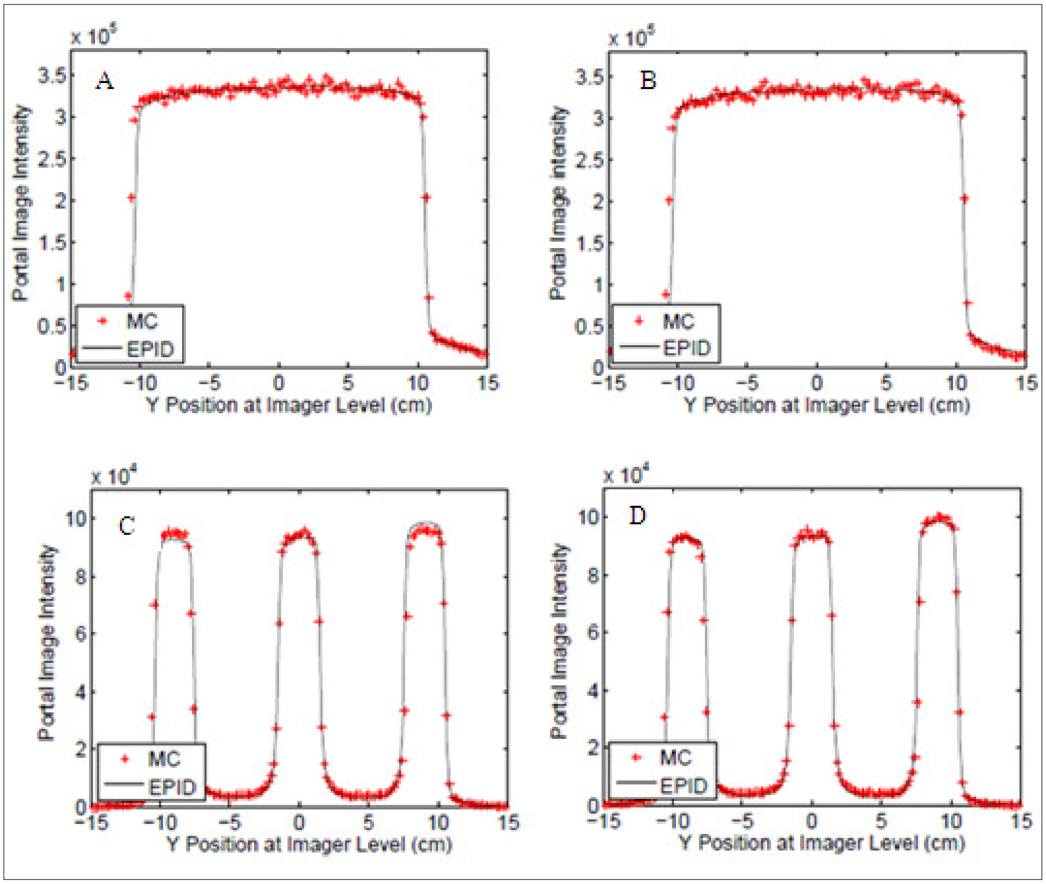

Figure 4.12. Inline profiles with and without the backscatter solution delivered in standard (non-IMRT) mode at a dose-rate of 300 MU min^{-1}. A) (15 × 15) cm^2 field with 2 cm uniform backscatter B) (15 × 15) cm^2 field with devised backscatter solution included C) 3 × (2 × 2) cm^2 fields with 2 cm uniform backscatter D) 3 × (2 × 2) cm^2 fields with devised backscatter solution included.

4.4 Discussion

The results obtained in this work are published in part by Cufflin *et al.* (2010a). The modelling solution devised to correct for non-uniform backscatter to the imager from the supporting structures is relatively simple yet has proved effective for all field sizes both on and off-axis, the results of MC IMRT simulations being presented in the next chapter. Additionally, EPID response was found to be linear with dose at in the range 5 to 500 MU at dose-rates of 100 and 300 MU min^{-1}. A loss of approximately 1 MU was observed due to saturation of the 65th frame at 600 MU min^{-1}, although a fix for this problem is reportedly available with an upgrade from the vendor. It is anticipated that the response would be linear at all dose-rates for upgraded systems.

Chapter 5

Pre-treatment Monte Carlo EPID Dosimetry for IMRT Verification

5.1 Introduction

This aspect of the thesis investigates the accuracy of MC simulations of amorphous silicon (a-Si) EPIDs for the dosimetric verification of IMRT prior to treatment. In particular, the suitability of the method for verification of head and neck IMRT with extended field segments (≈ 20 cm superior-inferior) covering almost the entire detector area was studied. This work also investigated the sensitivity of the technique to dose-rate variations in IMRT delivery.

5.2 Methods

5.2.1 Identification of IMRT Dose-Rate Dependent Delivery Errors

The imager was set-up to integrate the dose for the treatment beam (by selecting integrating or 'IMRT' image acquisition mode on the software). For clinical IMRT fields it is not possible to determine exact delivery errors that are present during each individual segment due to the complex nature in which multiple IMRT segments overlap and random errors being present on all segments (Ezzell and Chungbin 2001, Grigorov *et al.* 2006, Kuperman and Lam 2006). Therefore two simple sequences, one consisting of three sequential (2 × 2) cm^2 fields and the other of three sequential adjacent (5 × 5) cm^2 fields (figure 5.1) were created using Varian 'Shaper' software and delivered both in Varian standard mode (non-IMRT mode) and in IMRT mode at dose-rates of 100, 300 and 600 MU min^{-1}. The collimator was rotated to 90° and 10 MU per (2 × 2) cm^2 field or (5 × 5) cm^2 field was delivered. The EPID was irradiated directly and the same situation was set up within DOSXYZnrc for MC simulations. Portal images were acquired 3 times at each dose-rate and averaged. Calibration curves converting MC dose to portal image pixel intensity were obtained for a (10 x 10) cm^2 field and delivered MU of 10 to 100 MU. Additionally an NE 2571 Farmer-type ionisation chamber (Nuclear Enterprises, Berkshire, UK) was positioned at the centre of each (5 × 5) cm^2 segment, 5 cm deep in water equivalent material, as a direct comparison. An SDD of 140 cm was maintained to ensure a large enough field size for accurate chamber measurements. The measurements were repeated 10 times.

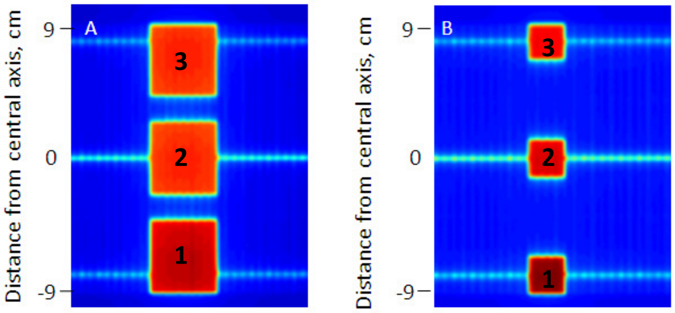

Figure 5.1. The simple three segment sequences set up to detect IMRT delivery errors. A) three (5 × 5) cm^2 segments and B) three (2 × 2) cm^2 segments.

5.2.2 Example Head and Neck IMRT Plan

The example IMRT plan referred to in this study is from a complex, highly modulated, head and neck 'step and shoot' treatment (figure 5.2) with 3 planning target volumes (PTVs) enabling the primary tumour and nodal volumes to be treated to different prescriptions of 66 and 54 Gy. The plan was optimised and calculated on Oncentra Masterplan (OMP, Nucletron) and consisted of 7 beams, all split in two due to restrictions in MLC movement, example EPID images being given in figure 5.3. It can be seen from figures 5.2 and 5.3 and table 5.1 that the treatment required very large fields (most with 20 cm superior-inferior extent) resulting in a large area of the detector being irradiated, meaning that an effective solution to the backscatter problem was imperative. The DICOM export facility was used to export the plan parameters, for example jaw and MLC positions and MU for each segment, and Matlab scripts used to automate creation of BEAMnrc input files.

5.2.2.1 Evaluation of Results

All results were processed using Matlab software and analysed using the gamma evaluation method (Low *et al.* 1998). The gamma evaluation method enables quantitative comparative analysis of dose distributions. Now in widespread use for comparing dose distributions in radiotherapy, the original technique was proposed in 1998. The method takes into account both percentage dose difference and distance to agreement (DTA) (equation 5.1), both these quantities being given levels by which to pass or fail a dose point when two dose distributions are compared.

$$\Gamma = \sqrt{\frac{r^2(\vec{r}_m, \vec{r}_c)}{\Delta d_m^2} + \frac{\partial^2(\vec{r}_m, \vec{r}_c)}{\Delta D_m^2}} \qquad (5.1)$$

where for each reference point, $\vec{r}_m$, gamma, Γ, is evaluated with respect to the calculation point, $\vec{r}_c$. Δd_m is the defined 'acceptable' distance to agreement and ΔD_m the defined 'acceptable' dose difference. Finally, $r(\vec{r}_m, \vec{r}_c)$ is the distance $\vec{r}_c - \vec{r}_m$ and $\partial^2(\vec{r}_m, \vec{r}_c)$ is the dose difference between the dose at the calculation point and the dose at the reference point. If the gamma evaluation value for a reference point is less than one, then that point has 'passed' the evaluation. Usually a percentage of points passing or failing is quoted.

Gamma analysis was performed for a 20% dose threshold so that the results were representative of the area within the treatment field. The percentage of points within the field passing gamma criteria of 2% (of maximum dose), 2.8 mm were calculated at the detector level of 140 cm SDD and converted back to isocentre level.

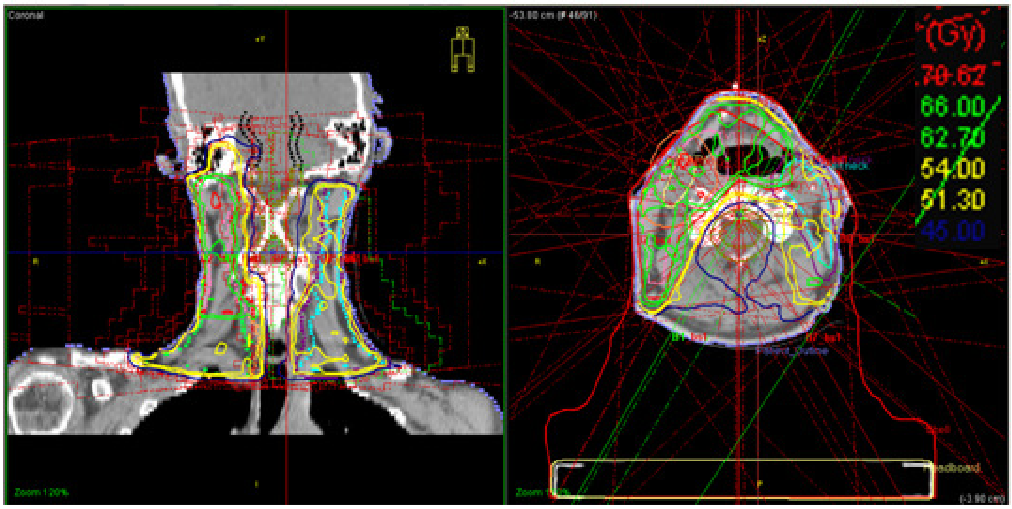

Figure 5.2. The complex IMRT plan modelled in this chapter**.** There are 2 dose levels prescribed, the primary PTV being treated to 66 Gy and additional nodal PTVs being treated to 54 Gy.

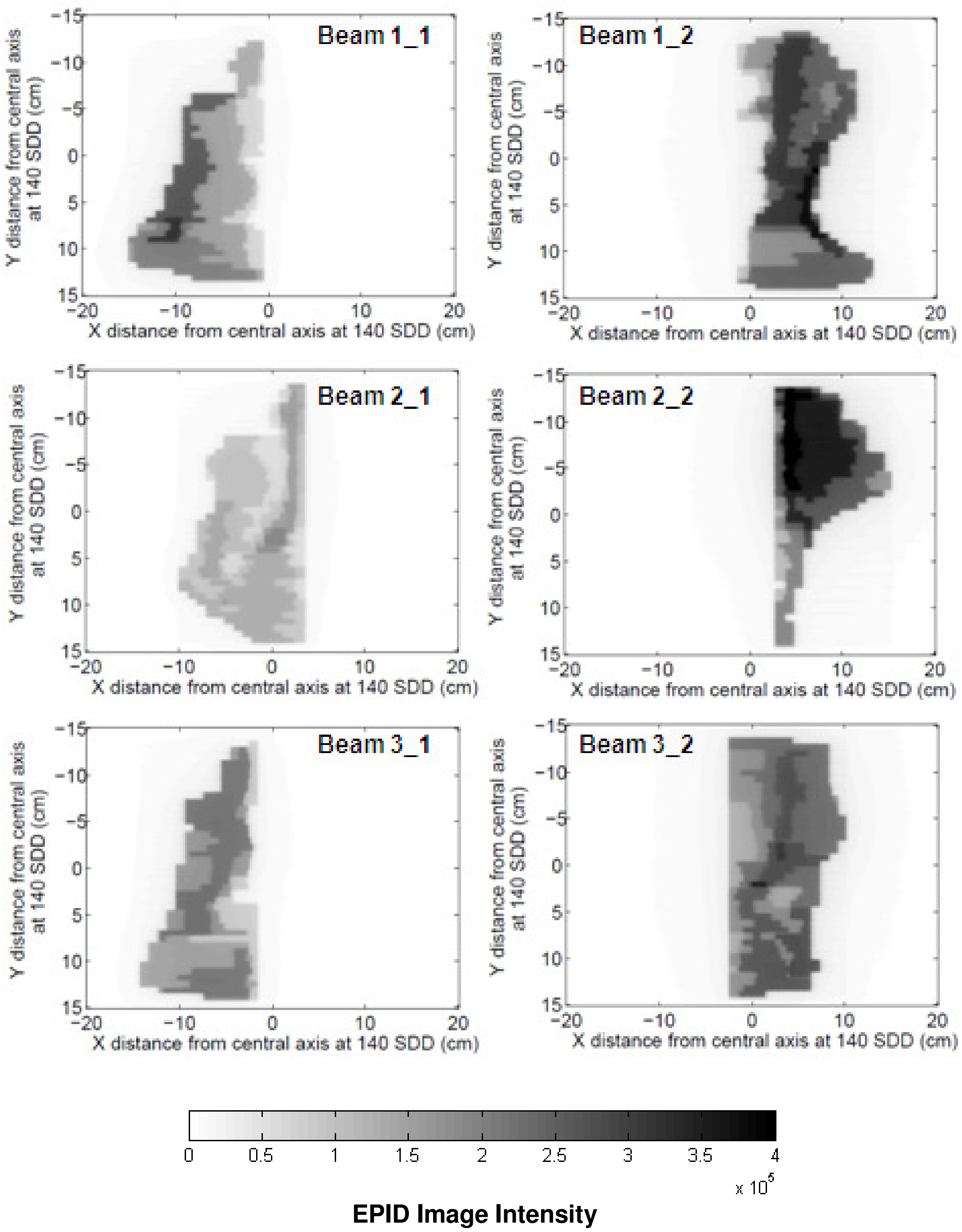

Figure 5.3 EPID images (at 140 cm SDD) for beams 1 to 3.

Beam	X (crossline) dimension (cm)	Y (inline) dimension (cm)	Number of Segments	Total Beam MU
1_1	10.5	18.5	4	60
1_2	10.5	20.0	6	93
2_1	9.8	20.0	7	71
2_2	9.1	20.0	5	40
3_1	9.1	20.0	4	40
3_2	9.1	20.0	6	66
4_1	11.2	20.0	6	64
4_2	10.5	20.0	6	73
5_1	10.5	20.0	8	69
5_2	10.5	19.5	4	23
6_1	8.4	19.5	6	59
6_2	8.4	19.5	6	50
7_1	10.5	19.5	6	71
7_2	9.8	19.5	6	68

Table 5.1. IMRT Plan Information.

5.3 Results

5.3.1 Identification of IMRT Delivery Errors

Figure 5.4 A - D shows the comparison between MC simulation and acquired image when delivering the (2 × 2) cm^2 sequence in figure 5.1 in both standard (non-IMRT) and IMRT mode at a dose-rate of 300 MU min^{-1}. C and D demonstrate the ability of the MC EPID dosimetry technique to detect the systematic overdose on the first segment and systematic underdose on the final segment for IMRT deliveries, these errors being of the order of 0.3 MU at 300 MU min^{-1}. These delivery errors increase with dose-rate and are not present for standard, non-IMRT deliveries. The delivery errors were found to be very similar for both sets of sequences illustrated in figure 5.1, the (2 × 2) cm^2 sequence being shown in figure

5.4 to demonstrate the combination of dose-rate plus backscatter effects, the backscatter effects being greater the smaller the field size. These results were verified by ion chamber measurements, agreement between EPID images and chamber measurement being within 0.1 MU (or 1%) for the 10 MU per segment deliveries (1% being the uncertainty on these simulations). Average undershoot and overshoot delivery errors measured by ion chamber were of approximately 0.1 MU, 0.3 MU and 0.6 MU at 100, 300 and 600 MU min^{-1} respectively. Additionally, random delivery errors, also increasing with increasing dose-rate, were measured on intermediate segments.

The delivery errors observed are understood to be due to the finite sampling time of the MLC controller. This effect has been observed previously using other methods (Ezzell and Chungbin 2001, Grigorov *et al.* 2006, Kuperman and Lam 2006). Irradiation of all segments is initiated by the MLC controller when the leaves are within tolerance (1 mm), but the MLC controller only receives information on delivered MU approximately every 50 ms, resulting in the delivered MU being different to the planned MU. The total beam cumulative MUs are, as for standard deliveries, monitored and controlled by the monitor ionisation chambers and so if too many MU have been delivered at the start of the final segment, this will result in an underdose on this segment.

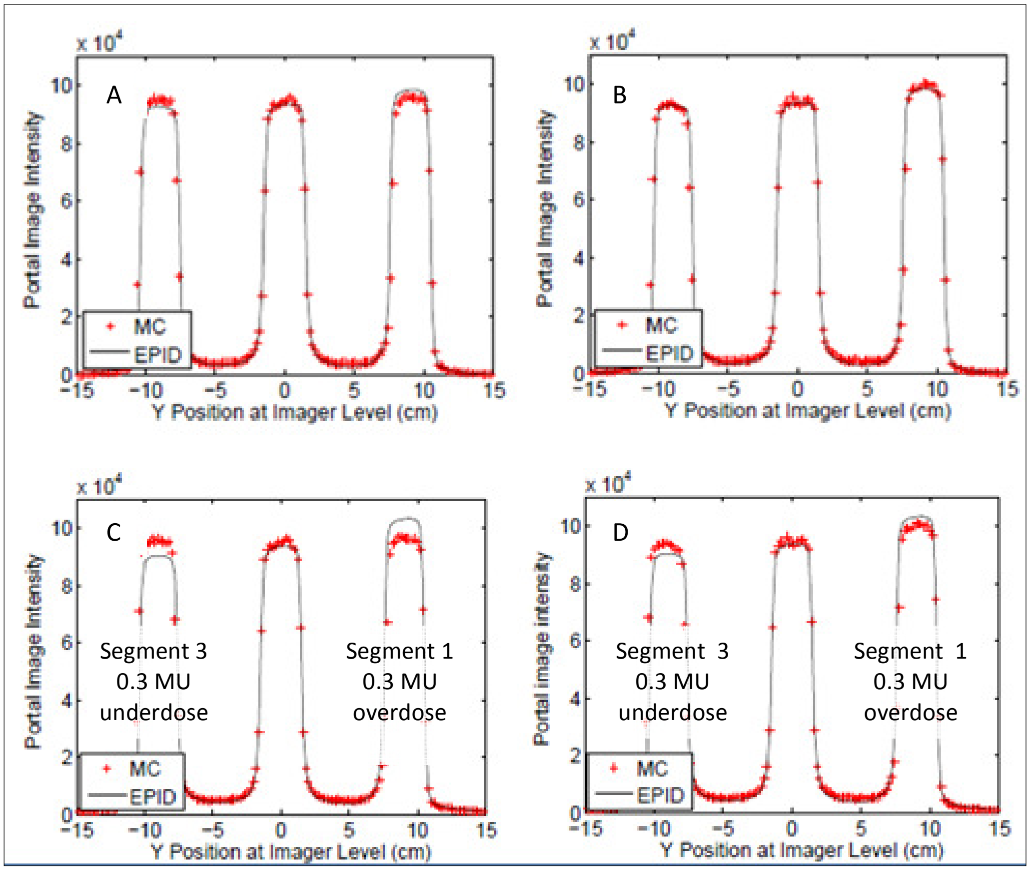

Figure 5.4. Inline profiles with and without the backscatter solution delivered in both standard (non-IMRT) and IMRT mode at a dose-rate of 300 MU min^{-1}. A) 3 × (2 × 2) cm^2 standard delivery fields with 2 cm uniform backscatter B) 3 × (2 × 2) cm^2 standard delivery fields with devised backscatter solution included C) 3 × (2 × 2) cm^2 IMRT delivery fields with 2 cm uniform backscatter D) 3 × (2 × 2) cm^2 IMRT delivery fields with devised backscatter solution included. C and D demonstrate the ability of the technique to detect overshoot and undershoot delivery errors on the first and last segments respectively.

	Segment 1	**Segment 2**	**Segment 3**
100 MU min^{-1}	+0.11 MU (σ 0.02 MU)	-0.01 MU (σ 0.01 MU)	-0.10 MU (σ 0.01 MU)
300 MU min^{-1}	+0.33 MU (σ 0.06 MU)	+0.11 MU (σ 0.05 MU)	-0.30 MU (σ 0.06 MU)
600 MU min^{-1}	+0.67 MU (σ 0.09 MU)	+0.15 MU (σ 0.19 MU)	-0.59 MU (σ 0.08 MU)

Table 5.2. Average IMRT dose delivery errors with associated standard deviation, σ, measured with ionisation chamber.

5.3.2 Example Head and Neck IMRT Plan

For the head and neck IMRT plan an average of 96% of points passed gamma criteria of 2%, 2 mm (at isocentre) at a dose-rate of 100 MU min^{-1} with the backscatter solution included, compared to an average of 79% of points passing this gamma criteria without the correction included (see detailed results in table 5.3). Figure 5.5 shows the improvement in image intensity prediction for a beam with a small off-axis segment (beam 3_1) when the backscatter effect is included.

		2%, 2.8 mm at 140 cm SDD		**3%, 4.2 mm at 140 cm SDD**	
Beam	**Total MU**	**With backscatter correction**	**Without backscatter correction**	**With backscatter correction**	**Without backscatter correction**
1_1	60	94.9	81.9	99.6	99.3
1_2	93	96.2	78.0	99.9	98.0
2_1	71	97.6	75.5	99.9	96.2
2_2	40	95.5	91.8	100.0	99.6
3_1	40	95.2	80.5	99.5	91.1
3_2	66	96.2	65.8	99.6	91.2
4_1	64	98.1	79.2	100.0	98.6
4_2	73	94.4	68.3	99.6	91.6
5_1	69	96.4	84.1	99.9	99.4
5_2	23	88.4	80.7	98.5	97.9
6_1	59	96.7	90.0	99.9	99.7
6_2	50	97.9	78.5	99.7	98.5
7_1	71	96.5	71.7	99.5	96.6
7_2	68	96.4	73.9	99.7	97.5
Average		**95.7**	**78.6**	**99.7**	**96.8**
σ		**2.5**	**7.4**	**0.4**	**3.2**

Table 5.3 Percentage of points passing gamma criteria of 2%, 2.8 mm and 3%, 4.2 mm with and without the devised correction for non-uniform backscatter. The standard deviation, σ, is also given. All images were acquired at 100 MU min^{-1}, the most accurate delivery.

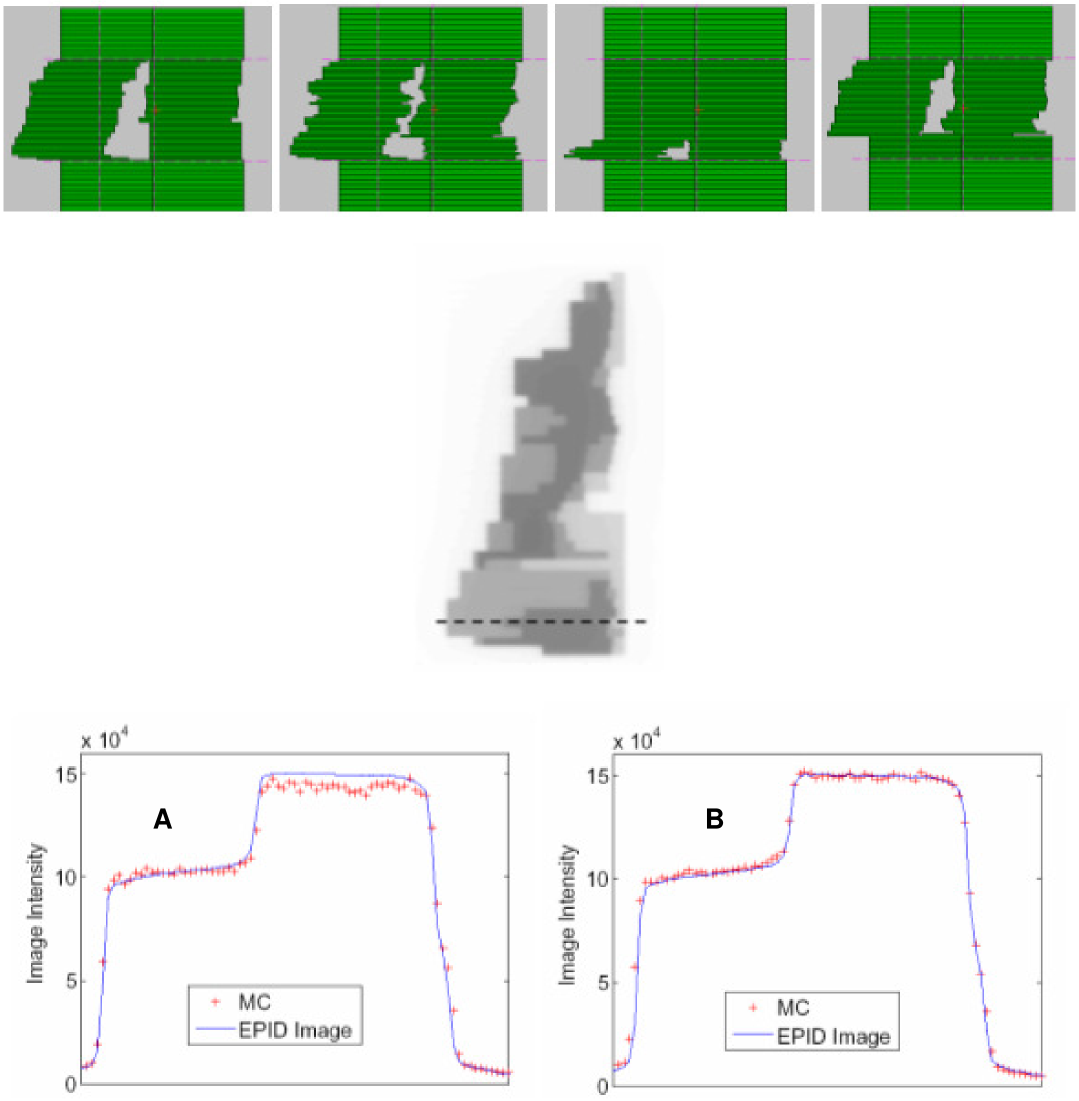

Figure 5.5. Demonstrating the effect of the established correction for backscatter for beams with small off- axis segments (beam 3_1 is shown in the figure). A) Without backscatter correction included. B) With backscatter correction included.

Irradiating all IMRT fields at dose-rates of 100 and 300 MU min^{-1} clearly demonstrated the ability of the technique to detect dose delivery errors. For all images, there is much better agreement between acquired image and prediction at 100 MU min^{-1} than at 300 MU min^{-1}, an average of 96% and 92% of points pass gamma criteria of 2%, 2 mm (at isocentre) at a dose-rate of 100 and 300 MU min^{-1} respectively (see summary in table 5.4). In addition, the areas exposed to both the first and final segments consistently showed low dose differences due to the overshoot and undershoot effects cancelling out, average dose differences for these areas all being within 1.5% local dose for the 100 MU min^{-1} acquisitions and 2.5% local dose for the 300 MU min^{-1} acquisitions. In all cases the first segment covered a much greater area than the final segment and areas of overdose can be seen within areas exposed during the first segment but not the final segment. Figure 5.6 shows the percentage difference between acquired image and MC prediction for beam1_1, as an example of the results obtained. It can be seen that the difference between MC prediction and measurement is low for the area of overlap between the first and last segments.

600 MU min^{-1} deliveries showed greater discrepancies but detailed results have not been included due to the saturation of the 65th frame being unpredictable for IMRT deliveries. For all situations the lowest percentage of points passing the gamma criteria was for beam 5_2, this beam consisting of only 23 MU in total (4 segments of 5.1, 4.3, 1.3 and 12.3 MU) and so sub-MU dose delivery errors are a large percentage of each segment MU.

		2%, 2.8 mm at 140 cm SDD		**3%, 4.2 mm at 140 cm SDD**	
Beam	**Total MU**	**100 MU min^{-1}**	**300 MU min^{-1}**	**100 MU min^{-1}**	**300 MU min^{-1}**
1_1	60	94.9	92.2	99.6	99.5
1_2	93	96.2	94.5	99.9	99.9
2_1	71	97.6	89.3	99.9	99.7
2_2	40	95.5	96.1	100.0	99.9
3_1	40	95.2	93.1	99.5	99.4
3_2	66	96.2	95.5	99.6	99.6
4_1	64	98.1	97.8	100.0	100.0
4_2	73	94.4	84.1	99.6	98.9
5_1	69	96.4	96.1	99.9	99.7
5_2	23	88.4	80.5	98.5	95.9
6_1	59	96.7	90.6	99.9	99.8
6_2	50	97.9	89.1	99.7	98.5
7_1	71	96.5	94.3	99.5	99.6
7_2	68	96.4	92.7	99.7	99.6
Average		95.7	91.9	99.7	99.3
σ		2.4	4.8	0.4	1.1

Table 5.4 Percentage of points passing gamma criteria of 2%, 2.8 mm and 3%, 4.2 mm at 100 and 300 MU min^{-1}. The standard deviation, σ, is also given.

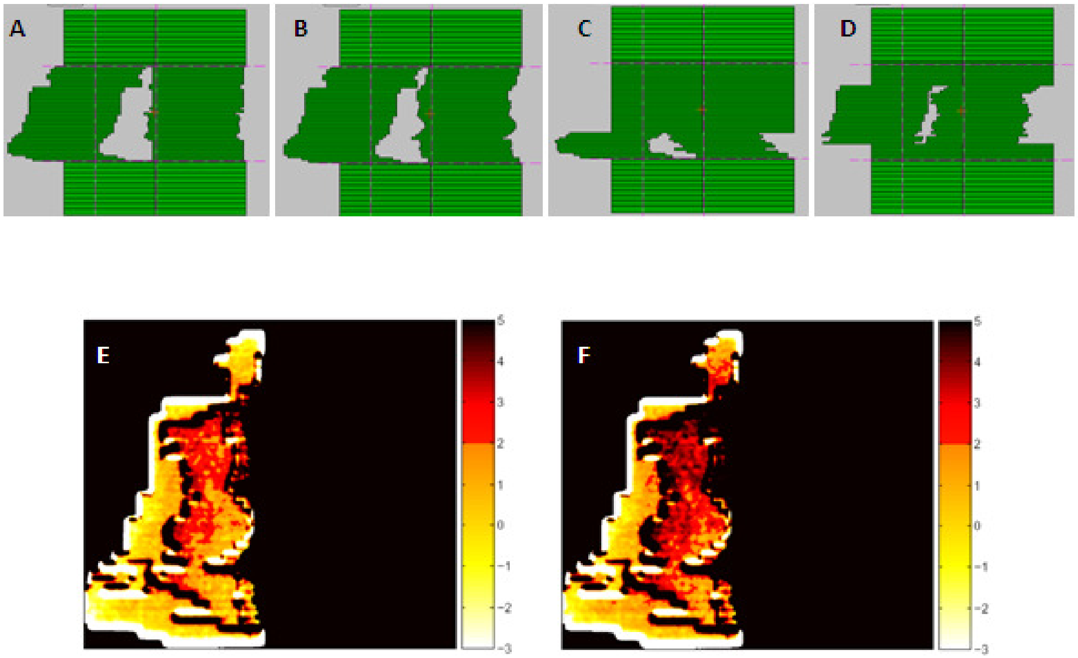

Figure 5.6. Beam 1_1 (60 MU, 4 segments). A-D) The beam segments in order, E) Percentage difference between acquired image and MC prediction at 100 MU min^{-1}, F) Percentage difference between acquired image and MC prediction at 300 MU min^{-1}.
NB The area outside the beam has been excluded from the calculation and therefore should not be interpreted according to the colour scale.

5.4 Discussion and Conclusions

The results obtained in this work were reported in Cufflin *et al.* (2010a) and presented, in part, at the international Electronic Portal Imaging conference in San Francisco in 2008, EPI2k8 (Cufflin *et al.* 2008). They show Monte Carlo portal dosimetry to be a particularly accurate IMRT verification technique. The modelling solution devised to correct for non-uniform backscatter to the imager from the supporting structures enables the verification of large IMRT beams covering almost the entire detector area. The IMRT verification results using MC portal dosimetry are excellent, with an average of 96% of pixels passing gamma criteria of 2%, 2 mm at isocentre at 100 MU min^{-1} with the devised correction for backscatter included.

Additionally this investigation has shown MC to be accurate enough to detect real, sub-MU delivery errors, the magnitude of these errors being consistent with previously published data derived by other methods (Ezzell and Chungbin 2001, Grigorov *et al.* 2006, Kuperman and Lam 2006). Additional random errors on any overlapping intermediate segments may increase the magnitude of the overall error per beam. Although these sub-MU errors are unlikely to be significant individually, delivery errors on multiple beams incident on the same volume of tissue will have a cumulative effect. These errors may be a significant percentage of low dose regions within IMRT treatment fields, which often correspond to organs at risk such as the spinal cord or rectum. Grigorov *et al.* 2006 show an example where approximately 30% of the rectal volume received an increase in dose due to the overshoot effect. They reported an average increase in rectum mean dose of 0.5 Gy and 2-3% NTCP for the 'overshoot' dose inaccuracy. Similarly, if multiple last segments are incident on the same voxels, a cold spot in the PTV may result. Along with the demonstrated pre-treatment solution to the verification of IMRT, chapter 8 describes the development and application of the technique to the verification of delivery during treatment (transit dosimetry) without intrinsic reduction in accuracy.

Initially the main drawback of this technique was that it was time consuming, single segments taking several hours to simulate on the cluster of 30 processors described above. However, distributing simulations on the recently developed RTGRID service (Chapter2, Downes *et al.* 2009) enables more rapid (and therefore more routinely usable) calculations.

This work demonstrates the sensitivity and accuracy of MC portal dosimetry for absolute verification purposes and fields of arbitrary complexity. The technique will enable testing of methodologies put in place to correct for delivery errors, such as those described by Grigorov *et al.* (2006) and Kuperman and Lam (2006) and can also aid in the selection of the best delivery parameters for IMRT treatments.

Chapter 6

INtegrated TReatment Planning and EPID Dosimetry (INTREPID): Devised Method and Novel Correction for Non-Uniform Backscatter

6.1 Introduction

Although it is widely accepted that MC simulations provide the most accurate method of radiotherapy dose calculation, they are inevitably time consuming. Even with increased computing power this issue continues to restrict the widespread use of MC simulations clinically. For this reason this work has investigated an alternative method for clinical verification of IMRT plans using an

EPID. The method devised as a part of this work is accurate, efficient and cost effective. Doses delivered by the IMRT plan for a given patient are calculated in a water-equivalent phantom at the EPID position of 140 cm SDD on the TPS currently used for all clinical radiotherapy planning. The dose 'maps' are converted to EPID image intensity using a set of pre-calculated correction factors provided from MC simulations and measurement. The technique has the advantage that it utilises the TPS and algorithm that the patient plan was based upon. The developed MC pre-treatment method (chapter 5) verifies the treatment delivery only, separate MC simulations in water or using patient CT data being needed to verify the TPS dose calculation.

Additionally, the difficulties in dosimetry caused by non-uniform backscatter from the imager arm (the effects of which are discussed in detail in chapter 4) had to be approached differently. A novel and versatile solution was found, which can be applied to all EPID dosimetry systems regardless of dose calculation methods used.

6.2 Method

As with all EPID work described in this thesis, calculations and measurements were carried out on a Varian 2100 CD linear accelerator with aS500 EPID at 140 cm SDD. IMRT irradiations were carried out at a dose-rate of 300 MU min^{-1}. As previously discussed in Chapter 5, there are known systematic delivery errors averaging 0.3 MUs for the first and last segment at this dose-rate but a lower dose-rate is not clinically practical with the need for high patient throughput to help keep patient waiting lists under control.

All IMRT dose distributions were planned and optimised on Oncentra Masterplan (OMP, Nucletron). These clinical plans were exported in DICOM format and then re-imported onto a water phantom set up in OMP. The dose distributions were calculated at the depth of dose maximum (d_{max}), this layer being set at the position of the scintillating screen. Calculation grid resolution was set to $0.1 \times 0.1 \times 0.1$ cm^3.

The process requires conversion of dose in water to EPID image intensity, the methodology followed being similar to that of the GLAaS algorithm (General Linear "calibration" Algorithm for the Varian a-Si PortalVision aS500) presented by Nicolini *et al.* (2006). Every IMRT segment is considered as having two components; the primary beam and the portion transmitted through the MLC. MC simulations were used to compare dose in water (at d_{max}) with EPID image intensity both within the field (for a 10×10 cm^2 field) and beneath the MLC, enabling dose conversion factors to be obtained.

It can be seen from figure 6.1 that there is a significant difference between water and EPID field size dependent output factors and so a single conversion factor converting from dose in water to EPID image intensity is not sufficient. Therefore, the equivalent window width field (EWWF), as defined by the MLCs, is calculated for every IMRT segment and a field-size dependant output factor, based on measurement, was applied to account for the difference between water and EPID field-size output factors. The EWWF is a similar concept to the 'equivalent square' commonly used in radiotherapy dose calculations for rectangular fields.

$$\text{Equivalent square} = 2xy/(x+y) \qquad (6.1)$$

where x is the field width and y the length. In the EWWF, x is defined as the mean leaf aperture for all MLC leaves.

The standard Varian EPID calibration procedure, which involves dividing every image by a 'flood' image was employed, resulting in flat images (as described in Chapter 4). Therefore all OMP dose distributions were similarly divided by an OMP calculated 'flood' field of the same dimensions as the EPID flood field.

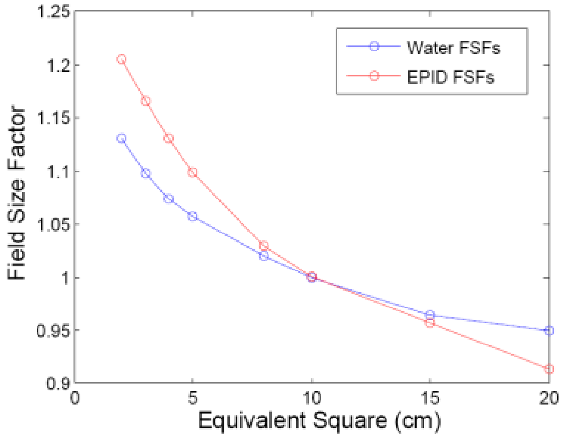

Figure 6.1. EPID and water field size output factors (FSFs), normalised to a (10 × 10) cm^2 field.

Acquired images are compared with image predictions, gamma analysis being carried out for a 20% dose threshold. If greater than 10% of points fail gamma criteria of 3% maximum dose, 3 mm DTA further investigations are carried out. The process map of the technique is given in figure 6.2.

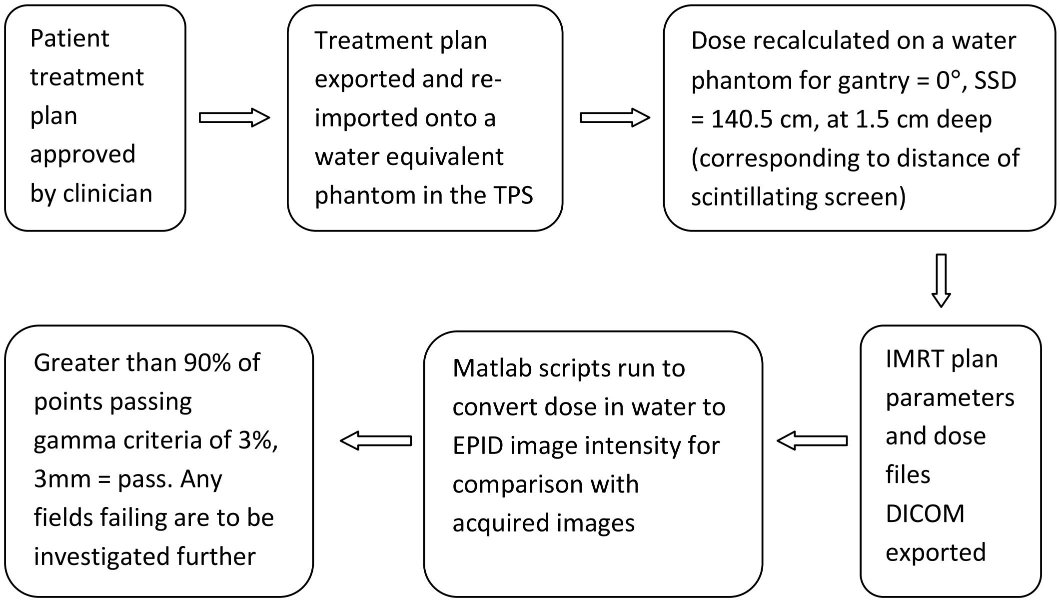

Figure 6.2. Process map for INTREPID pre-treatment portal dosimetry.

6.2.1 Correction for Non-Uniform Backscatter

As discussed in previous chapters, one of the biggest challenges facing those implementing portal dosimetry on Varian linacs is the non-uniform backscatter from components in the inline direction. When using the standard flood field calibration, the consequences are worst for small, off-axis fields, for which the scatter conditions deviate most from the flood field calibration conditions (Chapter 4, Cufflin *et al.* 2010a). Additionally, off-axis response in EPID differs from that in water due to different detection sensitivities to varying beam qualities off-axis, a consequence of the cone-shaped, high density, flattening filter within the linac (Parent *et al.* 2006). The method described here to correct for non-uniform backscatter also incorporates correction for any discrepancies in the results due to the differing response to the off-axis beam softening.

The first step was to investigate the magnitude of the non-uniform backscatter effect and how it varied with detector position. The imager was irradiated with a sequence of small square fields with matched edges covering as much of the detector area as possible without irradiation of the read-out electronics. To this end, (3 x 3) cm^2, (4 x 4) cm^2, (5 x 5) cm^2, (6 x 6) cm^2, (8 x 8) cm^2, (10 x 10) cm^2 and (15 x 15) cm^2 fields were explored. Corresponding fields were set up on the TPS, divided by the TPS 'flood field', and the ratio of the central point of each EPID measured field to TPS field was calculated. These results were used to form a series of matrices, which were interpolated and smoothed within Matlab enabling a field size and position dependent correction to be applied to every IMRT segment. Using the TPS calculated doses for this correction was justified as the TPS has previously been extensively commissioned for off-axis fields, very good agreement between TPS and measurement being obtained within the central ± 10 cm in both directions. It is very unlikely that an IMRT field would extend significantly beyond this range. Alternatively, measurement or MC simulation could be used instead of TPS calculated doses for these off-axis fields, but still applying the principles of this method.

Initially, as a part of this work the ‘gravitational centre’ of every IMRT segment was located and the non-uniform backscatter correction applied to each segment was based on this position only. However, IMRT segments are far more complex than simple square fields. For example, for segment 2 in figure 6.3, a gravitational centre of x = -4.6 cm, y = -2.6 cm and an EWWF of 6.2 cm were calculated. This would result in a correction factor of 1.008 being applied to the segment, which is not representative of the correction required for the lower part of the segment (in the target direction). Appling a matrix of correction factors for this segment results in a factor of 1.005 being applied to the upper half of the segment, but a correction as great as 1.025 is applied to the lowest part of the segment, which is a much closer representation of the differential backscatter in reality. The best solution for complex segments, however, is to explicitly model the backscattering materials using MC methods as described in Chapter 4.

A detailed description of the processes contained within the automated Matlab script is given in figure 6.4.

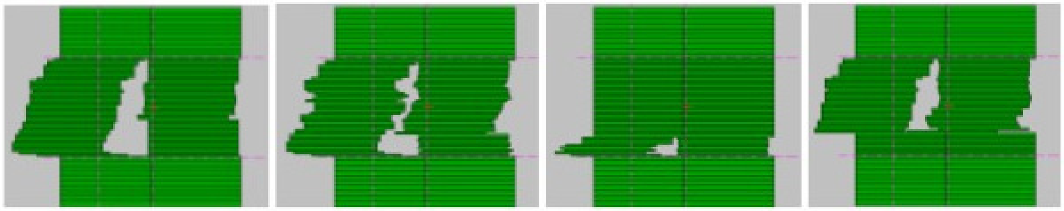

Figure 6.3. 4 segments of an IMRT beam demonstrating the complexity of segment shapes . This corresponds to beam 5 of patient 6 in table 6.1.

6.3 Results

For the first 10 IMRT treatment plans evaluated (a total of 82 beams from head and neck or pelvic plans), an average of 96% of points within the treatment field passed gamma criteria of 3% maximum dose, 3 mm DTA without the correction for backscatter included. Although in general these results are satisfactory, it can be seen from table 6.1 that a handful of beams produced poor results, with fewer than 90% of points passing gamma criteria of 3%, 3 mm. These beams all have at least one small segment off-axis in the inline direction. However, for fields with larger or more symmetric segments, satisfactory results are obtained without the correction for backscatter included.

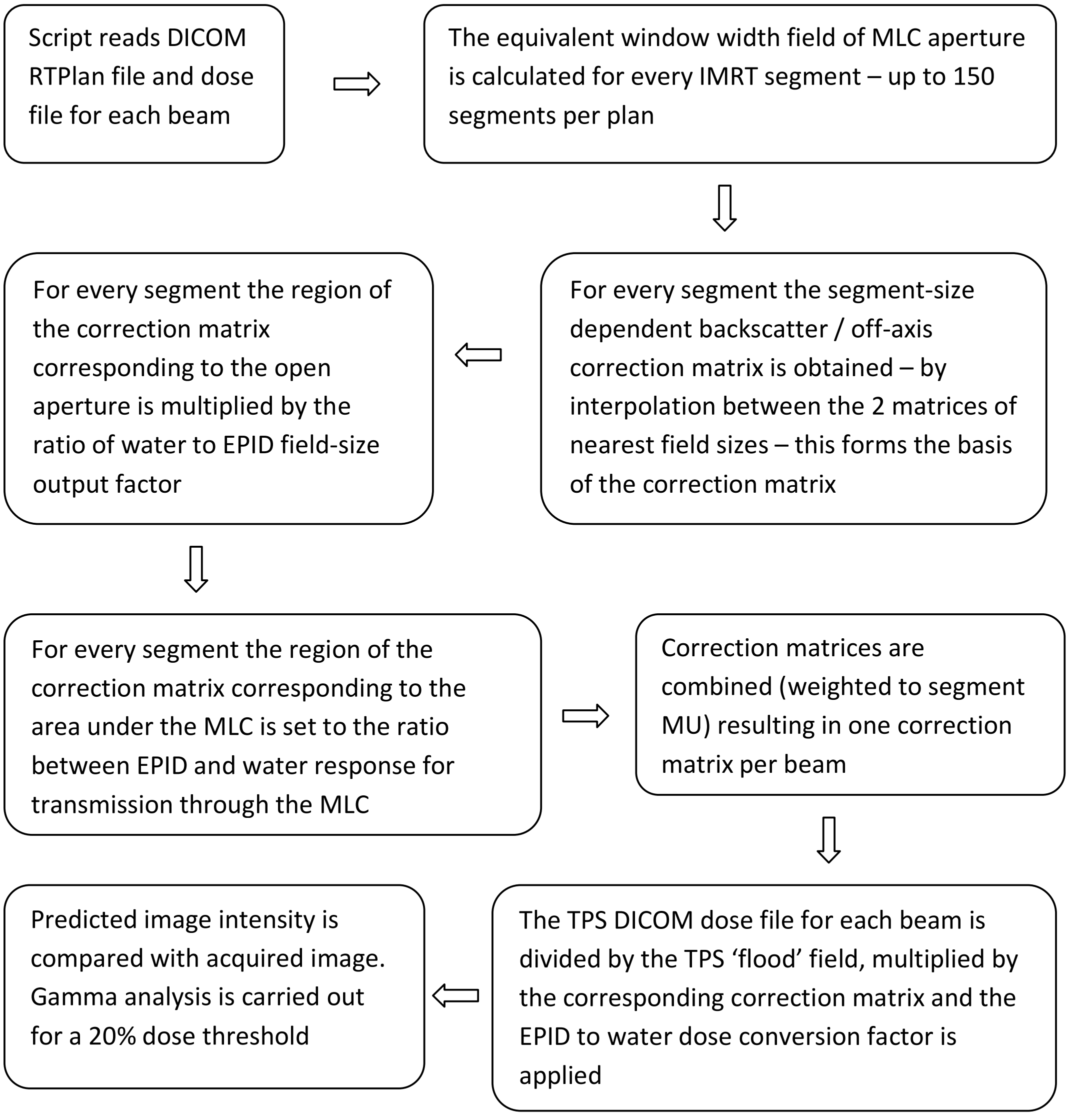

Script reads DICOM RTPlan file and dose file for each beam

The equivalent window width field of MLC aperture is calculated for every IMRT segment – up to 150 segments per plan

For every segment the segment-size dependent backscatter / off-axis correction matrix is obtained – by interpolation between the 2 matrices of nearest field sizes – this forms the basis of the correction matrix

For every segment the region of the correction matrix corresponding to the open aperture is multiplied by the ratio of water to EPID field-size output factor

For every segment the region of the correction matrix corresponding to the area under the MLC is set to the ratio between EPID and water response for transmission through the MLC

Correction matrices are combined (weighted to segment MU) resulting in one correction matrix per beam

The TPS DICOM dose file for each beam is divided by the TPS ‘flood’ field, multiplied by the corresponding correction matrix and the EPID to water dose conversion factor is applied

Predicted image intensity is compared with acquired image. Gamma analysis is carried out for a 20% dose threshold

Figure 6.4 Description of automated Matlab script processes.

Patient	**1**	**2**	**3**	**4**	**5**	**6**	**7**	**8**	**9**	**10**	**Overall**
Beam											
1	98.90	97.88	99.20	99.20	94.20	91.60	97.50	98.00	90.80	98.00	
2	98.60	97.98	98.80	98.10	96.40	98.40	98.70	97.90	98.00	98.20	
3	98.30	97.78	97.90	97.50	97.40	94.50	97.40	96.80	95.50	98.10	
4	99.00	98.55	98.70	98.40	98.10	94.30	98.10	99.00	96.80	**86.60**	
5	97.80	97.60	96.40	98.40	97.80	**86.00**	98.10	98.90	97.40	98.30	
6	99.50	97.33		93.30	99.20	**88.40**	98.20	94.50		98.30	
7	97.10	91.07		92.60	**83.50**	98.30	96.60	97.90		98.50	
8					98.10	92.00		90.60		93.40	
9					96.70	98.60		98.60		96.70	
10					94.90	95.70		90.80			
11					97.10	98.40					
12						98.80					
13						99.10					
14						**89.40**					
Average	**98.46**	**96.88**	**98.20**	**96.79**	**95.76**	**94.54**	**97.80**	**96.30**	**95.70**	**96.23**	**96.40**
σ	**0.81**	**2.59**	**1.11**	**2.68**	**4.32**	**4.41**	**0.69**	**3.22**	**2.89**	**3.96**	**3.34**

Table 6.1. Gamma pass results for 3%, 3 mm without correcting for differential backscatter. σ denotes the standard deviation.

Figure 6.5 shows the gamma map and the local dose percentage difference for beams 5 and 6 of patient 6, without the correction for non-uniform backscatter included. It can be seen that both of the beams have small off-axis segments, which coincided with a poor gamma pass rate.

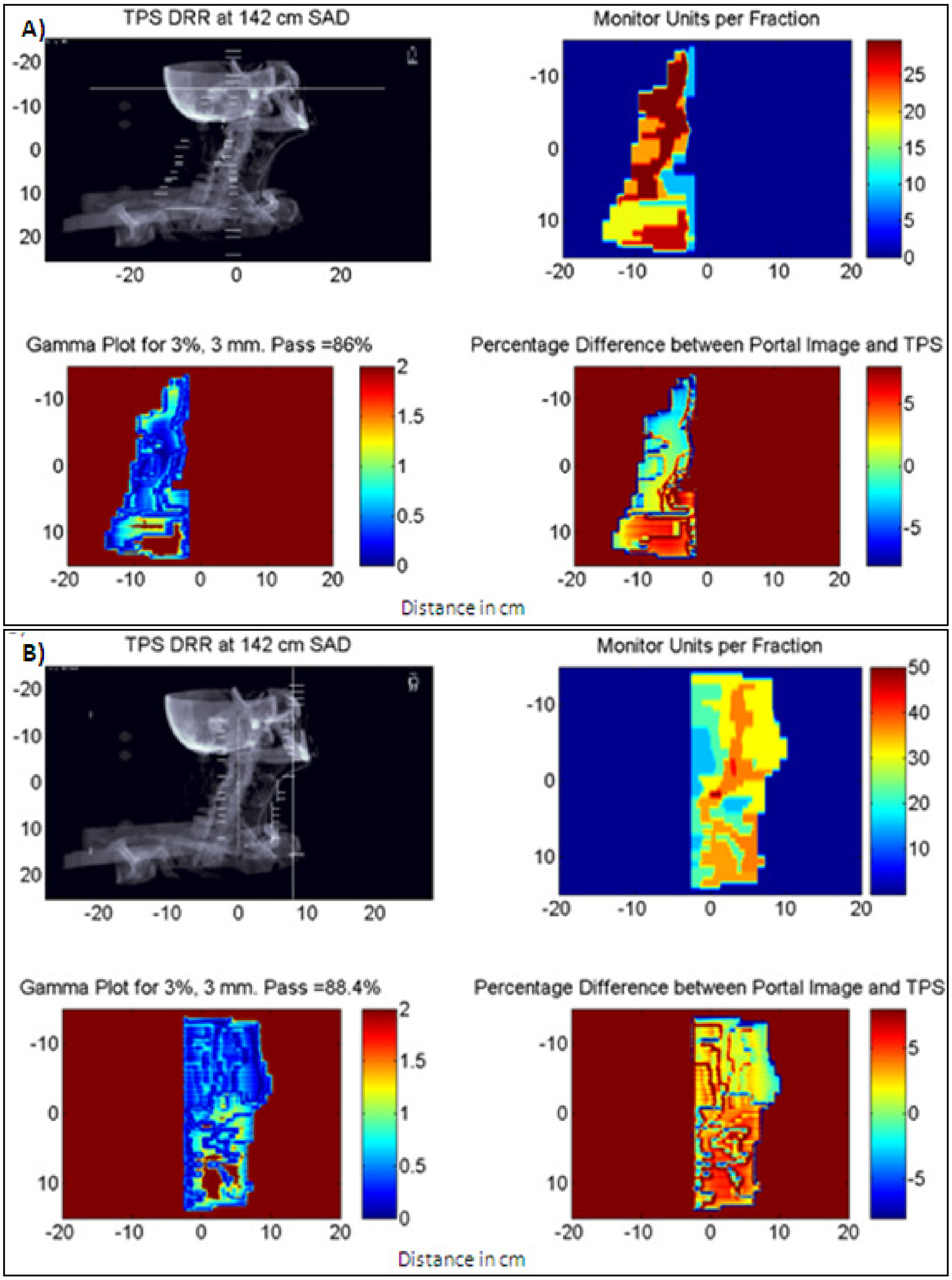

Figure 6.5. Results without non-uniform backscatter correction for A) Patient 6, beam 5 and B) Patient 6, beam 6. The TPS digitally reconstructed radiographs (DRRs) at the imager source to axis distance (SAD) are also shown. NB The area outside the beam has been excluded from all calculations and therefore should not be interpreted according to the colour scale.

6.3.1. Results: Correction for Non-Uniform Backscatter

Figure 6.6 shows the correction matrices obtained for (3 × 3) cm^2, (4 × 4) cm^2 and (6 × 6) cm^2 fields. As expected, the correction increased with decreasing field size and distance from the central axis in the target direction. A maximum correction of 1.07 was applied at the corners of the imager in the target direction for the (3 × 3) cm^2 fields, which decreased to 1.025 for (6 × 6) cm^2 fields, and it was found that no correction was required for fields of (10 × 10) cm^2 or larger.

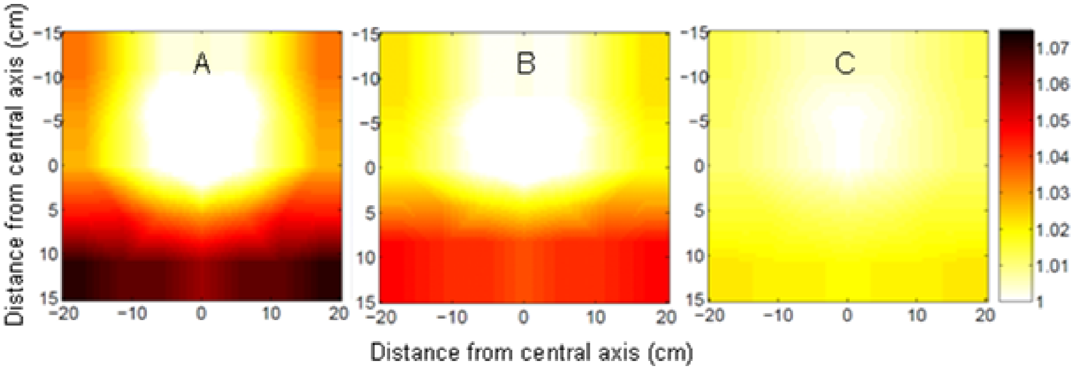

Figure 6.6. The correction matrices obtained, correcting for a combination of non-uniform backscatter and off-axis response. A) (3 × 3) cm^2, B) (4 × 4) cm^2 and C) (6 × 6) cm^2 fields. Positions in cm at the level of the imager.

The IMRT verification results obtained including this correction matrix method for rectification of non-uniform backscatter effects are given in table 6.2. It can be seen that the average number of points passing the gamma criteria of 3%, 3 mm increased from 96.4% to 97.9%. Although there is only a marginal improvement in the average gamma passes, the variation of the results also decreased, the standard deviation halving from 3.3 to 1.6%. Additionally, it can be seen that there was a marked improvement for all beams for which more than 10% of points initially failed the gamma criteria (for beams with small off axis segments). 100% of beams had a pass rate of greater than 90% with the correction for backscatter included, with 6% failing these criteria without the correction for backscatter included.

Patient	**1**	**2**	**3**	**4**	**5**	**6**	**7**	**8**	**9**	**10**	**Overall**
Beam											
1	99.20	99.05	99.40	99.50	98.10	98.90	96.20	98.60	91.20	99.70	
2	98.40	98.38	98.50	98.10	98.50	98.80	98.60	97.80	97.90	98.60	
3	98.10	98.20	97.50	98.60	98.60	97.80	97.60	97.80	95.40	98.00	
4	99.10	98.80	99.20	98.30	98.60	97.60	97.90	99.00	96.40	93.20	
5	97.80	97.63	95.90	98.40	98.40	97.00	98.00	99.40	97.30	98.10	
6	99.50	98.57		97.00	99.20	96.80	98.70	98.60		98.20	
7	97.10	96.10		92.90	98.30	99.20	96.90	98.00		99.10	
8					98.80	97.10		98.80		97.10	
9					93.10	98.80		98.60		96.10	
10					97.40	95.70		99.10			
11					98.70	98.60					
12						99.40					
13						99.20					
14						99.50					
Average	**98.33**	**98.10**	**98.10**	**97.54**	**97.97**	**98.17**	**97.70**	**98.57**	**95.64**	**97.57**	**97.89**
σ	**0.87**	**0.99**	**1.44**	**2.18**	**1.68**	**1.17**	**0.90**	**0.55**	**2.66**	**1.95**	**1.55**

Table 6.2. Gamma pass results for 3%, 3 mm with the devised correction for backscatter included. σ denotes the standard deviation.

Figure 6.7 shows the gamma map and the local dose percentage difference for beams 5 and 6 of patient 6, with the correction for non-uniform backscatter included. It should also be noted that at the delivered dose-rate of 300 MU min^{-1} there are also IMRT dose delivery errors of approximately 0.3 MU present for significant areas of these beams due to dose contributions from the first segment but not the final segment, which corresponds to 1 to 2% local dose difference for the areas of interest. Segments 1 to 4 of beam 5 are previously given in figure 6.3.

6. 4 Discussion

Correction for non-uniform backscatter from the imager arm and ancillary components downstream of the imager is a current problem for those wishing to perform dosimetric verification on Varian linacs (as detailed in previous chapter). One of the most recent papers on this topic, Berry *et al*. (2010) uses similar methods as those described here to address the problems associated with field-size and position on the imager. They have described two methods of correction, the first involving acquired correction matrices, and the second involving a field-size specific correction algorithm derived from the correction matrices. However, their correction matrices were sampled from a limited number of symmetric field sizes from (2 × 2) cm^2 to (30 × 40) cm^2 positioned on the central axis and so the method presented here is a more detailed evaluation of image intensity with field-size and position. Additionally, they applied the nearest correction matrix large enough to cover the entire irradiated field, and so, for example, for a Y2 jaw position of 8.8 cm, the matrix for an (18 × 18) cm^2 field is applied. Their algorithm for the smaller fields was based on extrapolation and not measurement of small, off-axis fields.

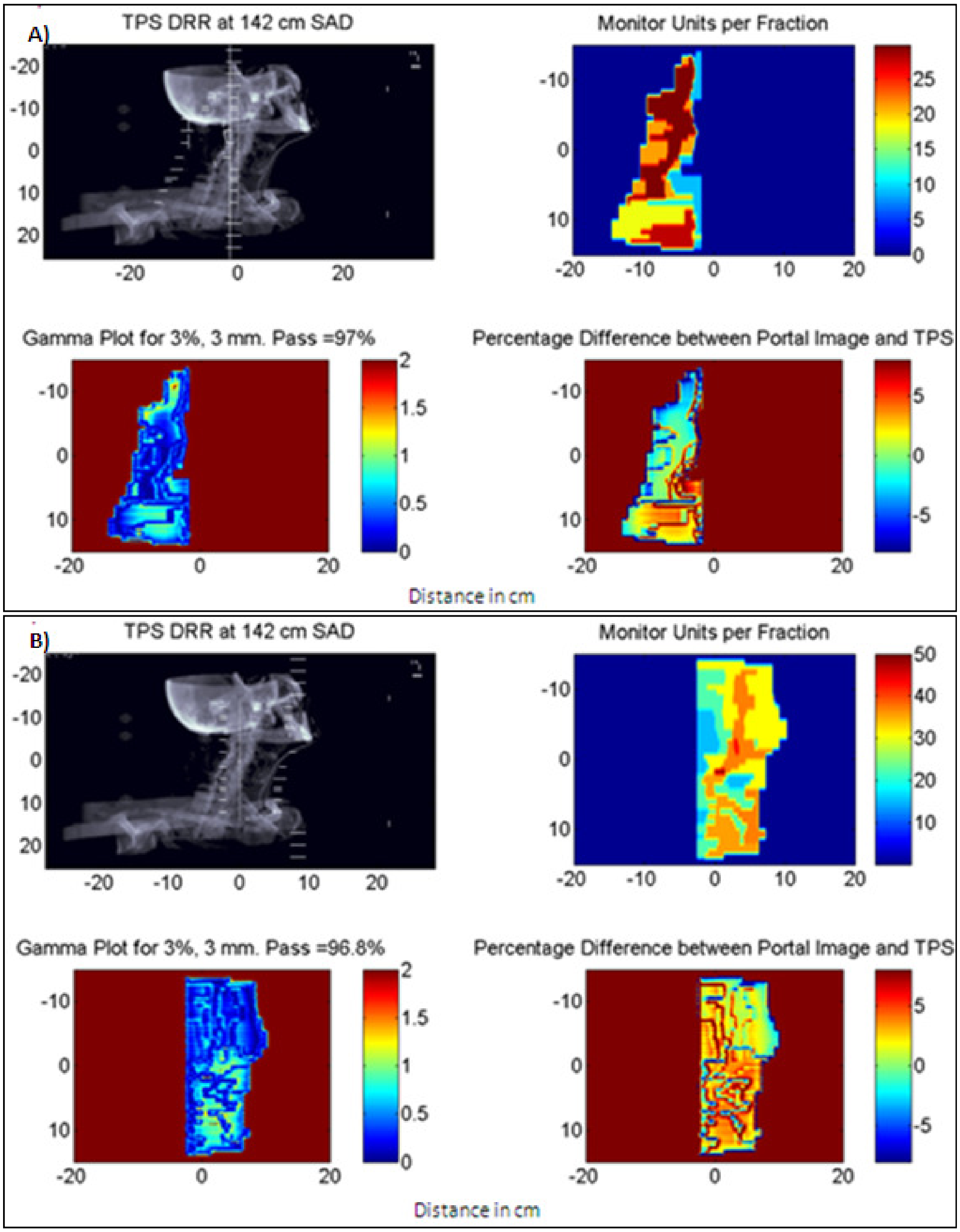

Figure 6.5. Results with non-uniform backscatter correction included for A) Patient 6, beam 5 and B) Patient 6, beam 6. The TPS digitally reconstructed radiographs (DRRs) at the imager source to axis distance (SAD) are also shown. NB The area outside the beam has been excluded from all calculations and therefore should not be interpreted according to the colour scale.

In contrast, the method described in this chapter applies a correction matrix for every IMRT segment based on off-axis measurement and EWWF defined by the MLC. This solution is novel and versatile, the methodology lending itself to all other EPID dosimetry methods, regardless of dose calculation algorithms used. As previously mentioned, measurement or MC simulation could be used as an alternative to TPS calculated doses for these off-axis fields.

6.5 Conclusions

The results to date show this technique to be an efficient method of IMRT pre-treatment dose verification. The results were partly presented (in the form of a poster presentation) at the UK Radiation and Oncology Conference (UKRO) 2009 (Cufflin *et al.* 2009a). The process is time efficient, requiring 10 minutes per patient on the linac and taking only a few minutes to calculate on the TPS. The devised correction for non-uniform backscatter improved agreement between predicted and measured EPID intensities, average gamma pass results are improved from 96% ($\sigma = 3.3$) to 98% ($\sigma = 1.6$), with a significant improvement of results for any fields with small segments off-axis in the target direction. At least 90% of all beams passed the gamma criteria of 3%, 3 mm.

Chapter 7

Application of INtegrated TReatment Planning and EPID Dosimetry (INTREPID) Method for Exit Dosimetry

7.1 Introduction

Progressing the description in previous chapters of pre-treatment EPID dosimetry techniques, two methods of transit EPID dosimetry (that verify the correct dose delivery during treatment) have also been developed as a part of this work. The first, the focus of this chapter, calculates the IMRT dose at the exit plane within the TPS. A series of pre-calculated correction factors, dependent on patient thickness, field size and position, are used to convert the dose (to a water equivalent medium) at the detector level to EPID image intensity, for comparison against patient acquired EPID images. The second method, as described in detail in the following chapter, involves a full forward MC calculation of portal dose.

As treatment plans and processes become more complex, the risk of potential errors increases, but they become more difficult to detect. The ultimate aim of radiotherapy dose verification is to ensure that all potential errors, whether they arise from the TPS dose calculation, incorrect patient positioning, changes in patient anatomy, data transfer malfunctions or linac functioning or calibration issues, are identified. The overall aim is to ensure that all patients get their treatment as planned. EPID dosimetry techniques, alongside image guided radiotherapy (IGRT) methods such as 3D cone beam CT, should enable the majority of errors undetected by other methods to be identified and corrected for.

Errors arising from the TPS may be due to incorrect modelling of MLC transmission, inability to model inter-leaf leakage, incorrect Hounsfield Unit (HU) to electron density (ED) conversion of CT data or a weakness in the calculation algorithm used. For IMRT treatments it is imperative that the TPS models leaf transmission correctly. The collimators (jaws) remain static for each IMRT beam on our Varian 2100 linacs, and so errors in TPS leaf transmission become significant for beams comprising many segments. Incorrect HU to ED conversion becomes more pronounced for larger patient thicknesses due to a greater absolute error in calculated radiological depth, or effective depth relative to water. MC simulations carried out as a part of this work have shown that at 6 MV a 2% error in calculated radiological depth at 10 cm deep would result in a dose error of less than 1%, but the error in calculated dose would be almost 3% at 35 cm deep. Therefore HU to ED conversion errors become significant when performing exit dose calculations for large patients.

Changes in patient anatomy between planning CT and treatment, or throughout the course of treatment, may be due to weight loss or gain, the emptying or filling of a body cavity, or tumour shrinkage as a response to treatment. Care should be taken within every radiotherapy department to set up adequate protocols for scanning and treatment to ensure that patient positioning and anatomy are as reproducible as possible throughout the course of treatment.

All centres delivering radiotherapy are required to have a thorough system of routine machine quality control (QC) in place to ensure any changes in machine functioning or calibration are detected (Mayles *et al.* 1999). Additionally, all centres delivering complex treatments, such as IMRT, should have a thorough system of MLC QC in place to ensure the leaves are being driven to the correct position. However, even the most rigorous systems of routine QC cannot completely prevent a machine occasionally malfunctioning during treatment. EPID dosimetry techniques should enable the magnitude and consequence of any machine faults to be assessed, as well identifying any accidental changes to plan parameters, whether they be due human or computer errors (Mans *et al.* 2010).

As already stated in the introduction (chapter 1), published transmission dosimetry techniques include (i) point dose verification by back-projection methods to a set location (usually 5 cm deep or the isocentre) within the patient, (ii) 2D transit dose verification at EPID level, (iii) 2D dose verification at the patient level (either exit dose or mid-plane) and (iv) 3D dose calculation within the patient, either by a back-projection dose calculation algorithm or back-projection of energy fluence and forward calculation of dose within the patient.

Van Elmpt *et al.* (2008a) point out the vast range of publications in the literature yet current lack of commercially available transmission (or transit) dosimetry solutions. 'Dosimetry Check' from Math Solutions (see chapter 1, section 1.5), based on the methods presented by Renner *et al.* 2005, claims to be the first commercial EPID based transit dosimetry solution. A preliminary study at Edinburgh Cancer Centre, with a poster presentation at the IPEM Biennial Radiotherapy meeting (Sankar *et al*. 2010), showed agreement between EPID measurements and TPS dose of 3.67 ± 0.8% at the isocentre for phantom studies.

The first clinical case showed agreement between EPID image and TPS of 5.8% at isocentre.

The method developed as a part of this work involves 2D transit verification at the EPID level by calculation of dose to a water equivalent 'EPID' within the TPS, using the CC algorithm available within our TPS. Conversion to EPID image intensity is achieved through application of a series of pre-calculated correction factors dependent on patient thickness and segment size, shape and location on the imager. Several other groups have used the TPS and / or convolution superposition algorithms to calculate the dose at the EPID level (McNutt *et al*. 1996, Dahlgren *et al*. 2002, 2006, Mohammadi *et al*. 2006, Reich *et al*. 2006). However, these publications relate to older EPID models, e.g. the Scanning Liquid Ion Chamber (SLIC) EPID (van Herk and Meertens 1988) and charged coupled device (CCD) EPIDs. The SLIC EPID was essentially water equivalent and, as water is the reference medium for radiotherapy dosimetry, the conversion to EPID intensity was much simpler than for the higher effective atomic number and density of the a-Si EPID. In addition, these papers refer to phantom studies only. The author is unaware of clinical studies using these techniques being published at this time.

The UK report 'Towards Safer Radiotherapy' has expressed support for the development of EPID-based approaches to patient dose verification. In line with this, the aim of this work is to set up an accurate and efficient method of verifying our clinical IMRT plans at treatment time using the Varian aS500 EPID. The technique is readily transferrable to the EPIDs provided by other linac vendors.

7.2 Methods

All dose distributions are planned and optimised on OMP. OMP has versatile DICOM export and import functions, enabling the patient CT dataset and treatment parameters to be exported and then imported into Matlab software (developed for this project), where it can be rotated around the plan isocentre by the relevant gantry angle and the water equivalent 'EPID' layer attached at the appropriate level and position. The modified CT data is then re-imported into OMP (see figure 7.1) to enable calculation of dose in water at the EPID level. The process for rotation and addition of the EPID is similar to that described in Chapter 8 for creation of MC phantom files, but the final product is a modified CT dataset.

The OMP calculated dose to water equivalent 'EPID' is exported and a series of correction factors applied within Matlab to convert to EPID image intensity. The four correction factors applied are (i) conversion from dose in water to EPID image intensity, (ii) a field-size dependent output factor to account for the difference between water and EPID field size factors, (iii) an off-axis correction matrix to account for effects of off–axis beam ‘softening’ at different depths and (iv) correction for non-uniform backscatter from the Varian EPID support arm and cabling. A process map describing the procedure is given in figure 7.2.

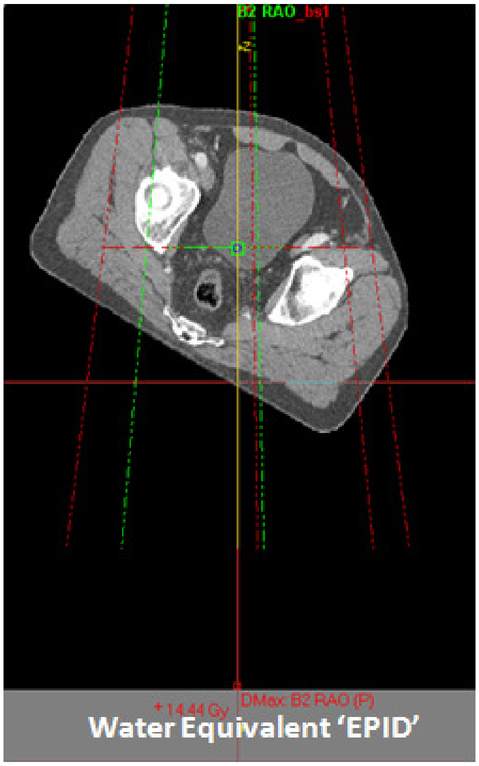

Figure 7.1. Rotated CT data set and attached ‘EPID’ within the TPS.

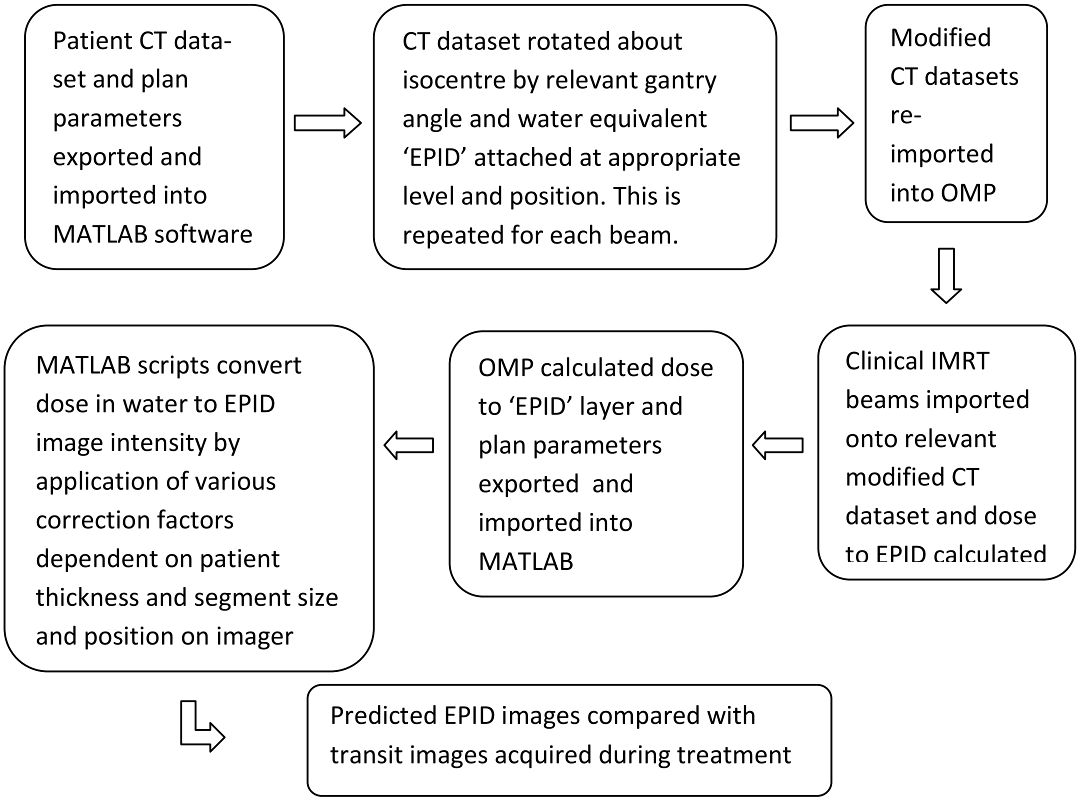

Patient CT dataset and plan parameters exported and imported into MATLAB software

CT dataset rotated about isocentre by relevant gantry angle and water equivalent 'EPID' attached at appropriate level and position. This is repeated for each beam.

Modified CT datasets re-imported into OMP

Clinical IMRT beams imported onto relevant modified CT dataset and dose to EPID calculated

OMP calculated dose to 'EPID' layer and plan parameters exported and imported into MATLAB

MATLAB scripts convert dose in water to EPID image intensity by application of various correction factors dependent on patient thickness and segment size and position on imager

Predicted EPID images compared with transit images acquired during treatment

Figure 7.2. Process map for INTREPID transit dosimetry.

7.2.1 Verification of Dose Calculation at the Exit Plane

MC simulations were used to evaluate the ability of the TPS to calculate doses correctly at the exit plane for the variety of algorithms available on OMP; the standard or 'classic' PB and CC algorithms and the newer 'enhanced' CC algorithm, more detail on these algorithms being given in chapter 2. The CC 'enhanced' calculation is more suited to this work due to the modelling of MLC inter-leaf leakage, faster calculation times and improved calculation matrix resolution over the CC 'classic' calculation. Water equivalent thicknesses of 5, 9, 15, 20, 25, 30 and 35 cm were investigated. Figure 7.3 shows the set-up for calibration of the system.

MC simulations of our Varian 2100 CD linacs with aS500 EPIDs were performed using the BEAMnrc and DOSXYZnrc codes, which make it relatively easy to replicate the exact set-up both on our Varian accelerators and within the TPS. It should also be noted that the work described in this chapter was carried out for comparison with full-forward MC calculation of portal dose using these codes (as described in the next chapter). The TPS based technique has the advantage that results can be obtained more quickly in a clinical setting and it includes the initial TPS dose calculation that the patient plan approval was based upon, and so combines verification of the TPS dose calculation with verification of treatment delivery.

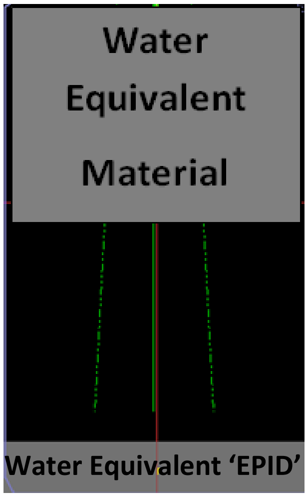

Figure 7.3. The calibration set up for MC, TPS calculation and measurement.

7.2.2 Hounsfield Unit to Electron Density Conversion

Correct calculation of dose at the exit plane is also dependent on correct HU to ED[8] conversion, both at the CT scanner and within the TPS. Therefore the scanner and TPS HU to ED curves were compared against each other and against the formulae presented by Thomas 1999 (equations 7.1 and 7.2).

$$HU = (ED-1) \times 1000 \qquad (7.1)$$

for tissues of densities less than that of bone, and

$$HU = (ED-1) \times 1950 \qquad (7.2)$$

for bone densities.

The HU to ED conversion for the scanner was determined by scanning the CIRS Model 062 phantom[9] (figure 7.4) with a range of tissue equivalent ‘nested disks’ of known densities for the various clinical protocols used. The HU to ED conversion for OMP was obtained from the Oncentra® MasterPlan v3.3 Physics and Algorithms Manual.

---

[8] It should be noted that generally within radiotherapy, and within this thesis, ED refers to the electron density relative to that of water.

[9] http://www.cirsinc.com/062_rad.html

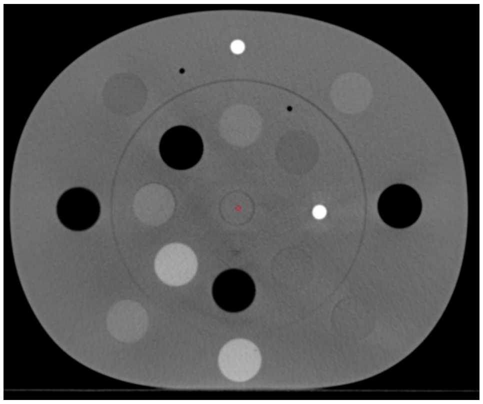

Figure 7.4. CT scan of CIRS electron density phantom.

7.2.3 Determination of Correction Factors

7.2.3.1 Correction Factor 1: OMP Dose in Water to EPID Image Intensity

For conversion of OMP dose in water to EPID image intensity, every IMRT segment is considered as comprising two components; the primary beam and the 'leakage' portion transmitted through the MLC. MC simulations were used to compare dose in water with dose in EPID both within the field (for a standard (10 × 10) cm^2 aperture) and beneath the MLC, enabling dose conversion factors to be obtained. These factors were initially obtained for transmission through thicknesses of water equivalent material from 6 cm up to 35 cm (as this was the maximum thickness of 'solid water' material available locally at the time this work was carried out), although this range needs to be extended for the full range of patient thicknesses that may be encountered.

7.2.3.2 Correction Factor 2: Field Size Output Factors

The variation of EPID and water field size output factors with increasing tissue thickness was investigated. The EWWF (defined in Chapter 6) was calculated for every IMRT segment, enabling the field-size output factor (accounting for the difference between water and EPID field size factors) to be applied.

7.2.3.3 Correction Factor 3: Off-Axis Calibration Matrices

Additionally, the variation of EPID response compared with dose in water for 'off-axis' positions due to beam spectral changes was investigated for water equivalent thicknesses of 6 cm to 35 cm.

7.2.3.4 Correction Factor 4: Correction for Non-Uniform Backscatter

As detailed in previous chapters, correction for non-uniform backscatter from the Varian support arm and cabling was required. The matrix-based method described in Chapter 6 was adapted to account for different tissue thicknesses.

These correction matrices, dependent on tissue thickness, segment size and position on the imager, were acquired by irradiating the imager with a series of fields (from (3 × 3) cm^2 to (12×12) cm^2) with matching edges to cover the entire detector area, for thicknesses of water equivalent material from 6 cm to 35 cm. Equivalent fields were calculated on the TPS, enabling field size and tissue thickness dependent correction matrices to be produced.

7.2.4 EPID Positional Stability with Gantry Angle

Iori *et al.* 2010 reported the positional reproducibility of the support arm to be the biggest hurdle when using the Varian EPID for IMAT verification. However, this paper referred to the older ‘R’ arm, whereas the work in this thesis has been carried out with an EPID on the newer ‘Exact’ arm, which is known to have superior mechanical alignment with gantry angle over the ‘R’ arm. The ‘R’ arm will have to be considered when extending this work as two of our older EPIDs have this arm. The study by Grattan and McGarry [2010] reported that their largest measured misalignments from EPID stated values for the Exact arm were a lateral shift of -0.4 ± 0.3 mm and a longitudinal shift of $+1.9 \pm 0.9$ mm, both at gantry angle 180°. These reported misalignments were within the specified manufacturer tolerance of 3 mm from EPID values. Although work is under way to investigate EPID position and reproducibility with gantry angle for the EPIDs at VCC Cancer Centre, for the purposes of this work predicted EPID images were shifted in 2D to obtain the best match with acquired EPID images. This method should also maintain the correct back-scatter and off-axis correction. Additionally, the vertical position of the imager also varies slightly with gantry angle and so the reported position was obtained from the DICOM information and image scaling and inverse square law corrections applied for any slight offsets.

7.2.5 Clinical IMRT Treatment Verification

The technique was initially validated for IMRT fields through water equivalent material at a gantry angle of 0°, before moving on to validate the technique for a Alderson Rando anthropomorphic phantom (figure 7.5), and then finally to verify actual patient IMRT treatments with variable gantry angles.

A clinically prepared head and neck IMRT plan of 14 beams was used to verify the technique for thicknesses of water equivalent material of 15, 21, 25 and 35 cm. A single (10 × 10) cm^2 field and 10 beams from a prostate plus pelvic nodal IMRT plan were used to verify the technique on the Rando phantom. To date, 68 clinical exit dosimetry beams have been evaluated, from a combination of 4 head and neck and 4 prostate plus pelvic nodal IMRT plans.

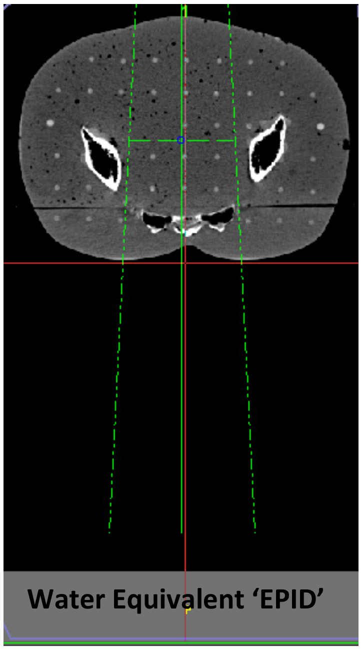

Figure 7.5. Transverse CT slice of the Rando anthropomorphic phantom with attached 'EPID'.

7.3 Results

7.3.1 Verification of Dose Calculation at the Exit Plane

Figure 7.6 shows the dose calculation through different thicknesses of water equivalent material for the MC simulation and OMP CC 'classic', CC 'enhanced' and PB 'classic' algorithms. MC verified the ability of OMP CC algorithms to calculate the transmitted dose correctly at the EPID level, there being very good agreement between the CC 'classic' algorithm and MC simulation for all thicknesses investigated (a difference of less than < 0.5%). The CC 'enhanced' algorithm showed similarly good agreement for water equivalent thicknesses of 5, 9, 30 and

35 cm, but a 1.5% difference between CC 'enhanced' and 'classic' was observed for thicknesses of 15, 20 and 25 cm. This is being investigated further and may be due to the local implementation of the algorithm. This work also proved the unsuitability of the PB algorithm for this work, with a difference of up to 15% between PB calculation and MC simulation for a thickness of 35 cm of water equivalent material. Due to calculation matrix resolution issues when using the CC 'classic' algorithm for these very large extended phantom geometries, a decision was made to use the CC 'enhanced' algorithm for the remainder of this work.

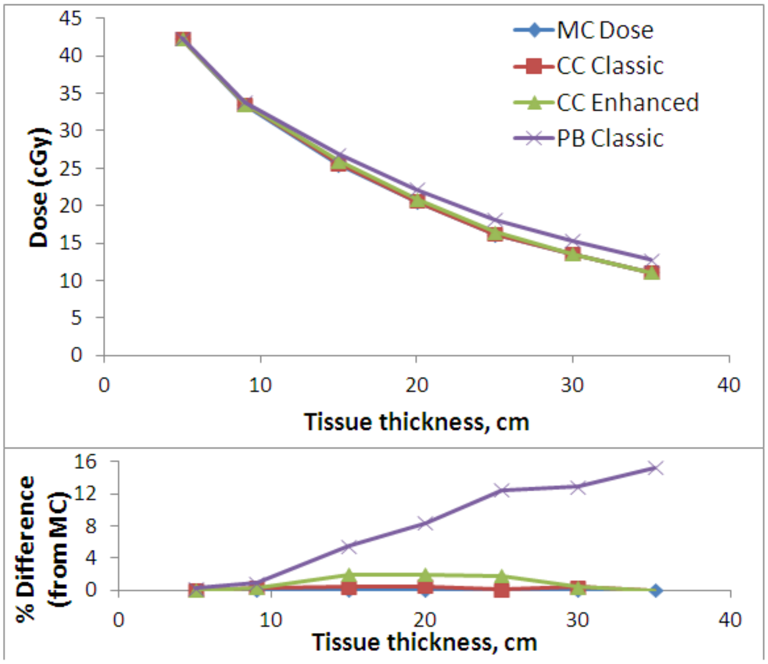

Figure 7.6. Dose calculation through different thicknesses of water equivalent material for MC simulation and Oncentra Masterplan CC 'classic', CC 'enhanced' and PB 'classic' algorithms. It should be noted that due to the excellent agreement between MC and CC 'Classic', many of the MC data points are hidden behind the CC 'Classic' data points.

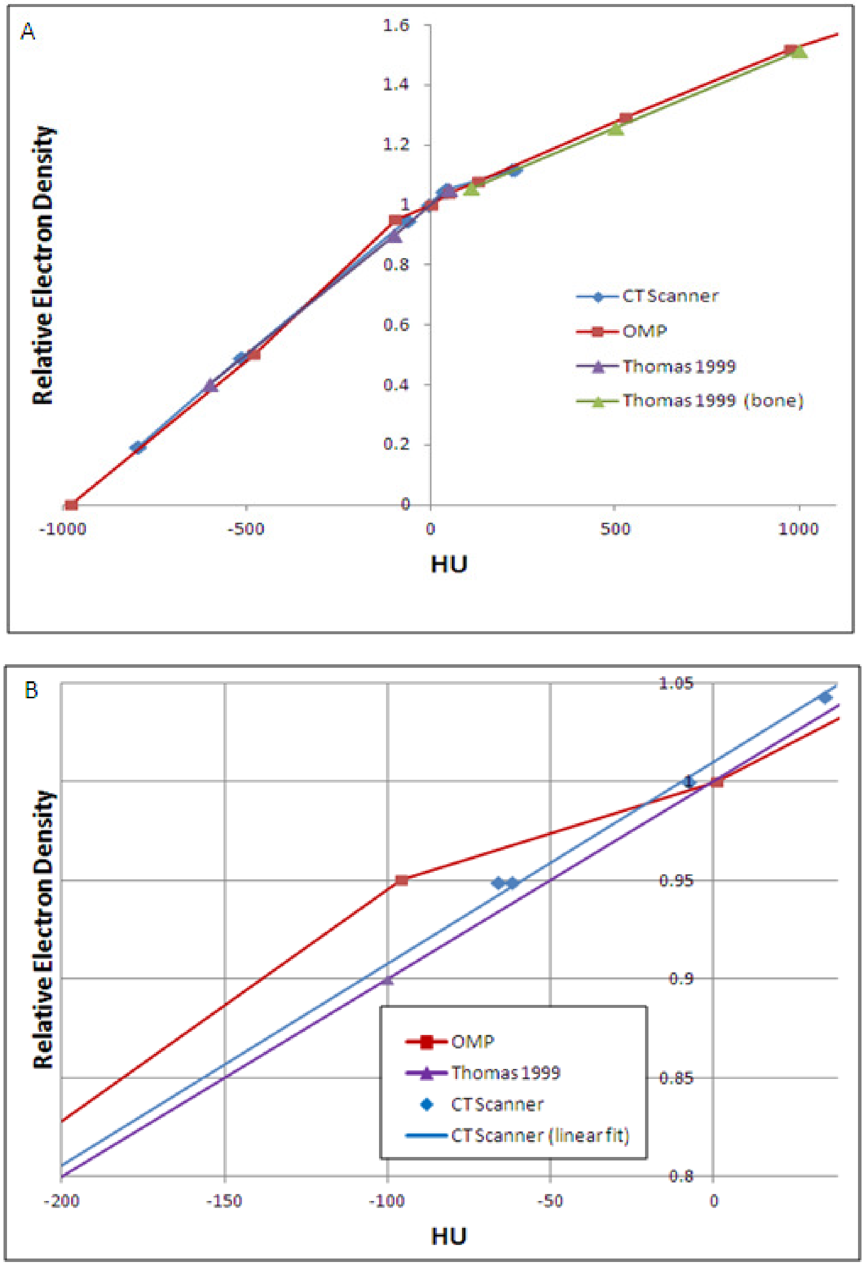

Figure 7.7. Relative electron density versus HU for the VCC scanner, Oncentra Masterplan (OMP) and calculated using Thomas 1999. From figure 7.7a it can be seen that in general there is good agreement between all three curves, although there is a discrepancy between the OMP and scanner HU to ED conversion around HU of -96 (figure 7.7b), which corresponds to adipose / fat tissue.

7.3.2 Hounsfield Unit to Electron Density Conversion

The graphs in figure 7.7 show the three calibration curves for the CT scanner (the scanner's prostate protocol is shown, although this is very similar to all other clinical protocols used), OMP and for the method for converting ED to HU described by Thomas 1999. It can be seen that there is generally good agreement for all three curves, except in the region around HU of -96. OMP assigns an ED of 0.95 for HU equal to -96, but the formula presented by Thomas 1999 gives an ED equal to 0.904 for this HU, a difference in ED of 5%. The CT scanner curve more closely matches that presented by Thomas 1999, an ED of approximately 0.91 corresponding to HU of -96.

The graph in figure 7.7b suggests that OMP over-estimates the ED for materials of HU in the region -200 to -50, which mainly corresponds to patient adipose or fat tissues. However, this is only likely to become an issue with patients with a large amount of adipose or fat tissue in the beam path. For example, for a large prostate patient with 10 cm adipose tissue in the beam path, a mis-calculation of radiological depth by 0.5 cm would result in approximately 2% error in the dose calculation. Dose errors are therefore likely to be less than 1% at isocentre for most patient cases.

7.3.3 Determination of Correction Factors

7.3.3.1 Correction Factor 1: OMP Dose in Water to EPID Image Intensity

As expected, both dose in water and EPID image intensity followed an approximate exponential with increasing patient thickness (figure 7.8). The ratio of the two curves was found to vary with depth and so a tissue thickness dependent conversion factor was required.

For transit verification based on patient CT, the TPS calculated radiological depth at the central axis was used for this position. The radiological depth at all other calculation points was approximated by calculating the dose for a large beam at the exit plane within the TPS and comparing the dose at all points against the central axis dose. An approximation that mean attenuation in tissue is 4% per cm is currently used, based on the MC simulation results. Relative dose under the MLCs was found to be 25 – 35% greater in EPID than for water equivalent material. A value of 30% was used in this work.

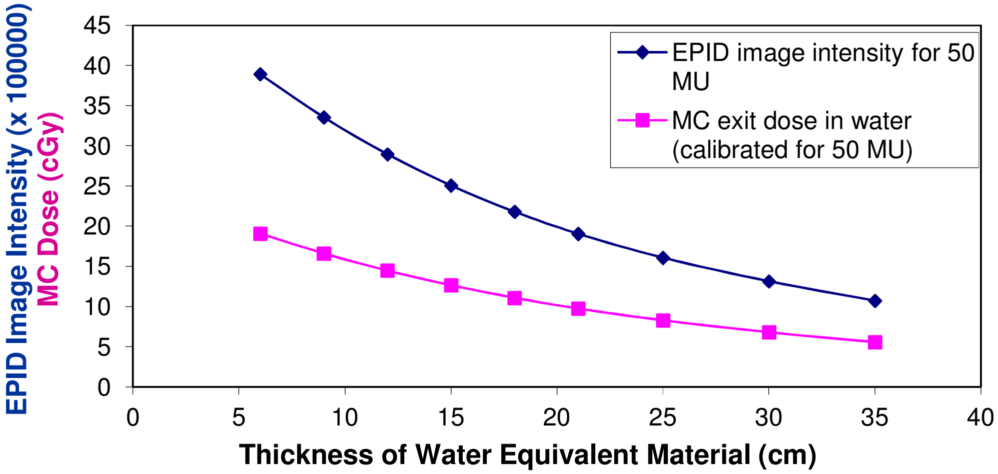

Figure 7.8. EPID intensity and MC exit dose in water for varying thickness of water equivalent material.

7.3.3.2 Correction Factor 2: Field Size Output Factors

The average ratio of EPID field size output factor to water field size output factor for thicknesses of water equivalent material of 6 cm to 35 cm are shown in figure 7.9. The factors were not found to vary significantly with depth, and so a standard correction factor for a given field was applied for all depths (the maximum standard deviation being 1.1% for an equivalent square of 15 cm).

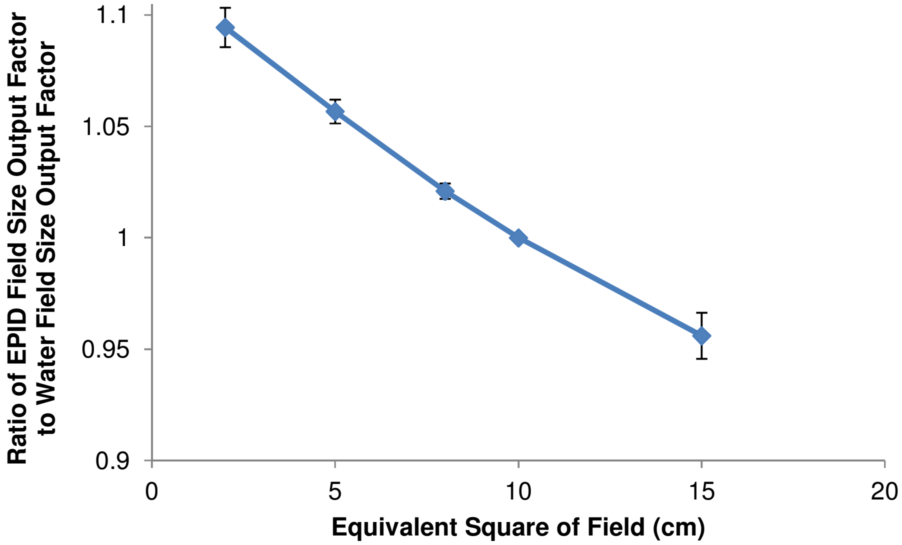

Figure 7.9. Average ratio of EPID field size output factor to water field size output factor, for thicknesses of water equivalent material of 6 cm to 35 cm.

7.3.3.3 Correction Factor 3: Off-Axis Correction Matrices

Figure 7.10 illustrates the ratio of EPID image intensity to dose in water for a large beam exiting different thicknesses of water equivalent material The results of these measurements proved it necessary to apply different water to EPID off-axis correction matrices for all tissue thicknesses to account for the differing EPID response to spectral variations in the beam with distance away from central axis and with depth.

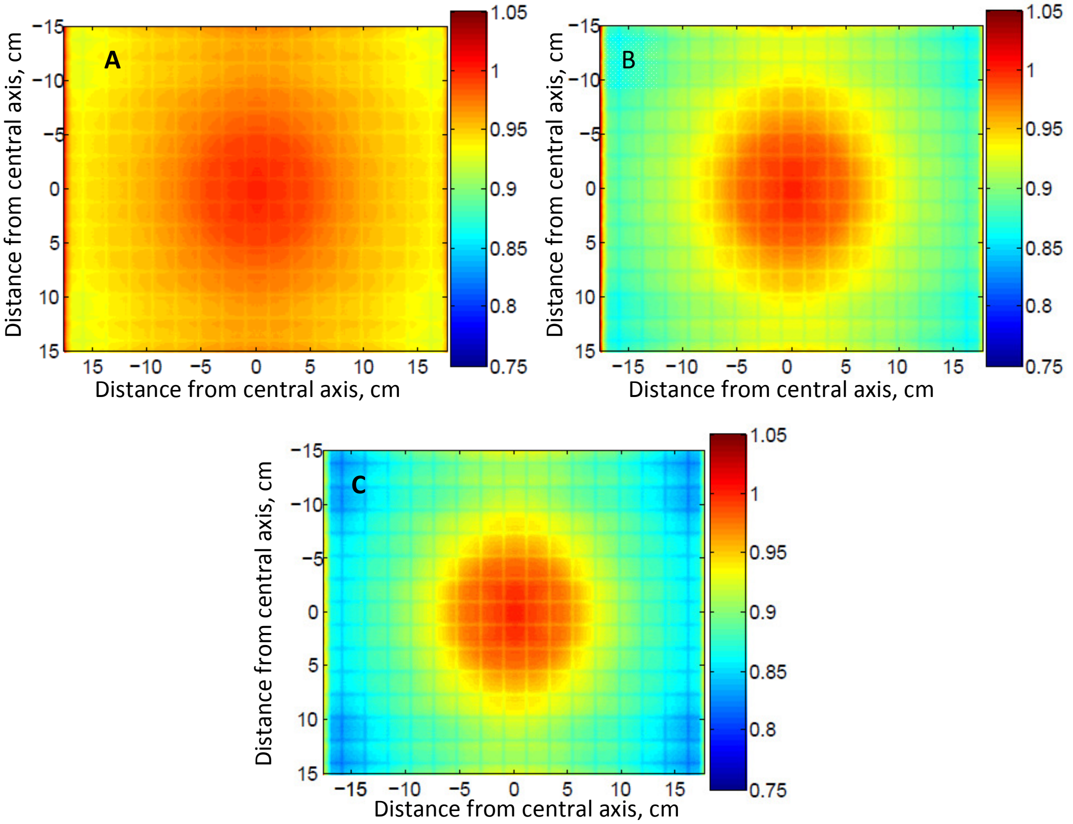

Figure 7.10. Off-axis correction. Ratio of EPID image intensity to dose in water for beam exiting A) 10 cm, B) 20 cm and C) 30 cm thickness of water equivalent material. The grid visible is due to the attenuation of the 'tennis racquet' couch top.

7.3.3.4 Correction Factor 4: Correction for Non-Uniform Backscatter

Figure 7.11 shows example correction matrices for non-uniform backscatter with (5 × 5) cm^2 fields for thicknesses of 10 cm and 20 cm water equivalent material. It can be seen that different correction matrices are required for different tissue thicknesses, correction values increasing with increasing patient thickness. As in figure 6.6 in the previous chapter, a greater correction is required for the inferior portion of the EPID due to non-uniform backscatter from supporting structures.

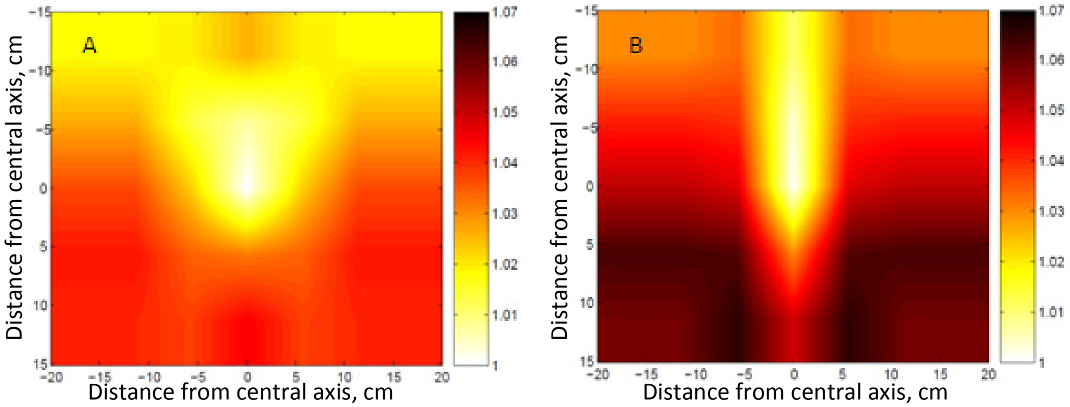

Figure 7.11. Matrices for correction for non-uniform backscatter through a) 10 cm water equivalent material and b) 20 cm water equivalent material for (5 × 5) cm^2 fields.

7.3.4 EPID Positional Stability with Gantry Angle

Initial measurements found the maximum displacement of the centre of the imager panel from the stated position to be 0.4 mm laterally and 1.6 mm longitudinally, both for gantry angle 180°. However, the reproducibility of position with gantry angle for our EPIDs is yet to be determined and so, as already stated, a 2D shift to best align predicted images with acquired images is currently performed.

7.3.5 IMRT Plan Verification

Results for transit IMRT verification through homogeneous water equivalent material were very good, an average of 96% and 98% of points passing gamma criteria (gamma < 1) of 3%, 3 mm and 4%, 4 mm respectively, for thicknesses of water equivalent material of 15, 21, 25 and 35 cm. However, for a (10 × 10) cm^2 beam incident on the Rando phantom there was a discrepancy of approximately 4.5% on the central axis. Further investigation revealed the ratio of measured radiological depth to physical depth for Rando to be much lower than that for standard patients, the ratio being approximately 0.9. From figure 7.7b it can be seen that Rando's relative electron density corresponds to the region with the greatest disparity between the scanner and OMP HU to ED conversion curves. It is believed that adjustable HU to ED curves will be available in a new release of OMP, but this is not available at present. As this is an extreme situation (Rando consists of more than 20 cm of fat / adipose equivalent tissue), in order to correct for this the Rando CT data set was adjusted within Matlab to enable the correct ED to be applied within OMP (to ensure correct calculation of radiological depth). This greatly improved agreement between prediction and measurement, there being less than a 1% difference for a (10 × 10) cm^2 exit dosimetry field. With the 'corrected' CT data, an average of 95% of points passed gamma criteria of 4%, 4 mm and an average of 98% of points passed gamma criteria of 5%, 5 mm for 10 fields from a prostate patient IMRT plan.

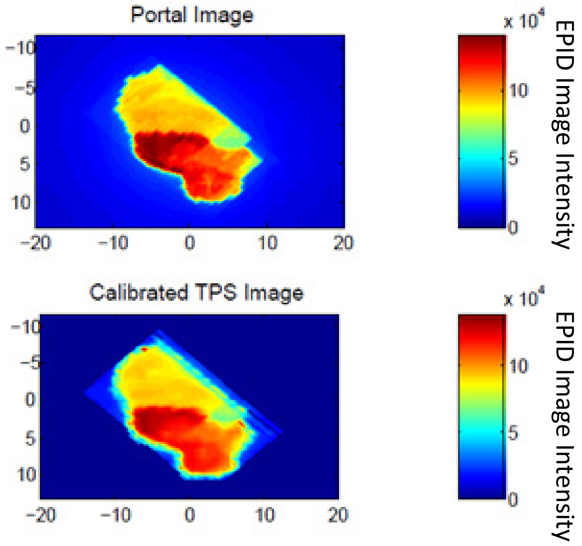

Figure 7.12. Acquired EPID Image and Calibrated TPS Image for a prostate beam. NB The area outside the beam has been excluded from all calculations and therefore should not be interpreted according to the colour scale.

Patient Number	Region	Number of beams	Average percentage of points passing gamma 5%, 5 mm	Standard deviation (%)
1	Head and neck	14	97.6	2.2
2		8	96.1	2.9
3		10	96.4	2.7
4		5	96.0	3.3
5	Prostate plus nodes	8	98.5	1.0
6		10	91.4	8.5
7		7	95.3	3.8
8		6	96.9	3.4
Overall Average		**68**	**96.0**	**3.5**

Table 7.1. Average percentage of points passing gamma criteria of 5%, 5 mm (gamma < 1) for 8 patients evaluated. Anterior and anterior oblique beams exiting couch bars have been removed.

To date a total of 68 beams from 4 head and neck and 4 pelvic plans have been evaluated, with an average of 96% of points passing gamma criteria of 5%, 5 mm (when all anterior and anterior oblique beams that exit couch bars are removed as these are not accounted for within the TPS). Table 7.1 summarises all results obtained and figure 7.11 gives the visual result obtained for a clinical prostate plan.

It can be seen from table 7.1 that the results for patient 6 were noticeably poorer than the results for the other 7 patients evaluated. Detailed results for this patient, and a comparison with MC simulation are given in table 7.2. The availability of the full-forward MC technique allows for a direct comparison using the same pre-treatment CT set to aid in identifying the cause of any discrepancies. It can be seen that there is very good agreement between TPS technique and MC simulation for all beams, both techniques showing poor verification results for beams 2, 5, 6 and 9. Further analysis of this patient's scan revealed the patient to have a very full bowel during initial planning scan, and all 4 beams with poor verification results corresponded to beams with a lot of bowel in the beam's eye view. It is therefore unlikely that the patient retained this full bowel throughout treatment. Figure 7.13 shows the CT scan, beam's eye view and gamma maps for beams 5 and 6.

Beam Number	**TPS Based Technique versus acquired EPID Image 5%, 5 mm**	**MC Simulation versus acquired EPID image 5%, 5 mm***	**TPS Based Technique versus MC Simulation 5%, 5 mm***
1	99%	98%	99%
2	***76%***	***77%***	***100%***
3	97%	99%	100%
4	98%	95%	100%
5	***78%***	***71%***	***100%***
6	***90%***	***91%***	***99%***
7	96%	95%	100%
8	95%	99%	99%
9	***87%***	***77%***	***99%***
10	99%	98%	100%
Mean	**91%**	**90%**	**99%**

Table 7.2. Detailed gamma pass results for patient 6. 4 beams (italicised) demonstrate poor verification results. It should be noted that for beams such as beam 5 with very good agreement between TPS and MC simulation, a larger difference in TPS versus EPID is due to the abrupt cut off of 5%, 5 mm.

* uncertainty on MC simulation 1 -2%

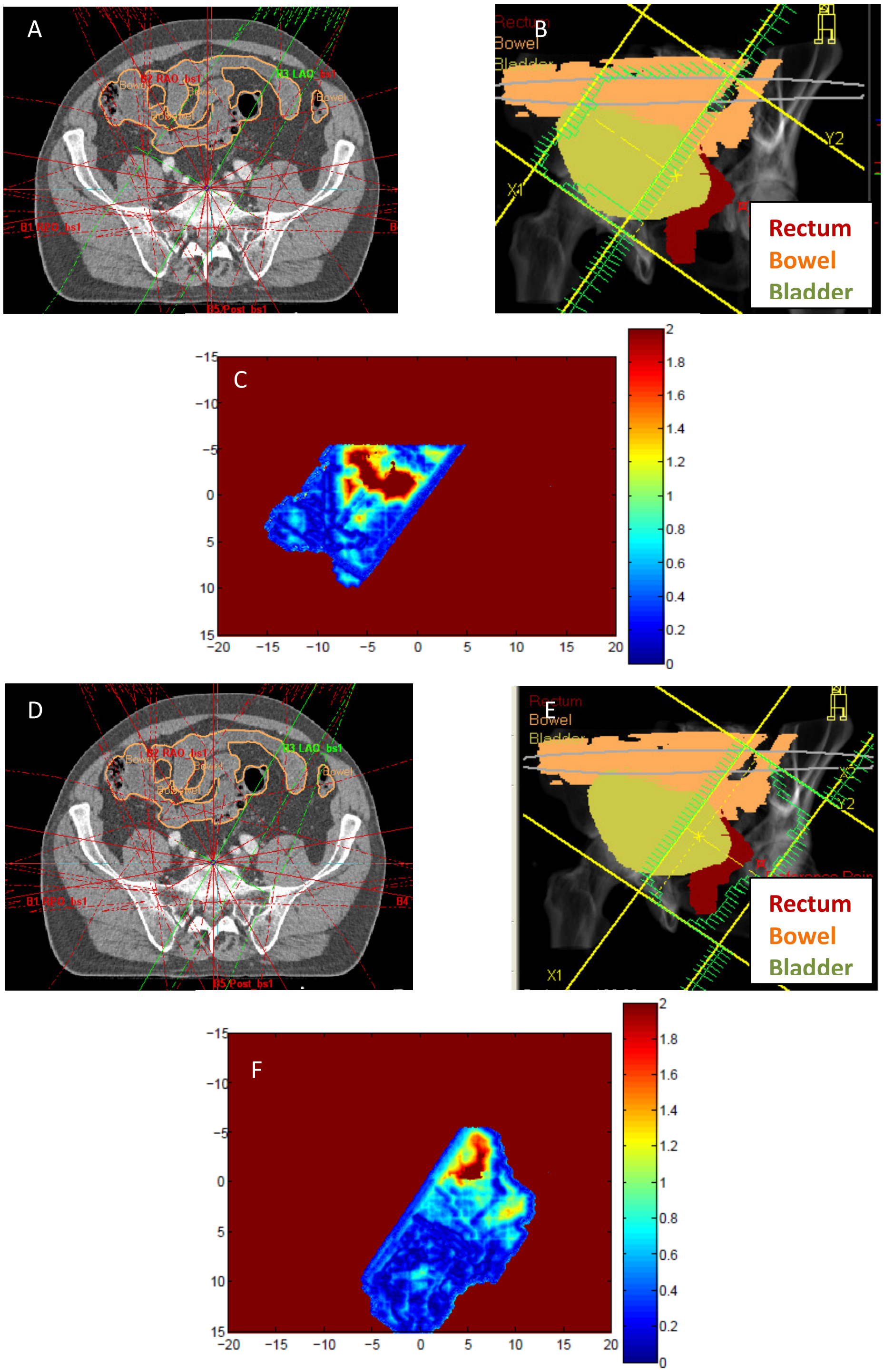

Figure 7.13. Verification results for beams 5 and 6 in table 7.3. A) Location of beam 5 on CT scan (green), B) Beam 5 Beam's Eye View, C) Beam 5 gamma map, D) Location of beam 6 on CT scan (green), E) Beam 6 Beam's Eye View, F) Beam 6 gamma map. NB The area outside the beam has been excluded from all calculations and therefore should not be interpreted according to the colour scale.

Initial evaluation of patient 4 in table 7.1 additionally showed a poor verification result, with an average of only 83% of points (standard deviation 5.7%) passing gamma criteria of 5%, 5 mm. It was known that this patient had positional problems for the first fraction, so a request to repeat images was made. On acquiring images on the subsequent fraction, the average verification pass-rate of 96% shown in table 7.1 was obtained, and the technique verified the patient's shoulder to be in the incorrect position for the first fraction, which would not be picked up by the standard isocentre set-up images of (12 × 12) cm^2. Figure 7.14 below shows the coronal view, beam's eye view and gamma passes for fractions 1 and 2 for beam 3 for this patient plan.

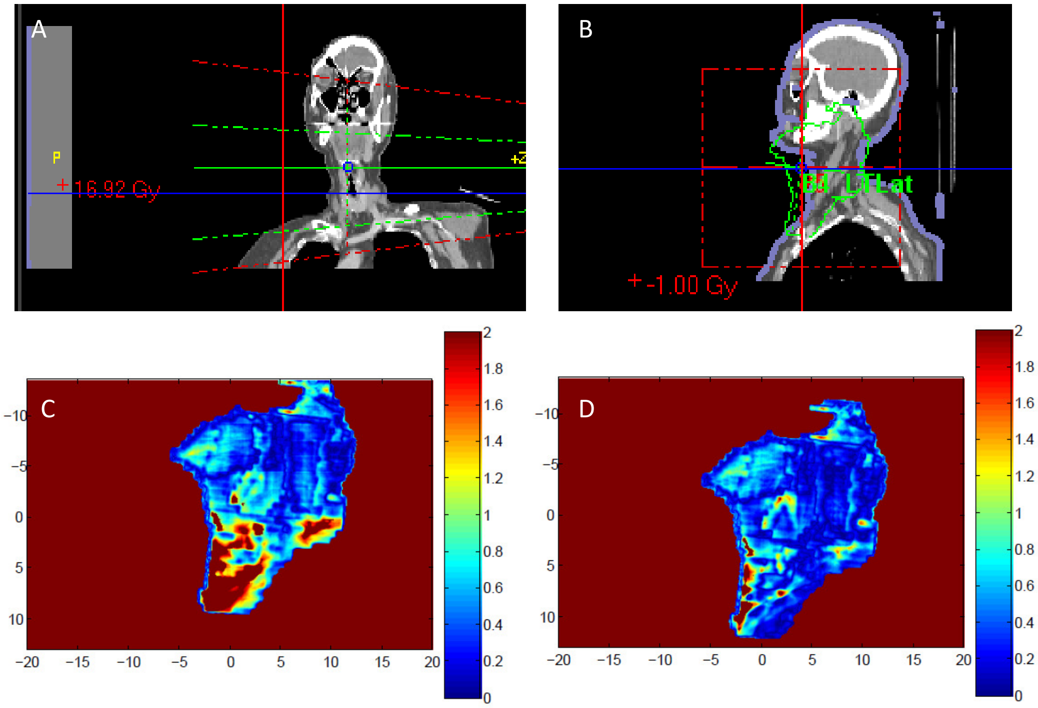

Figure 7.14. Gamma maps for subsequent fractions for a patient with known positional problems. A) Coronal view B) Beam's Eye View (green) C) Gamma map fraction 1 D) Gamma map fraction 2. NB The area outside the beam has been excluded from all calculations and therefore should not be interpreted according to the colour scale.

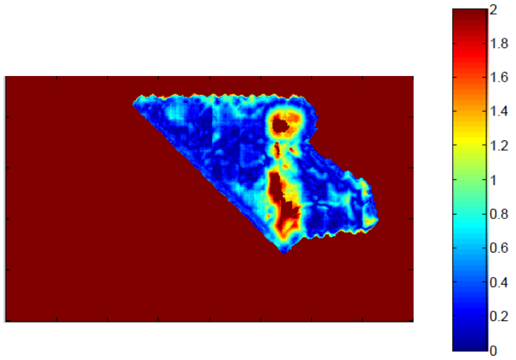

Figure 7.15. Example gamma pass for an anterior beam exiting a couch bar. NB The area outside the beam has been excluded from the calculation and therefore should not be interpreted according to the colour scale.

The technique described here has proved to be a very useful tool in the verification of IMRT delivery during treatment. However, there are still currently some limitations with its use. The main limitation is the size of the imager. The Varian aS500 EPID is only 30 cm × 40 cm and all our IMRT beams are very large (prostate plus nodal IMRT or multiple PTV head and neck IMRT). With the imager positioned at 140 cm SDD, an average of 25% of our IMRT treatment beams do not fit on the panel. The pre-treatment method was not subject to the same limitations as it was possible to rotate the collimator until the beam fitted on the imager. Additionally, anterior or anterior oblique beams may exit the moveable couch bars (the bars are moved out of the beam for posterior or posterior oblique beams so as not to affect the dose delivered to the patient, but this is more difficult for anterior beams). Figure 7.15 gives an example gamma result for an anterior beam exiting a couch bar. However, there is a new couch available from Varian which removes this issue. In addition, due to the lack of treatment time CT scan facilities on our current generation of Varian linacs, any true differences in patient anatomy between planning CT scan and treatment are unknown. This area will however be a productive one for future research and development work.

7.4 Conclusions

The Netherlands Cancer Institute (NKI) verify all their radiotherapy treatments (except for single fraction treatments or fields which are too large to fit on the imager) using their in-house back-projection EPID dosimetry technique. Mans *et al*. (2010) reports that they verified 4337 plans between January 2005 and August 2009, identifying 17 serious incidents, 9 of which would not have been detected by pre-treatment verification. The paper focuses particularly on a rectum plan that was corrupted during data transfer, resulting in an average difference between plan and treatment of 11.6%, local dose differences being as great as 20%. It is believed that the technique described in this thesis would also identify such errors.

OMP is a planning system with continual new developments. It is believed that the package will include a fast MC calculation algorithm for photons within the next 12 months. This development should enable this technique to be adapted to enable the high density materials to be incorporated into the EPID model and so conversion to dose in water and application of the multiple correction factors would not be required. Additionally, modelling of the support arm and cabling would enable a simpler solution for the non-uniform backscatter effect.

Although still in the development phase, the results of INTREPID applied to exit dosimetry are very promising. This technique was presented at EPI2kX, the international Electronic Portal Imaging Conference in Leuven, Belgium (Cufflin *et al.* 2010b) and at the IPEM Biennial Radiotherapy Meeting (Cufflin *et al*. 2010c). The results obtained showed very good agreement with full forward MC calculations for the IMRT cases cited above. This technique, which could easily be transferred to EPIDs from all vendors, enables verification results to be analysed quickly in a clinical setting and has the advantage that it uses the same TPS that was used for initial optimisation and dose calculation of the patient IMRT plan. To date a total of 68 beams from 4 head and neck and 4 pelvic plans have been evaluated, with an average of 96% of points passing gamma criteria of 5%, 5 mm. Additionally, the technique has also proven its ability to pick up dose errors due to changes in patient position or patient anatomy.

Chapter 8

Monte Carlo Patient Dose Verification

8.1 Introduction

One of the aims of this work was to develop a method for full forward MC calculation of portal dose at the imager plane for comparison against acquired EPID images of patients. This involves simulating the radiation transport, beam by beam, throughout the complete patient and EPID geometry within DOSXYZnrc. In the process the MC calculated dose within the patient is obtained 'for free'. With simple rotation and addition of the 3D dose files generated by DOSXYZnrc, the MC calculated dose within the patient can also be compared directly with that calculated by the TPS, providing an additional check of the TPS dose calculation for the patient plan. Uncertainties of 2% at the imager plane result in uncertainties of approximately 0.5% within the patient (per beam), and so a very accurate calculation of dose within the patient may be obtained provided other parameters such as the HU to electron density conversion and cross section data are sufficiently accurate.

It is a requirement that an independent monitor unit calculation is performed for all clinical radiotherapy plans (Royal College of Radiologists 2008). The more complex the treatment technique the more complex these check calculations become, calculation methods becoming particularly complicated for sophisticated planning and delivery techniques such as IMRT. A number of MU check calculation programmes are available, but these are very limited as they are only able to provide confirmation of dose at a point, and account for patient inhomogeneties using the radiological depth method, which is only valid if lateral charged particle equilibrium is maintained. For this reason many centres still verify the delivery of every patient’s IMRT treatment plan on a phantom. However, although this method confirms the correct delivery of the patient plan, phantoms used for routine verification are usually constructed of uniform perspex or water equivalent material, and so this procedure only confirms the ability of the TPS to calculate the dose correctly to a uniform phantom and not necessarily to the heterogeneous patient anatomy.

The method proposed in this chapter for full forward calculation of portal dose enables confirmation of the dose delivery during treatment, combined inherently with an accurate, 3D dose comparison of the TPS plan calculation for the patient.

8.2 Methods

8.2.1 Full Forward Calculation of Portal Dose

The process map for this technique is given in figure 8.1. As a pilot study, full forward MC calculation of portal dose was carried out for a total of 8 patient IMRT plans from a combination of prostate and head and neck treatments, all plans having been originally planned and optimised on OMP. The patient CT dataset and plan parameters were exported in DICOM format from OMP and imported into Matlab software. The plan parameter file includes all information to enable the CT data to be rotated about the patient plan isocentre by the relevant gantry angle so that the full 31 layer EPID model (including the non-uniform slabs of backscattering material to represent the support arm and cabling) can then attached at the relevant position perpendicular to the beam direction (figure 8.2).

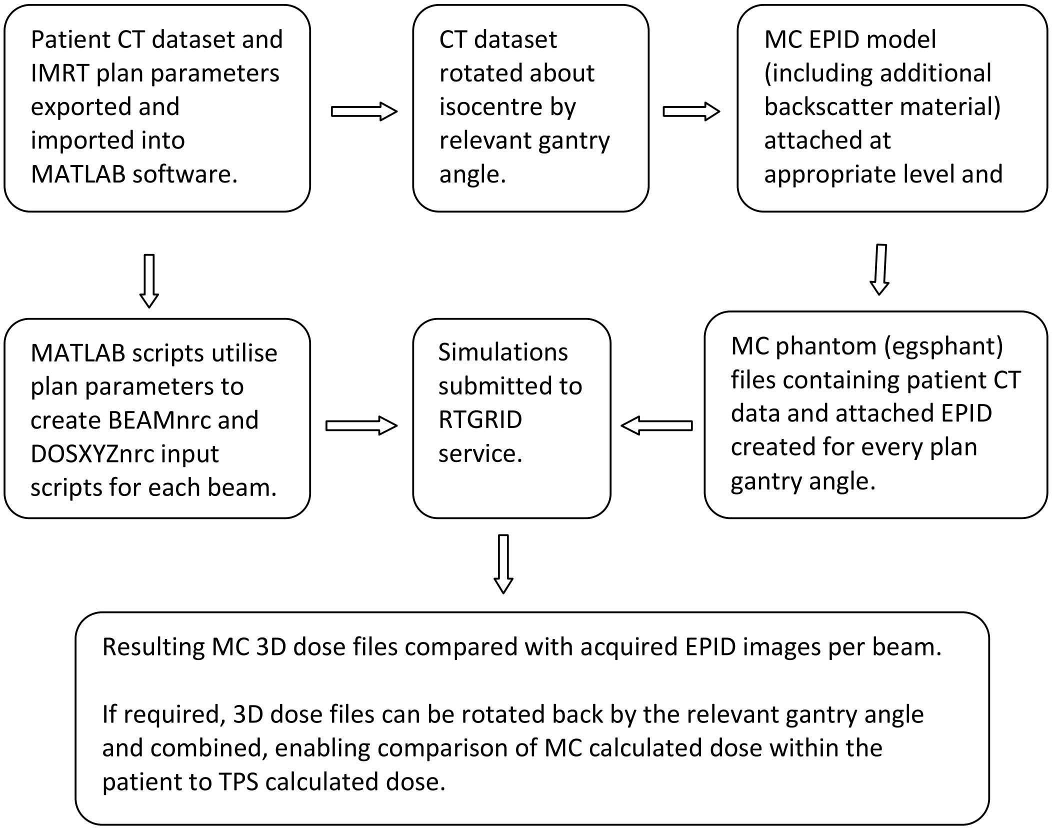

Figure 8.1. Process map for MC Exit dosimetry.

The method for rotating the patient CT dataset followed a similar routine to the ‘TWIZ&GLU’ routine described by Chin *et al.* (2003), Chin (2005). Chin described a 3 step routine to enable variable gantry angle simulations with the SLIC EPID, the routine involving 1) rotating the phantom by –*‘gantry angle’* around the isocentre; 2) “padding” the exterior of the phantom with additional air-filled voxels to obtain a rectangular frame; and 3) adding the EPID beneath the phantom at a specified SDD. The integrated phantom was then ready to serve as input for a DOSXYZnrc run, in which the beam was directed as if the gantry was not rotated. The routine performed as part of this work is very similar, the main differences being the replacement of the SLIC EPID with an aS500 EPID model, and a shift of the patient

CT dataset so that the isocentre corresponds to the centre of the patient geometry in all planes prior to rotation. The isocentre being located at the centre of the geometry simplifies the task of adding the aS500 EPID model with additional backscattering material; the backscattering material is non-uniform and thus location relative to the isocentre is critical. As stated by Chin (2005) this method ensures that the EPID model voxels correspond to the DOSXYZnrc orthogonal planes. Rotation of the continuous EPID contours would lead to inaccurate projection of the different thicknesses of the detector layers (figure 8.3).

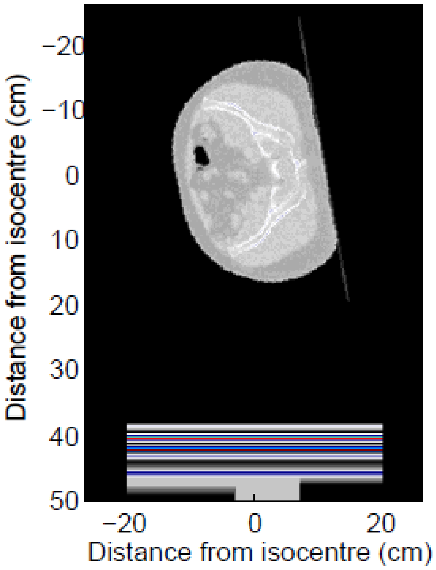

Figure 8.2. Showing a rotated patient CT slice with MC EPID model attached perpendicular to the beam direction for a beam gantry angle of 100°.

The accelerator portion of the simulation was performed with BEAMnrc, radiation transport within the patient and EPID being simulated within DOSXYZnrc. Matlab scripts were written for automated creation of BEAMnrc and DOSXYZnrc input files for each IMRT beam using the plan parameters, this method requiring that each beam be simulated separately. The DOSXYZnrc coordinate system differs from the DICOM coordinate system used conventionally within radiotherapy (and within the TPS), and so conversion to the DOSXYZnrc coordinate system is required. However, as the technique described here involves a rotation of the CT image and all treatment plans investigated in this study consist of co-planar beams (treatment couch angle = 0°), the only variable was the beam collimator angle, which can easily be related to the parameter 'phicol' within DOSXYZnrc.

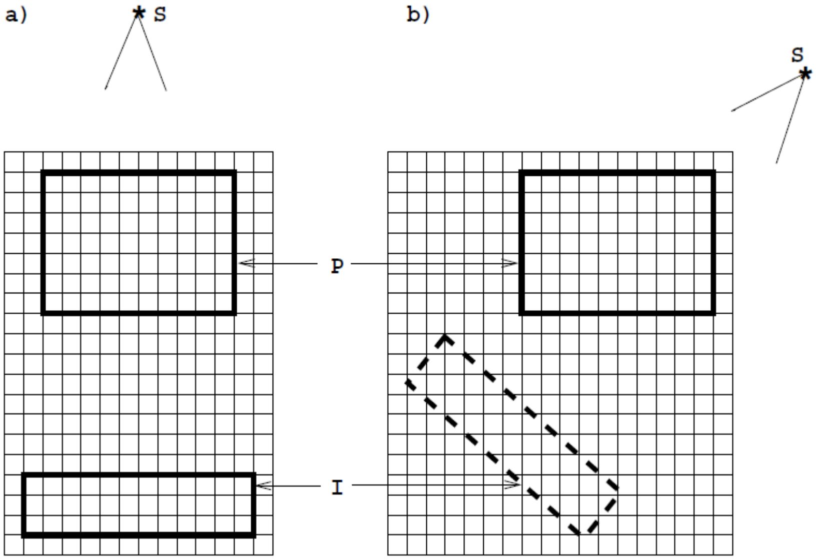

Figure 8.3. Defining a patient / phantom dataset (P) and an imager (I) on a common rectilinear grid. Beam direction from the source (S) is shown: a) irradiation from gantry angle 0°; b) irradiation from oblique angle, where the voxel boundaries no longer correspond to imager surfaces. Reproduced from Chin 2005.

In DOSXYZnrc, by default, each material in a CT phantom is indexed using a single digit ranging from one to nine, limiting the phantom composition to a maximum of 9 materials, which is insufficient for the integrated phantoms developed in this work. Therefore, indexing was changed to use characters greatly extending the number of materials. DOSXYZnrc was similarly modified for compatibility.

The MC simulation requires conversion of the CT HU to electron densities according to the appropriate 'ramp' for the CT scanner used, the accuracy of this CT ramp playing a major part in the final accuracy of the MC simulation results. The CT ramp (figure 8.4) was obtained locally using the CIRS Model 062 phantom (figure 7.4), with multiple inserts of known electron density. Additionally, the DOSXYZnrc MC code requires correct material specification (according to ICRU 1984), for example, soft tissue, bone, lung or air for all voxels.

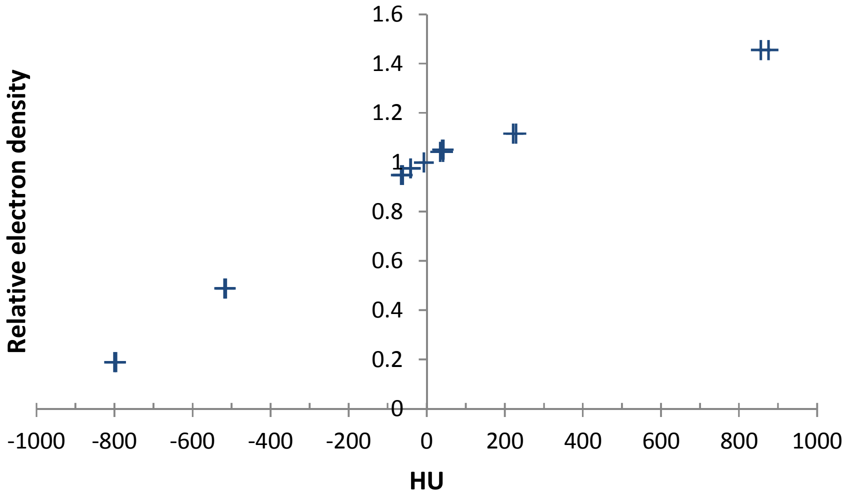

Figure 8.4 VCC scanner HU to electron density curve, the points representing the CIRS phantom inserts.

All simulations were run with a resolution of (2 × 2) mm^2, with 3 mm spacing between CT slices. Fine resolution is required for evaluation of complex IMRT plans with high dose gradients, although these simulations are computationally intensive for such large MC phantom (egsphant) files. Simulations were therefore run on the RTGrid service (chapter 2, Downes *et al.* 2009), which provides access to hundreds of PCs at Cardiff University via a web portal. Results for all beams for a patient plan (up to 14 beams) are obtained within 24 hours. Although the method is time consuming it is possible to run the simulations prior to the patient starting treatment, enabling immediate evaluation of EPID images following the first fraction. To obtain uncertainties of around 2% at the EPID it was found experimentally that the number of histories required was given by equation 8.1.

$$N = \frac{200 \times A}{nsplit \times v_{voxel} \times s^2} \qquad (8.1)$$

where A is the beam area, nsplit is the photon splitting number, v_{voxel} the voxel size and s the required uncertainty. This 'rule of thumb' was developed from equation 2.2. Photon splitting and DBS were set to 100 and 1000 respectively.

As with all MC simulations of Varian linacs it was necessary to correct for backscatter from the jaws to the monitor chamber using the method described by Liu *et al*. (2000). It was found that the position of the MLCs had no effect on the backscatter to the monitor chamber and so a single factor was used per beam (the jaws currently remain at a fixed position for each IMRT beam). Calibration was performed for a single (10 × 10) cm^2 field exiting a 15 cm thickness of water equivalent material, the MC simulation being calibrated directly against an EPID measurement with the same set-up. Some of our EPID panels are ageing and (from time to time) moved between different linacs, so it was deemed necessary to perform a calibration measurement each week on the particular machine on which patient exit images were to be taken. Additionally it was necessary to divide all MC simulations by a MC ‘flood’ image, as per the standard Varian calibration procedure (equation 4.1).

The exit dose images obtained were evaluated using the 2D gamma evaluation method for a 20% dose threshold using ‘pass’ criteria of 5%, 5 mm. Gamma criteria of 5%, 5 mm have been used for all exit dosimetry work in this thesis as changes in patient anatomy between planning CT and treatment make 3%, 3mm an unrealistic goal.

8.2.2 Evaluation of Dose within the Patient

Full forward MC calculation of portal dose involves simulating the radiation transport throughout the complete patient and EPID geometry, and so in the process the MC calculated dose within the patient is also obtained. With simple rotation and addition of the DOSXYZnrc generated 3D dose files, the MC calculated dose within the patient can also be compared directly with the calculated TPS dose, providing an additional check of the TPS dose calculation for the patient plan. Of the 8 cases involved in the MC portal dose study (see above), the MC calculated dose within the patient was compared with TPS calculated dose for two IMRT plans, one head and neck and one prostate. Patients 2 and 5 from table 8.1 were chosen as representative plans for this purpose.

Absolute calibration of the MC dose within the patient was performed using a similar method to absolute dose calibration of a linear accelerator. At our centre, linear accelerators are calibrated so that 100 MU is equal to 100 cGy at d_{max} for a (10 × 10) cm^2 field at 100 cm SSD. All calibration measurements are performed at 5 cm deep, however, and converted to the dose at d_{max}, as there are fewer uncertainties in measurement due to set-up and electron contamination at depth. In a similar way, the MC model of the linear accelerator was calibrated by calculating the MC dose at 5 cm depth in water for a (10 × 10) cm^2 field and a correction factor applied so that 100 MU gave a dose of 100 cGy at d_{max}.

Conventionally treatment planning system algorithms calculate dose to water, whereas MC calculates the energy deposited per unit mass, or dose, to a particular medium. Therefore, in order to evaluate agreement between MC and TPS calculated dose, the MC dose to medium would first need to be converted to dose to water using Bragg Gray Cavity theory by application of stopping power ratios for the medium and for water (Siebers *et al.* 2000). However, all OMP treatment plans evaluated here were calculated using the OMP CC 'enhanced' algorithm, which calculates dose to medium and so no conversion from dose to medium to dose to water was required. Comparison against the OMP pencil beam algorithms would require this correction and so this would need to be considered in any additional investigations comparing the MC calculated dose with pencil beam calculated plans. However, due to the known weaknesses of the pencil beam algorithm in heterogeneous patient anatomy its use is likely to be phased out and was therefore not used as a comparator in this work.

OMP calculated doses were compared against MC generated doses using the 2D gamma evaluation method, slice by slice, for a 20% dose threshold using gamma ‘pass’ criteria of 3%, 3 mm. An overall gamma pass value for the plan was obtained by calculating a weighted mean of the percentage of points passing for all slices (the gamma pass value for the slice was weighted dependent on the area of each slice with greater than the 20% dose threshold).

8.3 Results

8.3.1 Full Forward Calculation of Portal Dose

For the 68 exit dosimetry beams evaluated from the 8 patient plans considered, an average of 96.6% of points within the 20% dose threshold passed gamma criteria of 5%, 5 mm when using the forward MC method. The results are summarised in table 8.1. It should be noted that all beams exiting via couch bars were omitted from these results. The TPS based technique described in the previous chapter gave an average gamma pass of 96.0% when using the same criteria (table 7.1). It can be seen that the MC technique gave a slight, but insignificant (very much less than one standard deviation), improvement in results. This was somewhat surprising as a greater improvement in the verification results was expected using the MC technique, MC being widely accepted as the most accurate patient dose calculation method. However, as discussed in the previous chapter, dose discrepancies greater than 5% are likely to be due to changes in patient anatomy between pre-treatment CT scan and treatment or due to incorrect positioning of the patient during treatment. The availability of a treatment-time CT scan would obviously enable this to be confirmed. It can be seen that there is a particularly low gamma pass rate and high standard deviation for patient 6, this being the same patient identified as having a very full bowel for the pre-treatment scan in Chapter 7 section 3.5. Figure 8.5 shows the acquired image, MC simulation result, gamma map and percentage difference map for beam 6 from patient 6. The 'beam's eye view' in this case is shown in Figure 7.13. It can be seen that there is generally very good agreement between MC simulation and acquired image, the area failing the gamma criteria corresponding to patient bowel, which was full during the pre-treatment scan and so not readily reproducible.

Patient Number	**Region**	**Number of beams**	**Average percentage of points passing gamma 5%, 5 mm**	**Standard deviation, σ**
1	Head and neck	14	97.5	1.7
2		8	98.0	1.4
3		10	97.1	2.5
4		5	94.9	3.1
5	Prostate plus nodes	8	99.1	0.7
6		10	90.5	11.7
7		7	98.0	2.7
8		6	97.5	1.7
Overall Average			**96.6**	**3.2**

Table 8.1. IMRT verification results for MC exit dosimetry technique.

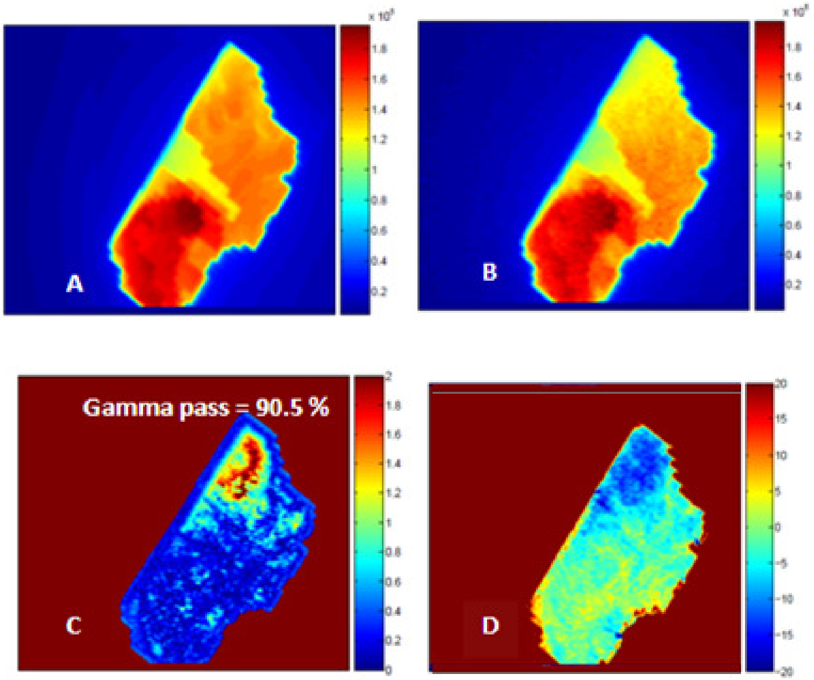

Figure 8.5. Results for beam 6 patient 6. A) Acquired patient EPID image, B) MC simulation, C) Gamma map for 5%, 5 mm, D) Percentage difference between acquired image and MC simulation. It should be noted that for images C and D the area outside the beam is excluded from the calculation and therefore should not be interpreted according to the colour scale.

All results to date have omitted beams exiting through treatment couch bars, which attenuate the beam by 10% (figure 8.6). If these couch bars were static it would be easy to incorporate them within the MC simulation, but unfortunately the bars are moveable to enable posterior beams to avoid them, as beam entry through a couch bar would significantly affect the patient dose. Correction for the effect of the bars is made more difficult by this movement when evaluating anterior and anterior-oblique beams exiting through them. However, the new Varian couches no longer have these highly attenuating bars, and so updating to a new couch system will remove this problem.

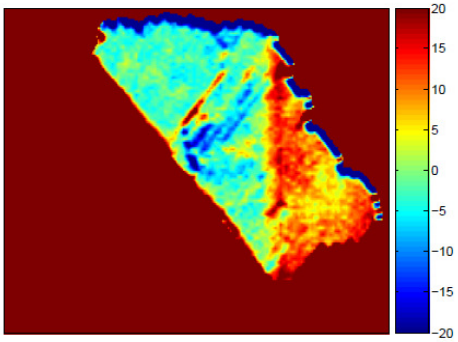

Figure 8.6. Percentage difference between MC simulation and acquired image for a beam exiting a couch bar. It should be noted that the area outside the beam is excluded from the calculation and therefore should not be interpreted according to the colour scale.

8.3.2. MC Evaluation of Dose within the Patient

There was very good agreement between MC simulation and the OMP collapsed cone 'enhanced' calculation of the IMRT patient dose distribution for both the head and neck plan (patient 2) and the prostate plan (patient 5) evaluated. An average of 98.3% of points (plan 2) and 95.7% of points (plan 5) passed gamma criteria of 3%, 3 mm.

Figure 8.7 shows the OMP calculated dose distribution, the MC calculated dose distribution and resulting gamma map for a sample CT slice for the prostate plan evaluated. It can be seen that although there is very good agreement between the two calculation methods, the OMP calculated dose is 2% to 3% lower towards the centre of the patient. A dose difference of 2% in this region would be expected as OMP overestimates the electron density for adipose and fat tissues as discussed in the previous chapter. OMP currently assigns an electron density of 0.95 for HU of -96, whereas it should be about 0.92. For prostate patients with large amounts of adipose tissue this small difference would therefore be expected at the centre of the patient.

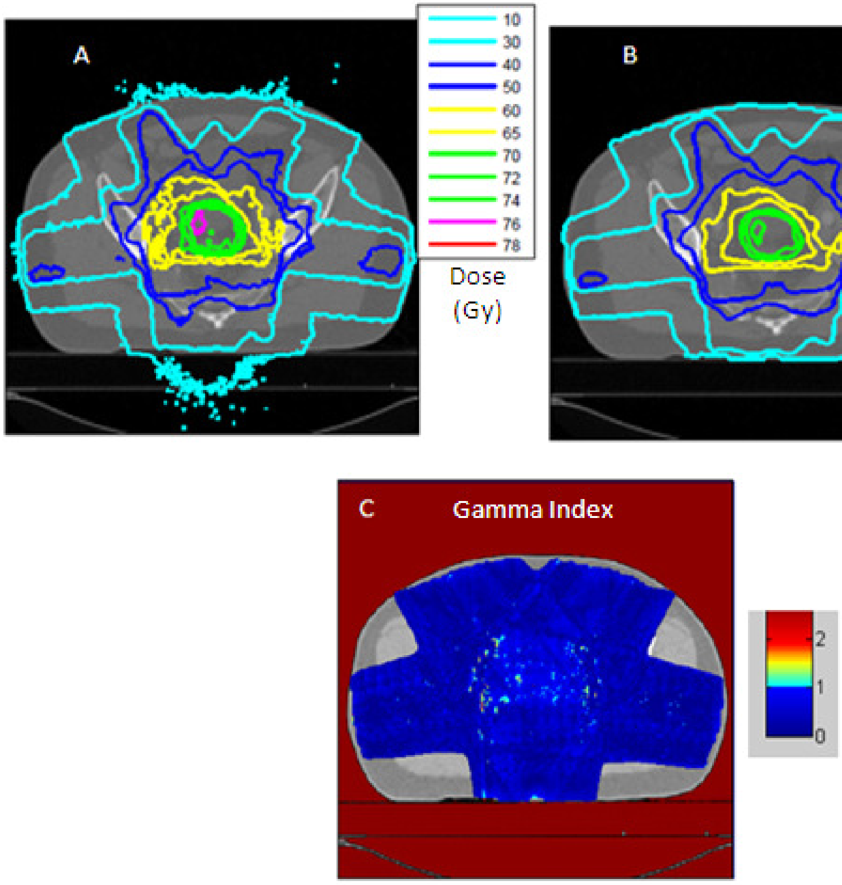

Figure 8.7. A) The MC calculated dose distribution (in Gray) for one CT slice for the prostate IMRT plan , B) OMP calculated dose distribution for the same CT slice and C) gamma map for the slice (for a 20% dose threshold). NB The area outside the patient should not be interpreted according to the colour scale.

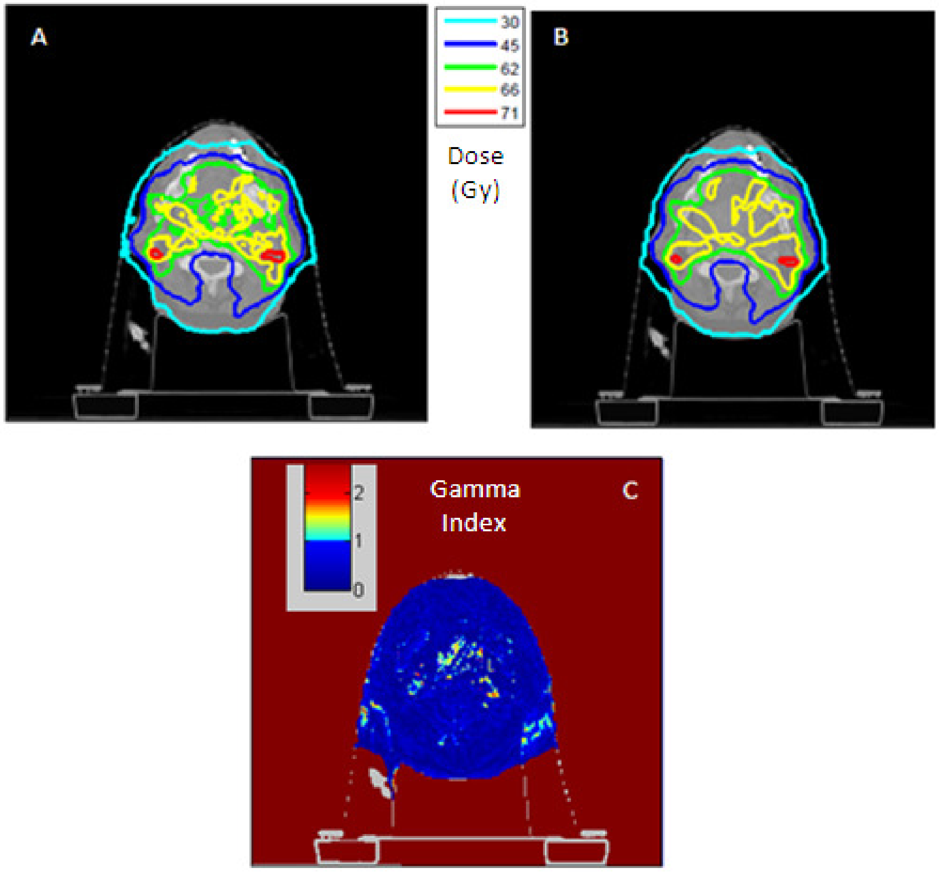

Figure 8.8. A) The MC calculated dose distribution (in Gray) for one CT slice for the head and neck IMRT plan , B) OMP calculated dose distribution for the same CT slice and C) gamma map for the slice. NB The area outside the patient should not be interpreted according to the colour scale.

Figure 8.8 shows the OMP calculated dose distribution, the MC calculated dose distribution and resulting gamma map for a sample CT slice for the head and neck plan evaluated. The overall gamma pass for this plan was 95.7%, and close inspection of results for all slices revealed that the plan consistently failed the gamma criteria in regions where HU is in the range 75 to 175. From figure 8.4 it can be seen that this range of HU falls in the area that corresponds to a change in gradient of the electron density to HU curve, and we currently have no data for this particular region. Removing the voxels with HU in the range 75 to 175 from the evaluation improved the overall gamma pass from 95.7% to 98.1%. Data in this range is therefore of limited accuracy and further investigation needs to be carried out to establish the correct electron density to HU conversion to use for our scanner in this range.

8.4 Conclusions

A full forward MC exit dosimetry technique has been developed. Evaluation of patient exit EPID images acquired during treatment produced very good results with an average of 97% of points passing gamma criteria of 5%, 5 mm. Areas failing these criteria were found to correspond to changes in anatomy between pre-treatment planning CT scan and treatment. This technique obtained marginally better results on average than the INTREPID technique described in the previous chapter, and would be suitable for the verification of the delivery of patient IMRT plans during treatment as a stand-alone method, or as a back-up system to aid in investigations when alternative methods fail the accepted gamma criteria.

The advantage of the full forward MC exit dosimetry technique is that in the process the MC dose within the patient is calculated ‘for free’ with no additional resources required. This MC calculated dose within the patient can be used to confirm the TPS calculated dose distribution before treatment. This is particularly useful for complex IMRT plans that stretch the ability of MU check calculation programmes, and where confirmation of dose at a single point is meaningless. For this reason many centres still verify all their IMRT patient plans on a phantom before treatment, however many of these phantoms are homogeneous and so this does not confirm the TPS dose calculation within the heterogeneous patient media. The MC exit dosimetry technique described as a part of this chapter would enable full 3D verification of the TPS calculated dose distribution whilst additionally verifying the delivery of the plan at treatment-time.

The results in this chapter were presented in part at the Second European Workshop on Monte Carlo Treatment Planning (Cufflin *et al.* 2009b).

Chapter 9

Conclusions

9.1 Summary

This work has focused on the development of EPID dosimetry techniques applicable to the verification of IMRT, the following aspects in particular.

1. A MC modelling solution devised to correct for non-uniform backscatter to the imager from supporting structures has been developed (Chapter 4, Cufflin *et al.* 2010a). The solution involved adding different thicknesses of water equivalent material to the back of the MC EPID model until MC simulated 'flood' images best matched the raw flood images. Although relatively simple, this method has proved efficient at correcting for the effects of non-uniform differential backscatter for all field sizes both on and off-axis. This solution has enabled the MC verification of large, clinical IMRT fields covering almost the entire detector area (Chapter 5). Incorporating this correction for non-

uniform backscatter greatly improved gamma pass-rates for the IMRT fields evaluated, the number of points passing gamma criteria of 2%, 2 mm improving from 78.6% to 95.7% for the complex head and neck case investigated.

2. The work in Chapter 5 proved MC portal dosimetry to be a particularly sensitive dose verification tool, accurate enough to detect real sub-MU delivery errors (Cufflin *et al.* 2008).
3. This work has developed a method for predicting acquired EPID images by calculating the dose in water at the EPID level within the TPS and applying a series of correction factors, based on MC simulation and measurement, to convert to EPID image intensity. INtegrated TReatment Planning and EPID Dosimetry (INTREPID) has been applied both pre-treatment (Chapter 6, Cufflin *et al.* 2009a) and to verify delivery during treatment (Chapter 7, Cufflin *et al.* 2010b, 2010c) achieving very satisfactory verification results. When applied pre-treatment, INTREPID is a very time efficient process, requiring 10 minutes per patient on the linac and taking only a few minutes to calculate on the TPS. When applied for verification during treatment, INTREPID calculation times are similarly time efficient. To date a total of 68 beams from 4 head and neck and 4 pelvic plans have been evaluated, with an average of 96% of points passing gamma criteria of 5%, 5 mm. Additionally, the technique has also proven its ability to pick

up dose delivery errors due to changes in patient position or patient anatomy.

4. A novel, field-size and position dependent matrix-based correction for the non-uniform backscattering materials to the rear of the imager has been developed (Chapter 6). This solution can be applied to all EPID dosimetry techniques, regardless of calculation method. When incorporated into INTREPID the devised correction for non-uniform backscatter improved agreement between predicted and measured EPID intensities. Average pre-treatment gamma pass results for 3%, 3 mm are improved from 96% ($\sigma = 3.3$) to 98% ($\sigma = 1.6$), with a significant improvement of results for any fields with small segments off-axis in the target direction.

5. A full-forward MC exit portal dosimetry technique has been developed for the a-Si EPID (Chapter 8), incorporating the modelling of the backscattering components as described in Chapter 4. Use of the RTGrid service and optimisation of MC simulation parameters enables results of clinical IMRT plans to be obtained overnight. Evaluation of patient exit EPID images acquired during treatment produced very good results with an average of 97% of points passing gamma criteria of 5%, 5 mm. Areas failing these criteria were found to correspond to changes in anatomy between pre-treatment planning CT scan and treatment. The advantage of the full forward MC exit dosimetry technique is that in the

process the MC dose within the patient is also calculated with no additional resources required. This MC calculated dose within the patient can be used to confirm the TPS calculated dose distribution before treatment.

9.2 Further Work and Discussion

One of the weaknesses of this work is the current unavailability of treatment-time CT images on our Varian linacs to confirm any changes in patient position or anatomy between planning CT and treatment. When this data becomes available the techniques described in this work can be adapted to calculate the treatment time dose projection. The MC technique will additionally provide information on how any differences in patient anatomy influence the dose delivered to the patient.

INTREPID, the TPS based EPID dose prediction method presented as a part of this work, modelled a 'water equivalent EPID' within the planning system requiring factors to convert from dose in water to dose in EPID and to correct for field size output factors in different materials. On the other hand, the BEAMnrc MC methods developed have simulated dose to the EPID directly, and so such correction factors are not required. It is anticipated, however, that Nucletron will introduce a MC photon dose calculation option within OMP in the near future. When the MC option is available it may enable accurate calculation of dose to high density materials such as those in the EPID. This would therefore allow for the accurate modelling of EPID plus backscattering supporting materials within OMP, removing the need for correction factors and simplifying the INTREPID method.

Many centres are now moving towards delivering IMAT (Intensity Modulated Arc Therapy), a form of IMRT that delivers radiation as single or multiple continuous arcs as opposed to delivery at discrete 'gantry' angles. IMAT is attractive as it is able to provide highly conformal dose distributions comparative to those of IMRT, but with increased delivery speed. A technique offering increased delivery speeds is appealing as this enables greater patient throughput and therefore reduction of patient waiting times. A number of treatment planning systems calculate IMAT plans by splitting the arc into discrete beams every 4° or so around the patient, increasing the number of discrete beams increasing the dose calculation accuracy. This IMAT dose calculation method could be applied directly to the EPID dose prediction techniques described in this thesis, enabling direct adaptation of the techniques to IMAT deliveries.

All work in this thesis has compared acquired EPID images with predicted images at the EPID level, enabling quick analysis of delivery at the treatment unit and simple analysis of the origin of any errors. However, many published approaches back-project the EPID images to enable delivered dose calculation within the patient, for comparison against the planned TPS dose distribution (van Elmpt *et al.* 2007, van Elmpt *et al.* 2008b, Wendling *et al.* 2006). Most centres performing routine back-projection of EPID images have Elekta or Siemens linacs, and the author is unaware of any back-projection methods that include a correction for the Varian non-uniform backscatter issue. Dosimetry Check, a commercial solution that claims to be available for all linac manufacturers, does not include such a correction. This thesis has shown these backscatter effects to be significant for the large IMRT fields, for head and neck or prostate plus nodal treatments, delivered at our centre. As already stated, the novel matrix-based correction method developed as a part of this work is versatile and could be adapted to be included in all EPID dose calculation methods.

References

1. Ahnesjo A, Andreo P, and Brahme A (1987), 'Calculation and application of point spread functions for treatment planning with high energy photon beams', Acta. Oncol. 26: 49-56
2. Ahnesjö A (1989), 'Collapsed cone convolution of radiant energy for photon dose calculation in heterogeneous media', Med. Phys. 16:577-92
3. Ahnesjö A and Trepp A (1991), 'Acquisition of the effective lateral energy fluence distribution for photon beam dose calculations by convolution methods', Phys. Med. Biol. 36:973-985
4. Ahnesjö A, Saxner M and Trepp A (1992), 'A pencil beam model for photon dose calculation', Med. Phys. 19:263-273
5. Ahnesjö A and Aspradakis M (1999), 'Dose calculations for external photon beams in radiotherapy', Phys. Med. Biol. 44:R99-R155
6. Ahnesjö A, Weber L, Murman A, Saxner M, Thorslund I, and Traneus E (2005), 'Beam modelling and verification of a photon beam multisource model', Med. Phys. 32:1722-37
7. Aspradakis MM, Morrison RH, Richmond ND and Steele A (2003), 'Experimental verification of convolution/superposition photon dose calculations for radiotherapy treatment planning', Phys. Med. Biol. 48:2873-2893
8. BEAM manual: OMEGA-BEAM Workshop (1997), National Research Council Canada
9. Bentley RE, Jones JC and Lillicrap SC (1967), 'X-ray spectra from accelerators in the range 2 to 6 MeV', Phys. Med. Biol. 12:301–14
10. Berger MJ (1963), 'Monte Carlo Calculation of the Penetration and Diffusion of Fast Charged Particles', Methods in Computational Physics, 1:135-215
11. Berry SL, Polvorosa CS andWuu CS (2010), 'A field size specific backscatter correction algorithm for accurate EPID dosimetry', Med. Phys. 37:2425-34
12. Bielajew AF and Rogers DWO (1987), 'PRESTA: The Parameter Reduced Electron-Step Transport Algorithm for electron Monte Carlo transport' Nucl. Instr. Meth. B18:165-181
13. Brewster D, Fraser L, Harris V, and Black R (2000), 'Rising incidence of prostate cancer in Scotland: increased risk or increased detection?', BJU International 85:463-73
14. Budgell GJ, Mott JH, Williams PC and Brown KJ (2000), 'Requirements for leaf position accuracy for dynamic multileaf collimation', Phys. Med. Biol. 45:1211-27
15. Budgell GJ, Zhang R and Mackay RI (2007), 'Daily monitoring of linear accelerator beam parameters using an amorphous silicon EPID', Phys. Med. Biol. 52:1721–1733
16. Cancer Research UK (2011), 'CancerStats Incidence UK', https://publications.cancerresearchuk.org/WebRoot/crukstoredb/CRUK_PDFs/CSINCIDENCE2010.pdf

17. Castadot P, Lee JA, Geets X and Grégoire V (2010), 'Adaptive radiotherapy of head and neck cancer', Semin. Radiat. Oncol. 20:84-93
18. Chen J, Chuang CF, Morin O, Aubin M and Pouliot J (2006), 'Calibration of an amorphous silicon flat panel imager for exit beam dosimetry', Med. Phys. 33: 584 – 94
19. Chetty IJ, Curran B, Cygler JE, DeMarco JJ, Ezzell G, Faddegon BA, Kawrakow I, Keall PJ, Liu H, Ma CM, Rogers DW, Seuntjens J, Sheikh-Bagheri D and Siebers JV (2007), 'Report of the AAPM Task Group No. 105: Issues associated with clinical implementation of Monte Carlo-based photon and electron external beam treatment planning.' Med. Phys. 34:4818-53
20. Chin PW, Spezi E and Lewis DG (2003), 'Monte Carlo simulation of portal dosimetry on a rectilinear voxel geometry: a variable gantry angle solution', Phys. Med. Biol. 48: N231 – N238
21. Chin P W, Lewis D 20. G and Spezi E (2004), 'Correction for dose-response variations in a scanning liquid ion chamber EPID as a function of linac gantry angle Phys. Med. Biol. 49 (8): N93-N103
22. Chin PW (2005), PhD thesis on 'Monte Carlo Portal Dosimetry', University of Wales College of Medicine
23. Chin P W, Lewis D G and Giddy J P (2005), 'A Monte Carlo solution for external beam photon radiotherapy verification', The Monte Carlo Method: Versatility Unbounded in a Dynamic Computing World (Oak Ridge: American Nuclear Society, ISBN 0-9448-695-0)
24. Cufflin RS, Spezi E, Millin AE and Lewis DG (2008), 'Monte Carlo Based Investigation of Dose Rate Dependency in IMRT Portal Dosimetry', presentation at EPI2k8 (Electronic Portal Imaging 2008), San Francisco.
25. Cufflin RS, Spezi and Lewis DG (2009a), 'IMRT Verification using Portal Dosimetry and a 3D Planning System', poster presentation at UKRO 2009, Clinical Oncology 21:264 - 265
26. Cufflin RS, Spezi E, Millin AE and Lewis DG (2009b), 'MC portal dosimetry as a reference standard in exit dose IMRT verification', presentation at the Second European Workshop on Monte Carlo Treatment Planning (MCTP), Cardiff 2009
27. Cufflin RS, Spezi E, Millin AE and Lewis DG (2010a), 'An investigation of the accuracy of Monte Carlo portal dosimetry for verification of IMRT with extended fields', Phys. Med. Biol. 55:4589-600
28. Cufflin RS, Spezi E, Millin AE and Lewis DG (2010b), 'Treatment planning system based exit dosimetry', presentation at EPI2kX (Electronic Portal Imaging 2010), Leuven
29. Cufflin RS, Spezi E, Millin AE and Lewis DG (2010c), 'Treatment Planning System based portal dosimetry', presentation at IPEM Biennial Meeting, Cardiff
30. Dahlgren CV, Ahnesjo A, Montelius A and Rikner G (2002), 'Portal dose image verification: formalism and application of the collapsed cone superposition method', Phys. Med. Biol. 47:4371 – 4387

31. Dahlgren CV, Eilertsen K, Jorgensen TD and Ahnesjo A (2006), ‘Portal dose image verification: the collapsed cone superposition method applied with different electronic portal imaging devices’, Phys. Med. Biol. 51:335 – 349
32. Dirix P and Nuyts (2010), ‘Value of Intensity Modulated Radiotherapy in Stage IV Head-and-neck Squamous Cell Carcinoma’, Int J Radiat. Oncol. Biol. Phys. 78:1373-80
33. Dirix P, Vanstraelen B, Jorissen M, Poorten VV and Nuyts S (2010), ‘Intensity-Modulated Radiotherapy for Sinonasal Cancer: Improved Outcome Compared To Conventional Radiotherapy’, Int J Radiat. Oncol. Biol. Phys. 78: 998-1004
34. Downes P, Yaikhom G, Giddy JP, Walker DW, Spezi E and Lewis DG (2009), ‘High-performance computing for Monte Carlo radiotherapy calculations’, Philos. Transact. A Math. Phys. Eng. Sci. 28;367(1897):2607-17
35. Ezzell G A and Chungbin S (2001), ‘The overshoot phenomenon in step-and-shoot IMRT delivery’, J. App. Clin. Med. Phys. 2(3): 138 - 148
36. Ezzell GA, Burmeister JW, Dogan N, LoSasso TJ, Mechalakos JG, Mihailidis D, Molineu A, Palta JR, Ramsey CR, Salter BJ, Shi J, Xia P, Yue NJ and Xiao Y (2009), ‘IMRT commissioning: Multiple institution planning and dosimetry comparisons, a report from AAPM Task Group 119’, Med. Phys. 36: 5359:5373
37. Foster I (2005), ‘Globus Toolkit Version 4: Software for Service-Oriented Systems’, In Proc. IFIP Intl. Conf. on Network and Parallel Computing, volume 2872 of LNCS, 2–13
38. Gardner J, Siebers J and Kawrakow I (2007), ‘Dose calculation validation of Vmc++ for photon beams’ Med. Phys. 34:1809-18
39. Grattan MWD and McGarry CK (2010), ‘Mechanical characterization of the Varian Exact-arm and R-arm support systems for eight aS500 electronic portal imaging devices’, Med. Phys. 37:1707-13
40. Greer PB, Cadman P, Lee C and Bzdusek K (2009), ‘An energy fluence-convolution model for amorphous silicon EPID dose prediction’, Med. Phys. 36 :547-55
41. Grigorov GN, Chow JCL and Barnett RB (2006), ‘Dosimetry limitations and a dose correction methodology for step-and-shoot IMRT’, Phys. Med. Biol. 51:637 – 652
42. Hasenbalg F, Fix MK, Born EJ, Mini R and Kawrakow I (2008),‘VMC++ versus BEAMnrc: a comparison of simulated linear accelerator heads for photon beams’, Med. Phys. 35:1521-31
43. Heath E and Seuntjens J (2003), ‘Development and validation of a BEAMnrc component module for accurate Monte Carlo modelling of the Varian dynamic Millennium multileaf collimator’, Phys. Med. Biol. 48:4045-63
44. Huang VW, Seuntjens J, Devic S and Verhaegen F (2005), ‘Experimental determination of electron source parameters for accurate Monte Carlo calculation of large field electron therapy’, Phys. Med. Biol. 50:779 – 786

45. Huedo E, Montero RS, and Llorente IM (2005), 'The GridWay Framework for Adaptive Scheduling and Execution on Grids', Scal. Comput. Pract. Exper. 6:1–8
46. Ibbott GS, Followill DS, Molineu A, Lowenstein JR, Alvarez PE and Roll JE (2008), 'Challenges in Credentialling Institutions and Participants in Advanced Technology Multi-Institutional Clinical Trials', Int J Rad. Oncol. Biol. Phys. 71: S71–S75
47. ICRU Report 37 (1984), 'Stopping Powers of Electrons and Positrons'
48. IMRT Collaborative Working Group (2001), 'Intensity Modulated Radiotherapy: Current Status and Issues of Interest' Int. J. Radiation Oncol. Biol. Phys. 51:880-914
49. Iori M, Cagni E, Paiusco M, Munro P, and Nahum AE (2010), 'Dosimetric verification of IMAT delivery with a conventional EPID system and a commercial portal dose image prediction tool', Med. Phys. 37:377–390
50. Jensen SB, Pedersen AM, Vissink A, Andersen E, Brown CG, Davies AN, Dutilh J, Fulton JS, Jankovic L, Lopes NN, Mello AL, Muniz LV, Murdoch-Kinch CA, Nair RG, Nogueira-Rodrigues A, Saunders D, Stirling B, von Bültzingslöwen I, Weikel DS, Elting LS, Spijkervet FK and Brennan MT (2010), 'A systematic review of salivary gland hypofunction and xerostomia induced by cancer therapies: management strategies and economic impact', Support Care Cancer 18:1061-79
51. Kawrakow I, Fippel M and Friedrich K (1996), '3D electron dose calculation using a Voxel based Monte Carlo algorithm (VMC)', Med. Phys. 23:445-57.
52. Kawrakow I (2000), 'Accurate condensed history Monte Carlo simulation of electron transport. Egsnrc, the new egs4 version', Med. Phys. 27:485 – 98
53. Kawrakow I, Rogers DWO and Walters BRB (2004), 'Large efficiency improvements in BEAMnrc using directional bremsstrahlung splitting', Med. Phys. 31: 2883-98
54. Kawrakow I and Walters BRB (2006), 'Efficient photon beam dose calculations using DOSXYZnrc with BEAMnrc', Med. Phys. 33:3046-3056
55. Kim JO, Siebers JV, Keall PJ, Arnfield MR, and Mohan R (2001), 'A Monte Carlostudy of radiation transport through multi-leaf collimators', Med. Phys. 28**:**2497-2507
56. Kim S (2009), 'Characteristics of elliptical sources in BEAMnrc Monte Carlo system: Implementation and application', Med. Phys.36:1046–1052
57. Knöös T, Wieslander E, Cozzi L, Brink C, Fogliata A, Albers D, Nyström H and Lassen S (2006), 'Comparison of dose calculation algorithms for treatment planning in external photon beam therapy for clinical situations', Phys. Med. Biol., 51:5785–5807
58. Ko L, Kim JO and Siebers JV (2004), 'Investigation of the optimal backscatter for an a-Si electronic portal imaging device', Phys. Med. Biol.

49: 1723 –1738

59. Künzler T, Fotina I, Stock M and Georg D (2009), 'Experimental verification of a commercial Monte Carlo-based dose calculation module for high-energy photon beams', Phys. Med. Biol. 54:7363-77

60. Kuperman VY and Lam WC (2006), ‘Improving delivery of segments with small MU in step-and-shoot IMRT’, Med. Phys. 33:1067 – 1073
61. Li W, Moore J and Siebers J (2006), ‘Using fluence separation to account for energy spectra dependence in computing dosimetric a-Si EPID images for IMRT fields’, Med. Phys. 33: 4468 – 80
62. Litzkow M, Livny M, and Mutka M (1988), ‘Condor - a hunter of idle workstations’, Proceedings of the 8th International Conference of Distributed Computing Systems.
63. Liu HH, Mackie TR and McCullough EC (2000), ‘Modelling photon output caused by backscattered radiation into the monitor chamber from collimator jaws using a Monte Carlo technique’, Med. Phys. 27: 737-44
64. Louwe RJ, McDermott LN, Sonke JJ, Tielenburg R, Wendling M, van Herk MB, and Mijnheer BJ (2004), ‘The long-term stability of amorphous silicon flat panel imaging devices for dosimetry purposes’, Med. Phys. 31:2989–2995
65. Love PA, Spezi E, Lewis DG, Smith CW, Morton E and Munro D (2000), ‘Parallel processing of radiotherapy Monte Carlo simulations on a remote Beowulf cluster’, Proc XIII Int. Conf on the Use of Computers in Radiation Therapy (Heidelberg) edited by W Schlegel T Bortfeld (Berlin: Springer) 409 - 410
66. Low DA, Harms WB, Mutic S and Purdy JA (1998), ‘A technique for the quantitative evaluation of dose distributions’, Med. Phys. 25: 656-61
67. Mackie TR, Scrimger JW and Battista JJ (1985), ‘A Convolution Method of Calculating Dose for 15 MV X- Rays’, Med. Phys. 12:188-196
68. Mackie TR, Liu HH and McCullough (1998), ‘Model-based photon dose calculation algorithms’, Treatment planning in radiation oncology, edited by FM Khan and RA Potish (Lippincot: Williams and Wilkins) 89-112
69. Mainegra-Hing E, Rogers DW and Kawrakow I (2005), ‘Calculation of photon energy deposition kernels and electron dose point kernels in water’, Med. Phys. 32:685-99.
70. Mans A, Wendling M, McDermott LN, Sonke JJ, Tielenburg R, Vijibrief R, Mijnheer B, van Herk M and Stroom JC (2010), ‘Catching errors with in vivo EPID dosimetry’, Med. Phys. 37: 2638 -2643
71. Mayles WPM, Lake R, McKenzie A, Macaulay EM, Morgan HM, Jordan TJ and Powley SK (1999), IPEM Report 81, ‘Physics Aspects of Quality Control in Radiotherapy’
72. McCurdy B M, Luchka K and Pistorius S (2001), ‘Dosimetric investigation and portal dose image prediction using an amorphous silicon electronic portal imaging device’, Med. Phys. 28: 911 – 24
73. McDermott LN, Nijsten SMJJG, Sonke JJ, Partridge M, van Herk M and Mijnheer BJ (2006a), ‘Comparison of ghosting effects for 3 commercial a-Si EPIDs’, Med. Phys. 33: 2448 – 2451
74. McDermott LN, Wendling M, van Asselen B, Stroom J, Sonke JJ, van Herk M and Mijnheer BJ (2006b), ‘Clinical experience with EPID dosimetry for prostate IMRT pre-treatment dose verification’, Med. Phys. 33:3921–30

75. McDermott LN, Wendling M, Nijkamp J, Mans A, Sonke JJ, Mijnheer BJ and van Herk M (2008), '3D in vivo dose verification of entire hypo-fractionated IMRT treatments using an EPID and cone-beam CT', Radiother. Oncol. 86:35–42
76. McDonald MW, Godette KD, Whitaker DJ, Davis LW, and Johnstone PA (2009), 'Three-Year Outcomes of Breast Intensity-Modulated Radiation Therapy with Simultaneous Integrated Boost.' Int J Radiat. Oncol. Biol. Phys. 77:523-530
77. McNutt TR, Mackie TR, Reckwert P, Papenikolaou N and Paliwal BR (1996), 'Calculation of portal dose using the convolution / superposition method', Med. Phys. 23:527-535
78. Mohammadi M, Bezak E and Reich P (2006), 'Comparison of two-dimensional transmitted dose maps: evaluation of existing algorithms', Australas. Phys. Eng. Sci. Med. 29:179 -87
79. Mohan R, Chui C and Lidofsky L (1986), 'Differential pencil beam dose computation for photons', Med. Phys. 63:64-73
80. Mohan R, Tong S, Arnfield M, Wu Q, and Siebers J (2000), 'The impact of fluctuations in intensity patterns on the number of monitor units and the quality and accuracy of intensity modulated radiotherapy', Med. Phys. 27:1226–1237
81. Moore JA and Siebers JV (2005), 'Verification of the Optimal Backscatter for an a-Si electronic portal imaging device', Phys. Med. Biol. 50:2341 – 2350
82. Nelson WR, Hirayama H and Rogers DWO (1985), 'The EGS4 Code System', Report SLAC-265. SLAC, Stanford
83. Nicolini G, Fogliata A, Vanetti E, Clivio A and Cozzi L (2006), 'GLAaS: An absolute dose calibration algorithm for an amorphous silicon portal imager. Applications to IMRT verifications', Med. Phys. 33: 2839 - 51
84. Nijsten SMJJG, van Elmpt WJC, Jacobs M, Mijnheer BJ, Dekker ALAJ, Lambin P and Minken AWH (2007a), 'A global calibration model for a-Si EPIDs used for transit dosimetry', Med. Phys. 34: 3872-84
85. Nijsten SM, Mijnheer BJ, Dekker AL, Lambin P and Minken AW (2007b), 'Routine individualised patient dosimetry using electronic portal imaging devices', Radiother Oncol. 83:65–75
86. Oncentra® MasterPlan v3.3 Physics and Algorithms Manual
87. Parent L, Seco J, Evans PM, Fielding A and Dance DR (2006), 'Monte Carlo modelling of a-Si EPID response: the effect of spectral variations with field size and position', Med. Phys. 33:4527-40
88. Parent L, Fielding AL, Dance DR, Seco J and Evans PM (2007), 'Amorphous silicon EPID calibration for dosimetric applications: comparison of a method based on Monte Carlo prediction of response with existing techniques', Phys. Med. Biol. 52: 3351 – 3368
89. Partridge M, Ebert M and Hesse BM (2002), 'IMRT verification by three dimensional dose reconstruction from portal beam measurement', Med. Phys. 29:1847–58

90. Piermattei A, Fidanzio A, Azario L, et al. (2007), 'Application of a practical method for the isocenter point in vivo dosimetry by a transit signal', Phys. Med. Biol. 52:5101–17
91. Ramsey CR, Salter BJ, Shi J, Xia P, Yue N J and Xiao Y (2009), 'IMRT commissioning: Multiple institution planning and dosimetry comparisons, a report from AAPM Task Group 119', Med. Phys. 36 : 5359:5373
92. Reich P, Bezak E, Mohammadi M and Fog L (2006), 'The prediction of transmitted dose distributions using a 3D treatment planning system', Australas Phys. Eng. Sci. Med. 29(1): 18-29
93. Renner WD, Norton K and Holmes T (2005), 'A method for deconvolution of integrated electronic portal images to obtain incident fluence for dose reconstruction', J Appl. Clin. Med. Phys. 6:22–39
94. Rogers DWO, Faddegon BA, Ding GX, Ma CM, We J and Mackie TR (1995), 'BEAM: a Monte Carlo code to simulate radiotherapy treatment units', Med. Phys. 22: 503-24
95. Rogers DWO, Ma M, Walters B, Ding GX, Sheikh – Bagheri D and Zhang G (2001), BEAMnrc Users Manual, NRCC Report PIRS – 0509A (rev G). NRCC, Ottawa
96. Rogers DW (2006). 'Fifty years of Monte Carlo simulations for medical physics.' Phys. Med. Biol. 51:R287-301
97. Royal College of Radiologists (2008), 'Towards Safer Radiotherapy', BFCO(08)1
98. Sankar AP, Nichol LEA and Macleod A (2010), 'Initial experience on the evaluation of 'DosimetryCheck' – First commercial EPID based transit dosimetry solution', poster presentation at IPEM Biennial Radiotherapy Meeting July 2010
99. Sheikh-Bagheri D and Rogers DWO (2002), 'Sensitivity of megavoltage photon beam Monte Carlo simulations to electron beam parameters', Med. Phys. 379 – 390
100. Siebers JV, Keall PJ, Nahum AE, and Mohan R (2000), 'Converting absorbed dose to medium to dose to water for Monte Carlo based photon beam dose calculations', Phys. Med. Biol. 45:983–98
101. Siebers JV, Kim JO, Ko L, Keall PJ and Mohan R (2004), 'Monte Carlo computation of dosimetric amorphous silicon electronic portal images', Med. Phys. 31 : 2135 – 2146
102. Spezi E and Lewis DG (2002), 'Full forward Monte Carlo calculation of portal dose from MLC collimated treatment beams', Phys. Med. Biol. 47:377-390
103. Spezi E, Lewis DG and Smith CW (2002), 'A DICOM-RT based toolbox for the evaluation and verification of radiotherapy plans', Phys. Med. Biol. 47:4223-4232
104. Spezi E (2003), PhD thesis on 'Monte Carlo simulation of Intensity Modulated Radiotherapy'

105. Spezi E, Angelini AL and Ferri A (2006), 'A multiple acquisition sequence for IMRT verification with a 2D ion chamber array', Med. Dosim. 31:269-72
106. Staffurth J (2010), 'A Review of the Clinical Evidence for Intensity-modulated Radiotherapy', Clin. Oncol. 22:643-657
107. Steciw S, Warkentin B, Rathee S and Fallone BG (2005), 'Three dimensional IMRT verification with a flat panel EPID' Med. Phys. 32(2): 600 - 612
108. Thomas SJ (1999), ' Relative electron density calibration of CT scanners for radiotherapy treatment planning', BJR 72: 781 – 786
109. van Elmpt WJC, Nijsten SMJJG, Dekker ALAJ, Mijnheer BJ and Lambin P (2007), 'Treatment verification in the presence of inhomogeneities using EPID based three-dimensional dose reconstruction', Med. Phys. 34:2816 – 2826
110. Van Elmpt W, McDermott L, Nijsten S, Wendling M, Lambin P and Mijnheer BJ (2008a), 'A literature review of electronic portal imaging for radiotherapy', Radiother. Oncol. 88:289–309
111. van Elmpt W, Nijsten S, Mijnheer B, Dekker A, Lambin P (2008b), 'The next step in patient-specific QA: 3D dose verification of conformal and intensity-modulated RT based on EPID dosimetry and Monte Carlo dose calculations', Radiother. Oncol. 86:86–92
112. van Elmpt W and Ezzell GA (2009), 'POINT/COUNTERPOINT: EPID dosimetry must soon become an essential component of IMRT quality assurance', Med. Phys. 36, 4325:4328
113. Van Esch A (2004), 'The use of an a-Si based EPID for routine absolute dosimetric pre-treatment verification of dynamic IMRT fields', Radiotherapy and Oncology. 71: 223 -234
114. van Herk M and Meertens H (1988), 'A matrix ionisation chamber imaging device for on-line patient setup verification during radiotherapy', Radiother Oncol. 11(4):369-78
115. Verhaegen F and Seuntjens J (2003), 'Monte Carlo modelling of external radiotherapy photon beams'. Phys. Med. Biol. 48: R107– R164
116. Walters BRB, Kawrakow I and Rogers DWO (1996), DOSXYZ Users Manual NRCC Report PIRS-794revB
117. Walters B and Kawrakow I (2007), 'Technical note: Overprediction of dose with default PRESTA-I boundary crossing in DOSXYZnrc and BEAMnrc', Med. Phys. 34:647 - 650
118. Wang S, Gardner JK, Gordon JJ, Li W, Clews L, Greer PB, and Siebers JV (2009), 'Monte Carlo-based adaptive EPID dose kernel accounting for different field size responses of imagers', Med. Phys. 36:3582-3595
119. Warkentin B, Steciw S, Rathee S and Fallone BG (2003), 'Dosimetric IMRT verification with a flat panel EPID', Med. Phys. 30: 3143 – 55
120. Welsh JS, Mackie TR and Limmer JP (2007), 'High-energy Photons in IMRT: Uncertainties and Risks for Questionable Gain', Technology in Cancer Research and Treatment. 6:147-149

121. Welsh Cancer Intelligence and Surveillance Unit (2010), 'Cancer Survival Trends in Wales, 1985-2004', http://www.wales.nhs.uk/sites3/home.cfm?orgid=242
122. Wendling M, Louwe RJW, McDermott LN, Sonke JJ, van Herk M, Mijnheer BJ (2006), 'Accurate two- dimensional IMRT verification using a back-projection EPID dosimetry method', Med. Phys. 33(2): 259 – 336
123. Williams MV (2007), 'Improving patient safety in radiotherapy by learning from near misses, incidents and errors', British Journal of Radiology 80:297-301

Appendix 1: Publications and Presentations

Journal Publications

'An investigation of the accuracy of Monte Carlo portal dosimetry for verification of IMRT with extended fields', R S Cufflin, E Spezi, A E Millin and D G Lewis, Phys. Med. Biol. **55**(16):4589-600 (2010)

Invited Presentations

'Treatment planning system based EPID dosimetry', R S Cufflin, E Spezi, A E Millin and D G Lewis, Oncentra Masterplan User Group Meeting, Cardiff 2010

Proffered Conference Oral Presentations

'Treatment planning system based exit dosimetry', R S Cufflin, E Spezi, A E Millin and D G Lewis, European Society for Therapeutic Radiation and Oncology (ESTRO) Biennial Meeting, London 2011

'Treatment planning system based portal dosimetry', R S Cufflin, E Spezi, A E Millin and D G Lewis, Institute of Physics and Engineering in Medicine (IPEM) Biennial Meeting, Cardiff 2010

'Treatment planning system based exit dosimetry', R S Cufflin, E Spezi, A E Millin and D G Lewis, Electronic Portal Imaging Workshop (EPI2kX), Leuven, 2010

'MC portal dosimetry as a reference standard in exit dose IMRT verification', R S Cufflin, E Spezi, A E Millin and D G Lewis, Second European Workshop on Monte Carlo Treatment Planning (MCTP), Cardiff 2009

'Monte Carlo portal dosimetry as the gold standard for IMRT verification', R S Cufflin, E Spezi, A E Millin and D G Lewis, MCNEG Monte Carlo User Group Meeting, Oxford 2009

'Monte Carlo based investigation of dose rate dependency in IMRT portal dosimetry', R S Cufflin, E Spezi, A E Millin and D G Lewis, Electronic Portal Imaging Workshop (EPI2k8), San Francisco 2008

'Differences in IMRT delivery with dose-rate detected using Monte Carlo portal dosimetry', R S Cufflin, E Spezi, A E Millin and D G Lewis, Institute of Physics and Engineering in Medicine (IPEM) Biennial Meeting, Bath 2008

‘Monte Carlo EPID modelling: An IMRT verification solution’, R S Cufflin, A E Millin and D G Lewis, Institute of Physics and Engineering in Medicine (IPEM) Annual Scientific Meeting, Cardiff 2007

‘Optimisation of image acquisition parameters for IMRT verification (using Monte Carlo Portal Dosimetry)’, R S Cufflin, A E Millin and D G Lewis, Portal Imaging: Back to Basics, British Institute of Radiology BIR 2007

Proffered Conference Poster Presentations

‘Development of a Monte Carlo based technique to improve accuracy of portal dosimetry’, European Society for Therapeutic Radiation and Oncology (ESTRO) Biennial Meeting, Maastricht 2009

‘IMRT Verification using portal dosimetry and a 3D planning system’, UK Radiation Oncology Conference (UKRO) Cardiff 2009, Clinical Oncology 21:264 - 265

Appendix 2: Glossary of Abbreviations

This glossary gives a list of abbreviations used in this thesis.

BCA	**Boundary Crossing Algorithm.** The algorithm used to transport particles across boundaries in Monte Carlo simulations.
CC	**Collapsed Cone.** A dose calculation algorithm used in radiotherapy treatment planning systems (see section 2.2.2).
CPU	**Central Processing Unit.** The central processing unit of a computer.
DBS	**Directional Bremsstrahlung Splitting.** A variance reduction technique used in BEAMnrc Monte Carlo simulations (see section 2.1).
d_{max}	**Depth of Maximum Dose.** Depth of maximum dose on the central axis of a radiotherapy beam.
DRR	**Digitally Reconstructed Radiograph.** A radiograph reconstructed from CT data.
DTA	**Distance to Agreement.**
ED	**Electron Density.** The number of electrons per unit volume. In radiotherapy the ED of a material relative to that of water is usually quoted.
ECUT	**Electron Transport Cut Off.** If an electron energy falls below the transport cut off, the particle trajectory is terminated and its energy deposited in the current region.
EGS	**Electron Gamma Shower.** The EGS computer code system is a general purpose package for the Monte Carlo simulation of electron and photon transport.
EPID	**Electronic Portal Imaging Device.** EPIDs capture radiotherapy beam transmission images and are primarily used to verify the patient position during treatment, but they also have the potential to be used as efficient dose verification tools of high spatial resolution.

EWWF	**Equivalent Window Width Field.** A first-order approximation of the equivalent square field size for MLC shaped apertures (see section 6.2).
FSF	**Field Size Output Factor.** Ratio of output at d_{max} for a reference field (usually 10 cm × 10 cm) to output at d_{max} for a given field size. It should be noted that this definition used in this thesis, and at VCC is the inverse of the factor used at many other centres.
HTC	**High Throughput Computing.** The use of many computing resources to accomplish a computational task**.**
HU	**Hounsfield Units.** Hounsfield Units, or CT numbers, represent the difference in X-ray attenuation between a given material and water.
ICRU	**International Commission on Radiation Units.** Organisation whose principal objective is the development of internationally acceptable recommendations regarding quantities and units of radiation.
IGRT	**Image Guided Radiotherapy.** IGRT utilises images, such as EPID or cone beam CT images, to improve accuracy and precision of treatments.
IMAT	**Intensity Modulated Arc Therapy.** Radiotherapy treatment achieving high conformity to the tumour volume by dynamic movement of the linac gantry and MLCs during treatment.
IMRT	**Intensity Modulated Radiotherapy.** Radiotherapy treatment achieving high conformity to the tumour volume by modulating the beam profile using moving MLCs during treatment (section 1.3).
INTREPID	**INtegrated TReatment Planning and EPID Dosimetry.** Technique developed as a part of this work to calculate the dose at the EPID utilising the treatment planning system and a series of derived correction factors (see chapters 6 and 7).
IPEM	**Institute of Physics and Engineering in Medicine.** UK Registered charity that promotes the advancement in physics for medical benefits**.**
KERMA	**Kinetic Energy Released per unit Mass.** KERMA is the energy released in a medium, per unit mass, by indirectly ionising radiation.

Linac	**Linear Accelerator.** A type of particle accelerator in which charged particles are accelerated by means of oscillating electric fields. They are used for the production of X-rays and electrons for therapeutic purposes (radiotherapy).
MC	**Monte Carlo.** Monte Carlo methods simulate physical processes utilising probability distributions and random number generators (statistical sampling).
MLC	**Multileaf Collimator.** Beam shaping device made of many high density narrow ‘leaves’ (see section 1.3).
MU	**Monitor Units.** Calibrated radiotherapy machine unit.
NGS	**National Grid Service.** A HTC service that provides computing power for all that require it by simply ‘plugging in’.
NKI	**Netherlands Cancer Institute.** Key research and cancer institute based in Amsterdam.
NTCP	**Normal Tissue Complication Probability.** Prediction model of the biological effect of radiation to healthy tissues.
OAR	**Organs at Risk.** Healthy critical organs in close proximity to the radiotherapy treatment area.
OMP	**Oncentra MasterPlan.** Treatment planning system from Nucletron (The Netherlands) for the preparation of radiotherapy treatment plans and calculation of patient dose.
PB	**Pencil Beam.** A dose calculation algorithm used in radiotherapy treatment planning systems (see section 2.2.2).
PCUT	**Photon Transport Cut Off.** If the photon energy falls below the transport cut off, its trajectory is terminated and the energy deposited in the current region.
PTV	**Planning Target Volume.** The tumour plus margins allowing for uncertainties and variations in tumour location and patient positioning.
QC	**Quality Control.** A process that is used to ensure a certain level of quality in a product or service, for example, the routine examination and testing of the quality of products.

SDD	**Source to Detector Distance.** Distance between the accelerator source and the measuring detector.
SLIC	**Scanning Liquid Ion Chamber.** Older version of an EPID utilising a liquid ionisation chamber.
TCP	**Tumour Control Probability.** Prediction model of the biological effect of radiation in controlling tumour growth.
TERMA	**Total Energy Released in the Medium.** Quantity used in CC calculation algorithms (see section 2.2.2).
TPS	**Treatment Planning System.** Computer system used for the preparation of radiotherapy treatment plans and calculation of patient dose.
VCC	**Velindre Cancer Centre.** VCC in Cardiff, Wales, is one of the largest cancer centres in the UK, providing specialist cancer services to over 1.5 million people in South East Wales and beyond.